Centrifuge Modeling to Investigate the Runout Behavior of Impounded Fly Ash

By

SAMUEL BAYLOR FOLLETT

THESIS

Submitted in partial satisfaction of the requirements for the degree of

MASTER OF SCIENCE

in

Civil & Environmental Engineering

in the

OFFICE OF GRADUATE STUDIES

of the

UNIVERSITY OF CALIFORNIA

DAVIS

Approved:

Alejandro Martinez, Chair

Daniel W. Wilson

Ross W. Boulanger

Committee in Charge

2021

Centrifuge Modeling to Investigate the Runout Behavior of Impounded Fly Ash

ABSTRACT

The failure of impounded fly ash at the Kingston Fossil Plant in 2008 led to severe economic and environmental consequences from the flow of ash for almost one kilometer downstream. With over 700 active surface impoundments and federal disposal regulations enacted in 2015, the coal-power industry is required to properly address the risk and possible consequences associated with impounded fly ash. The Electric Power Research Institute and the University of California Davis, Center for Geotechnical Modeling collaborated to advance the understanding of possible flow failures of impounded ash, including conditions that lead to its triggering, methods to identify its potential in the field, and the potential impacts of dewatering.

A centrifuge testing program began in 2018 to explore the influence of initial density and dewatering of impounded ash, with a focus on its runout behavior after a model impoundment is subjected to a loss of lateral confinement. This study presents the results from the one centrifuge test performed at 60 g and three 1 g tests conducted in 2021, with comparisons made to four previous 60 g tests. Fly ash was deposited into a novel centrifuge container, with a pair of gates opened in flight to induce an idealized containment structure failure. The strength and stiffness of the ash were measured prior to the failure using a miniature CPT penetrometer and bender elements for the 60 g test and a miniature T-bar penetrometer for the 1 g tests. Pore pressures were measured throughout the entire 60 g test using tensiometers, and water contents were measured using moisture probes for all tests during specimen preparation and testing. Various cameras were used to track the runout after the opening of the gates. Failure mechanisms of the ash ranged from slope instability to a drastic flow failure in the 60 g tests, and flow failures to a slumping-like failure in

the 1 g tests Although the runout results between the 60 g and the 1 g tests agree in the effect of ash density, the failure mechanisms were not found to be comparable due to differences in confining stress between the two test types. Ash strength and stiffness and water table height were found to impact the runout length in all tests. The results from this testing program and comparison to the previous centrifuge tests demonstrate that dewatering can improve the stability of fly ash impoundments and that looser deposits are more prone to flow failures associated with large runout distances.

ACKNOWLEDGMENTS

I would like to thank Professor Alejandro Martinez for the opportunity to participate in the fly ash research, for teaching me new perspectives in geotechnical engineering, and for supporting me through my ambitious goals for graduate school. I'd like to thank Professor Srikanth Madabhushi, who has guided me through complicated research and provided timely support, despite being across the globe due to COVID-19. I would also like to thank Alexander Orlando for helping me complete my research during the sweltering heat of a Davis summer. Thank you to Mandeep Singh Basson for your help with all things coding and always providing constructive feedback for my research. Thank you to Professor Trevor Carey for teaching me the ropes of centrifuge modeling and always making sure I had my head on straight. Thank you to the CGM staff for helping me through a difficult project. And thank you to Kyle O'Hara for making sure I wasn't taking life too seriously.

I would like to thank Dan Wilson for guiding me through the intricacies of centrifuge modeling and for reviewing my work. Thank you to Professor Ross Boulanger, who inspired me to pursue geotechnical engineering as a career many years ago and for supporting me throughout graduate school. Thank you to Professor Jason DeJong for your guidance and sharing your insightful perspectives. And thank you to Professor Katerina Ziotopoulou for providing exceptional mentorship and support, and for working with me to make sure I got the best graduate education possible.

I'd like to thank my fellow graduate students; graduate school would not have been the same without you. Thank you to my friends and family. Thank you to my mother and father for supporting me through my entire life and through my shenanigans. And thank you to Michelle and

Nova, who have provided so much love and support and have made sure I went to bed at a reasonable time these past two years.

This material is based upon work supported by the Electric Power Research Institute. Any opinions, findings, and conclusions or recommendations expressed in this material are those of the author and do not necessarily reflect the views of the Electric Power Research Institute.

Financial support for this research was also provided through the COVID-Impacted Research Funding Program by the University of California Davis.

Table of Contents

LIST OF TABLES

LIST OF FIGURES

1 INTRODUCTION

On December 22nd, 2008, a dike failure occurred at a fly ash dredge cell at the Kingston Fossil Plant (under the Tennessee Valley Authority, TVA) in Tennessee, shown in **Figure 1**. About 4.1 million cubic meters of ash were released in flow slides over one to two hours after the initial failure (TVA 2009). Ash spilled almost a kilometer downstream, damaged or destroyed 26 homes, and infiltrated the Emory River, as shown in **Figure 2**. The failed cell was used for permanent disposal, with the ash hydraulically excavated from an adjacent ash pond and allowed to settle in the cell (Bachus and Santamarina 2014). The failure caused significant environmental damage and required extensive cleanup efforts, with TVA estimating the cost of spill ranging from $675 million to $975 million, not including litigation and claims.

Fly ash makes up more than 58% of coal combustion products, which is generated in a combustion chamber in the flue gas and is captured with air pollution control equipment (Kalyoncu 2001). When not recycled, fly ash is typically stored in impoundments by placing it as a slurry composed of ash particles and wastewater. With more than 700 active surface impoundments in the United States and corresponding disposal regulations enacted in 2015 (EPA 2015), the need to be able to characterize the runout behavior of impounded fly ash has become apparent. Past failures of fly ash impoundments and mine tailings dams have resulted in catastrophic consequences from the liquefaction of the impounded material and its subsequent flow downstream (Santamarina et al. 2019).

Previous studies have been performed by the Electric Power Research Institute (EPRI) to investigate the behavior of ponded fly ash. EPRI in 2012 studied basic engineering properties of ponded ash from 22 different sources, with an emphasis on assessing its static liquefaction potential. Diagenesis (cementation through geochemical reactions) potential was also determined

based on measured pH of the ash material. In 2013 and 2015, geotechnical centrifuge tests were performed by EPRI on sand embankments constructed over saturated fly ash deposits, with the goal of investigating the process of undrained failures caused by rapid surcharge loading. In 2014, EPRI investigated discrepancies in traditional CPT correlations for fly ash and proposed recommendations to alter them, as well as a plate load test to assess the shear strength mobilization in the ash. In 2020, EPRI evaluated diagenesis potential for five types of ash, with an emphasis on its effect on shear strength and consolidation behavior.

Figure 1. Failed fly ash impoundment at Kingston Fossil Plant, TN (Photo: Greenpeace).

In collaboration with EPRI, research was undertaken at the University of California Davis (UC Davis) to investigate the parameters that influence the runout behavior of fly ash when subjected to a sudden loss of lateral confinement. The sudden loss of lateral confinement acts an idealized failure of a containment structure, such as a dredge cell failure. From this failure, pore pressures within the ash can change from the following mechanisms: a reduction in mean total

stress (from the loss of stress perpendicular to the failed portion of the containment structure), plastic volumetric strains (or shear-induced dilatancy), and seepage of water through the ash. A rapid (undrained) change in mean total stress will result in corresponding excess pore pressures. For shear-induced dilatancy, undrained loading in dilative material would be expected to generate negative excess pore pressures from the dilative tendency of the ash, while a contractive material would be expected to generate positive excess pore pressures from the associated contractive tendency.

Figure 2. Fly ash material that flowed downstream of the failed impoundment (Photo: National Geographic).

Expected stress paths of the fly ash under a "sudden loss of lateral confinement" failure are shown at an element level in **Figure 3** (EPRI 2021). Drained loading would be expected to cause failure of the ash by lateral extension, whereas the undrained loading path will depend on the dilatancy (from shear-induced excess pore pressures) of the material. The undrained stress paths are initially vertical while the material is in an elastic state of stress, due to a change in pore

pressure developed that is equal to the change in mean total stress. The stress paths then diverge depending on the materials volume-change behavior under shear. Contractive material may undergo an extensive loss of mean effective stress during failure, as shown by the blue stress path in **Figure 3** tending towards the origin, with a near to total loss of confining stress resulting in static liquefaction. Though the "sudden loss of lateral confinement" failure is an idealization and does not account for any possible interactions with a failed containment structure or downstream topography, actual failures in practice should have a less rapid progression, allowing this research to provide a bound for the behavior of fly ash impounded by failing containment structures.

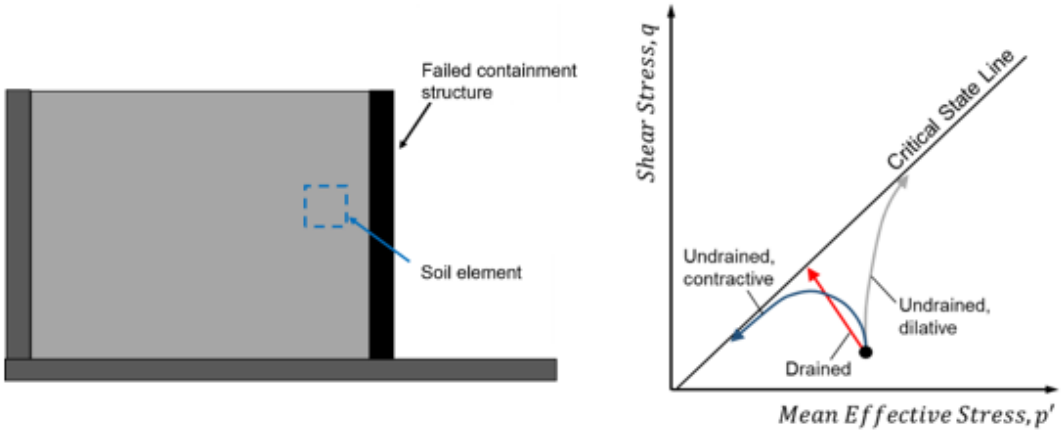

Figure 3. Expected stress paths from a "sudden loss of lateral confinement" failure at an element level (EPRI 2021).

Building upon the work in EPRI (2021), one centrifuge test was performed to assess the effects of dewatering on the strength, stiffness, dilatancy, and runout behavior of a looser ash impoundment (compared to centrifuge models in EPRI 2021). Different CPT strength measurements were correlated with the observed behavior of the ash, with relations to critical state soil mechanics where possible. Pore pressure measurements were used to infer dilatancy of the ash

under the “sudden loss of lateral confinement” failure and were used to support CPT strength estimates and state relations. The results were then related to those found in EPRI (2021). Three 1 g tests were performed to further relate initial density of impounded ash to its runout behavior. Despite inconclusiveness in density measurements, slurry water content and T-bar penetration resistance were able to be correlated with the runout behavior in the 1 g tests. In both the centrifuge test and the 1 g tests, issues identified in EPRI (2021) with the correlated water content readings of the moisture probes were explored further.

2 EXPERIMENTAL METHODS

2.1 Introduction to Testing Program

A centrifuge testing program was conducted at the UC Davis Center for Geotechnical Modeling (CGM) to investigate the runout behavior and consequences of fly ash impoundment failures. Two 1-meter (m) centrifuge, six 9-m centrifuge, and three 1 g tests were performed in total at the CGM. The current study performed for this research thesis includes the final 9-m centrifuge (FR06) and all three of the 1 g tests (T1, T2, and T3), while the previous study (EPRI 2021) included the two 1-m centrifuge and the first five 9-m centrifuge tests (FR01 through FR05). The 1-m centrifuge results are not discussed in this thesis. The EPRI (2021) report referenced throughout this thesis is preliminary, and the final report will include the results from the one 9-m centrifuge test (FR06) performed for this thesis. All 9-m centrifuge tests performed in EPRI (2021) and all tests for this thesis were performed on fly ash from the same source, except for test FR04. For this reason, FR04 is not discussed in this thesis.

2.2 Fly Ash Material

The fly ash tested in this thesis was taken directly from a power plant in the United States and shipped to the CGM in plastic 55-gallon drums. The ash was delivered in a powdered state, with its water content typically between 10 to 20%. Engineering and index properties of the ash are presented, as investigated by EPRI (2012, 2013, 2014, 2015, and 2021). Scanning electron microscope (SEM) photos of the tested ash (EPRI 2014) are presented in **Figure 4**, showing that many of the particles are spherical as a result of the coal burning process.

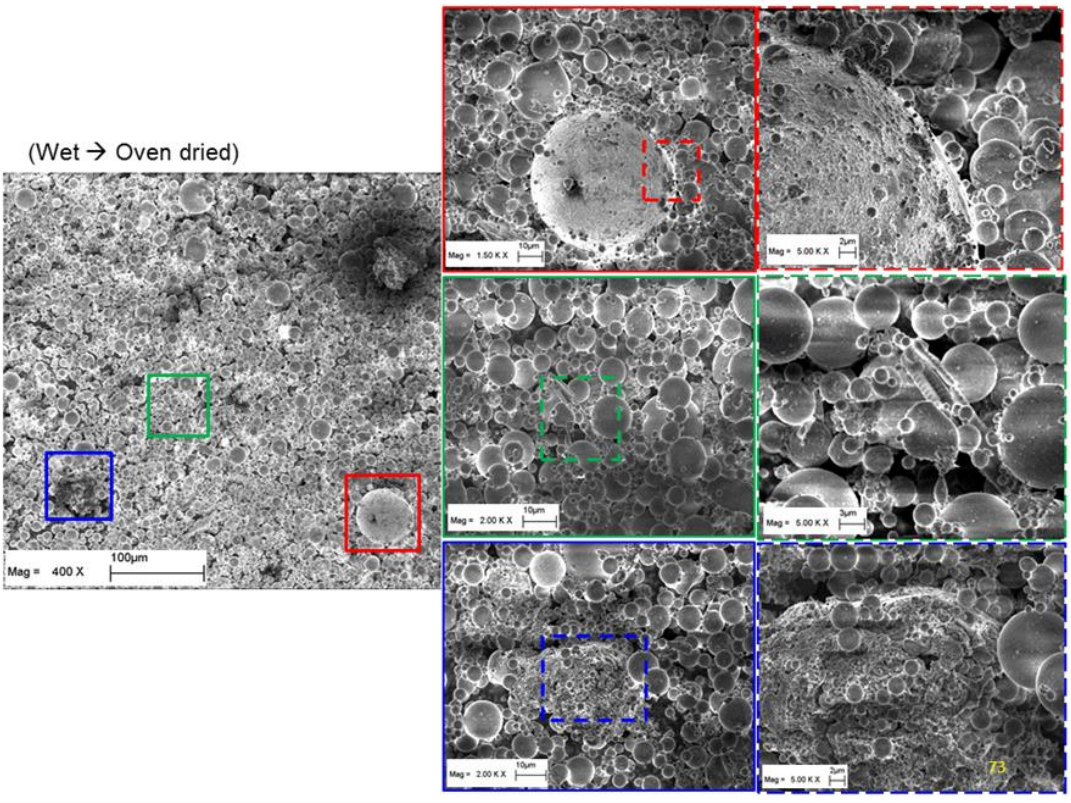

Figure 4. SEM photos of tested fly ash (EPRI 2014).

2.2.1 Index Properties

The ash discussed is designated as Class-F and has a low calcium content. **Table 1** presents the index properties determined by the previous studies. EPRI (2012 & 2015) found the pH of the ash to be a maximum of 8.79, which is below the likely diagenesis threshold of 9.5 described in EPRI (2012). EPRI (2014) reported this specific ash not developing diagenesis during testing, nor was it observed in EPRI (2021) or during handling of the ash. Specific gravity of the ash has been measured between 2.28 to 2.56, with 2.51 from EPRI (2015) being used for all void ratio calculations in this thesis. **Figure 5** shows grain size distribution curves for the ash. The fines content is approximately 90% with about 7 to 10% smaller than 2 microns, and a coefficient of uniformity, C_u, of about 8.5. The liquid limit of the ash ranges from 21 to 28 and was typically

observed to behave in a liquid-like manner in this study around 25% water content during handling. The plastic limit has been measured as 22, resulting in a plasticity index value, *PI*, ranging from 0 to 7.

Table 1. Index properties of the fly ash studied.

Property	EPRI (2015)	EPRI (2012)	EPRI (2013)	EPRI (2021, at UC Davis)	EPRI (2021)
Specific Gravity in water, $G_{S,water}$	2.51	2.28	-	-	2.54, 2.56
Specific Gravity in alcohol, $G_{S,alcohol}$	-	2.34	-	-	-
10th Percentile Particle Size, D_{10} (mm)	0.003	0.003	0.003	-	0.0025
50th Percentile Particle Size, D_{50} (mm)	0.021	0.014	0.021	-	0.024
Coefficient of Uniformity, C_u	-	-	8.5	-	-
Coefficient of Curvature, C_c	-	-	1.1	-	-
Minimum Dry Density (kg/m^3) [1]	-	1099	-	-	-
Maximum Dry Density (kg/m^3) [1]	-	1442	-	-	-
Liquid Limit, *LL* (%)	21	28	-	25.02	-
Plastic Limit, *PL* (%)	-	22	-	-	-
Plasticity Index, *PI* (%)	-	6	-	-	-
pH	8.79	7	-	-	-
El. Cond., fluid (mS/m)	-	155	-	-	-
El. Cond., sediment (mS/m)	-	115	-	-	-
Ferromagnetic Content (%)	-	3.3	-	-	-
Vertical Hydraulic Cond., $k_{vertical}$ (cm/s)	-	$3.30 \cdot 10^{-5}$	-	-	$1.70 \cdot 10^{-4}$
Compression Coefficient, C_C [2,3]	-	-	-	0.053	0.013 – 0.042
Recompression Coefficient, C_r [2]	-	-	-	0.0030	0.0033
Vertical Coefficient of Consol., C_V (cm^2/s) [2,3]	-	-	-	0.5 - 4.3	-
Air Entry Pressure (kPa)	-	-	-	-	10
Proctor Optimum Moisture Content (%)					20.8
Proctor Maximum Dry Density (kg/m^3)					1417.8

[1] Based on method developed in EPRI (2014); [2] From consolidation tests with initial void ratios between 0.837 and 0.855; [3] Based on stress increments between 115 kPa and 850 kPa.

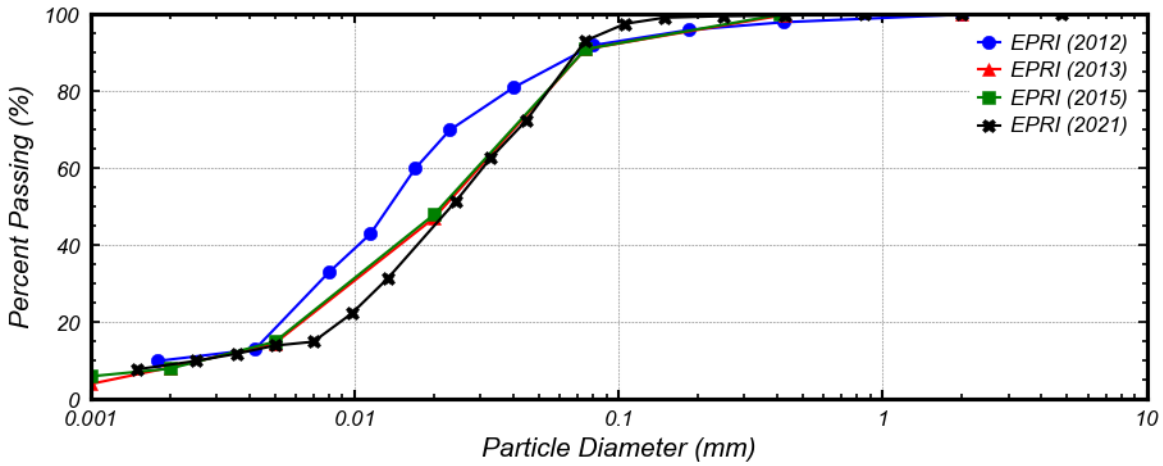

Figure 5. Grain size distribution curves of the fly ash studied.

2.2.2 Compaction Properties

A five-point standard Proctor test was performed by a commercial lab to determine maximum dry density and optimum water content for the ash. Ash shown in **Figure 6**, the maximum dry density is about 1.42 Mg/m^3, with an optimum water content of 20.8%.

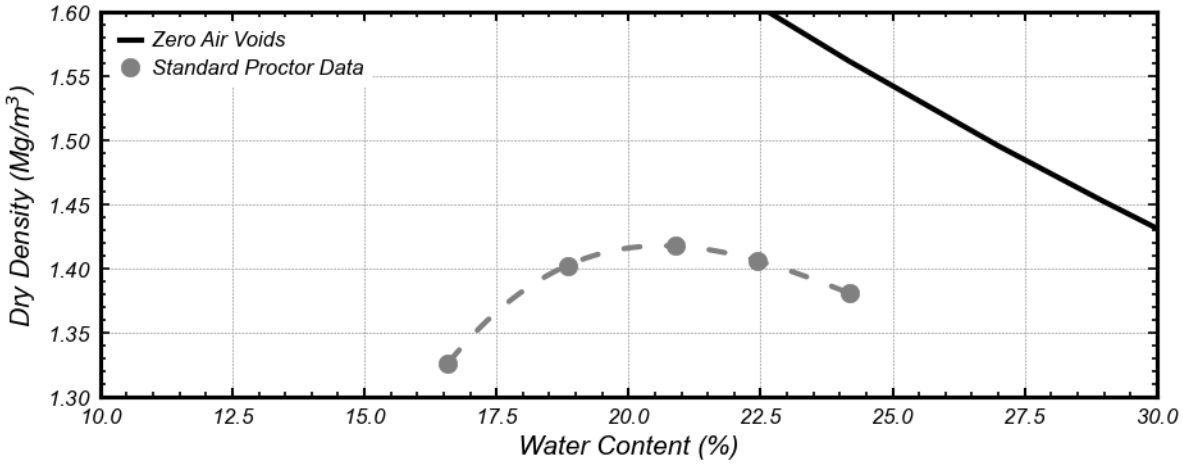

Figure 6. Standard Proctor compaction curve (EPRI 2021).

2.2.3 Consolidation Properties

Consolidation testing was performed at UC Davis and a commercial lab, with the results shown in **Figure 7**. For the UC Davis data, the compression index (C_c) was 0.053, the recompression index (C_r) was 0.003, and C_c/C_r was about 17.7. The coefficient of consolidation (C_v) was measured in some of the UC Davis test increments, with values determined to range from 0.5 to 4.3 cm^2/s. For the commercial lab data, C_c was measured as 0.013 and 0.042, with an increasing void ratio (e_0) leading to increasing compressibility (e_0 of 0.800 and 0.958 for the commercial lab data, respectively). C_r was measured to be about 0.003, similar to the UC Davis data. C_c/C_r ranges approximately from 4 to 14 for the commercial lab data.

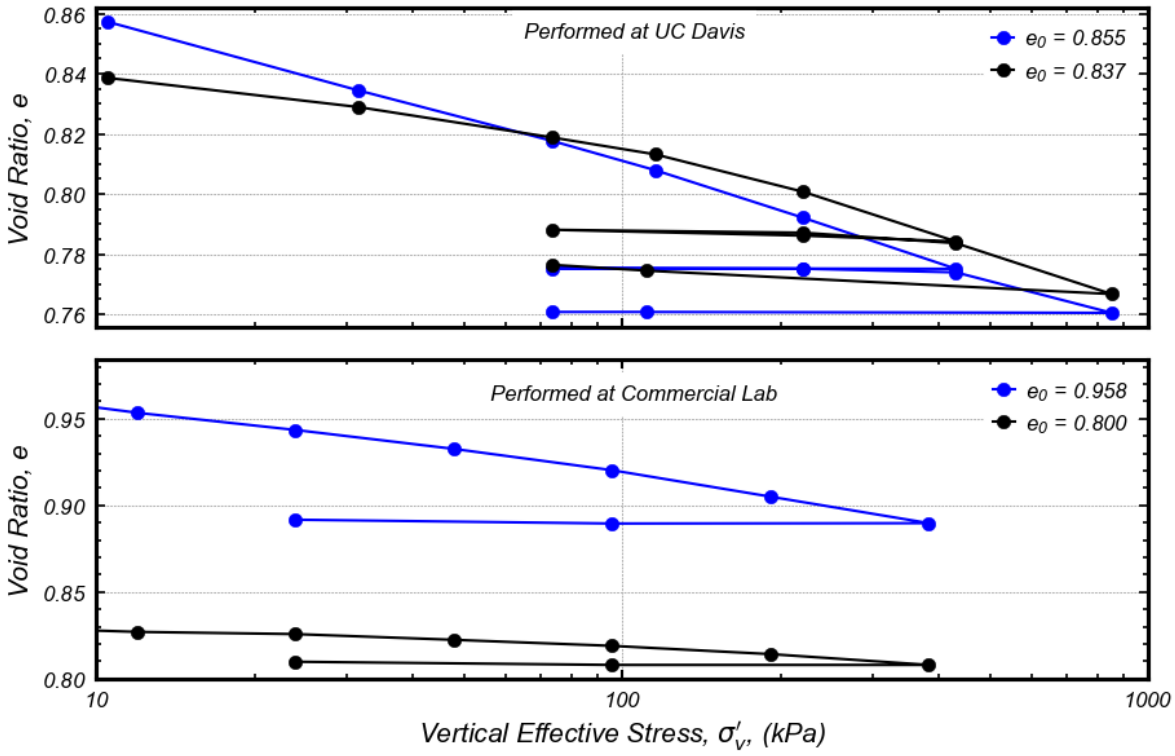

Figure 7. Consolidation test results (EPRI 2021).

2.2.4 Shear Strength Properties

Isotropically-consolidated, undrained triaxial compression (ICU-TXC) tests were performed in EPRI (2020 & 2021), with the results shown in **Figure 8** through **Figure 11**. Densities of the specimens ranged from 1.30 to 1.45 Mg/m^3, with confining stresses (σ'_{3c}) ranging from 207 to 556 kPa. In **Figure 10**, an M-line is plotted with a slope of 1.00, which corresponds to a critical state friction angle (φ'_{cs}) of 25.4°. As shown from **Figure 11**, all tests plot on the dense of critical side of the critical state line, with all void ratio – mean effective stress paths moving to the right during loading. Two possible critical state line (CSL) power functions are introduced as well in the plot, which will be used in later analysis. It should be noted that some of the tests had negative excess pore pressures limited by cavitation, as shown in **Figure 8** and **Figure 9**.

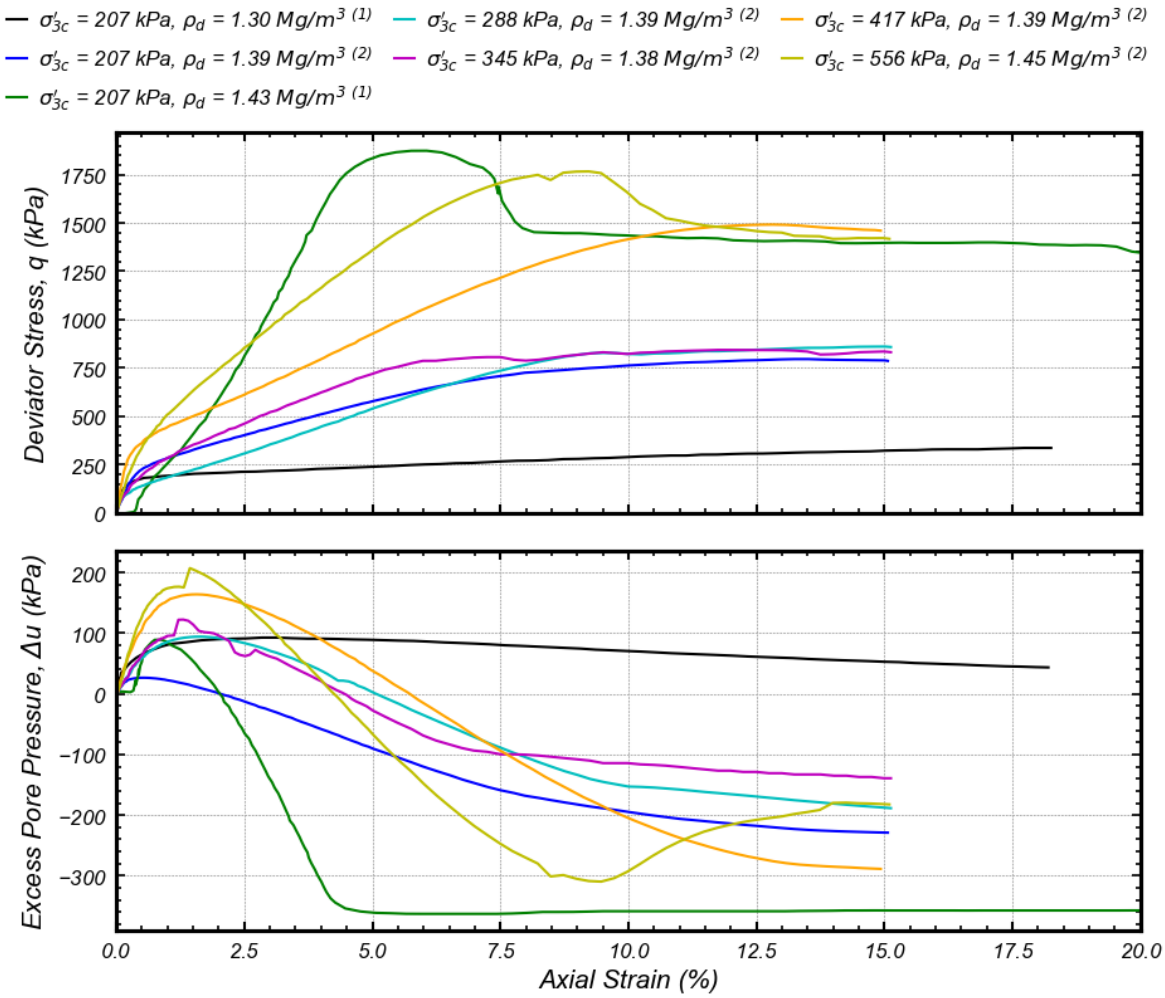

Figure 8. ICU-TXC tests: deviator stress and excess pore pressure (EPRI 2020 [(1)] and 2021 [(2)]).

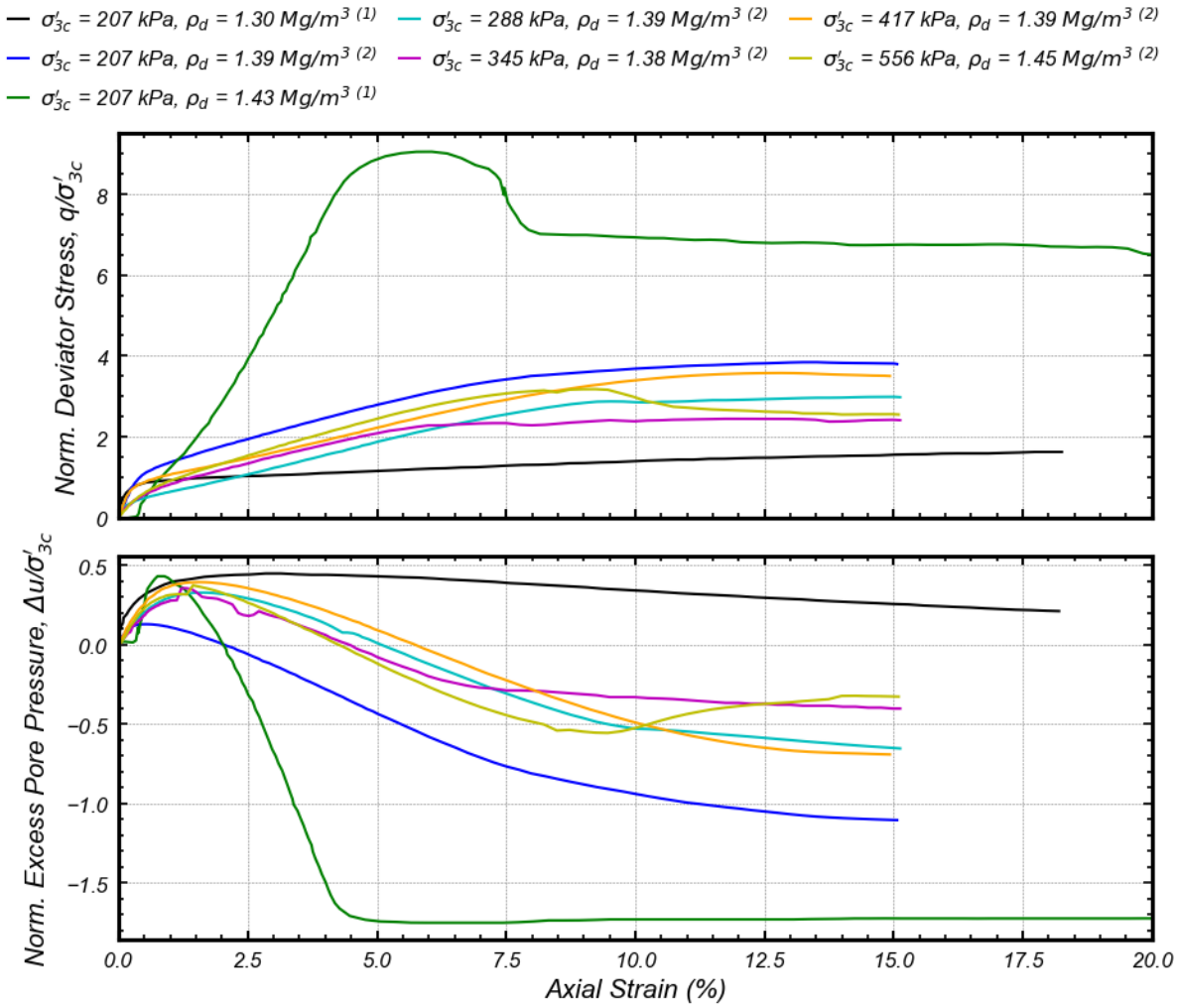

Figure 9. ICU-TXC tests: deviator stress and excess pore pressure normalized by consolidation stress (EPRI 2020 (1) and 2021 (2)).

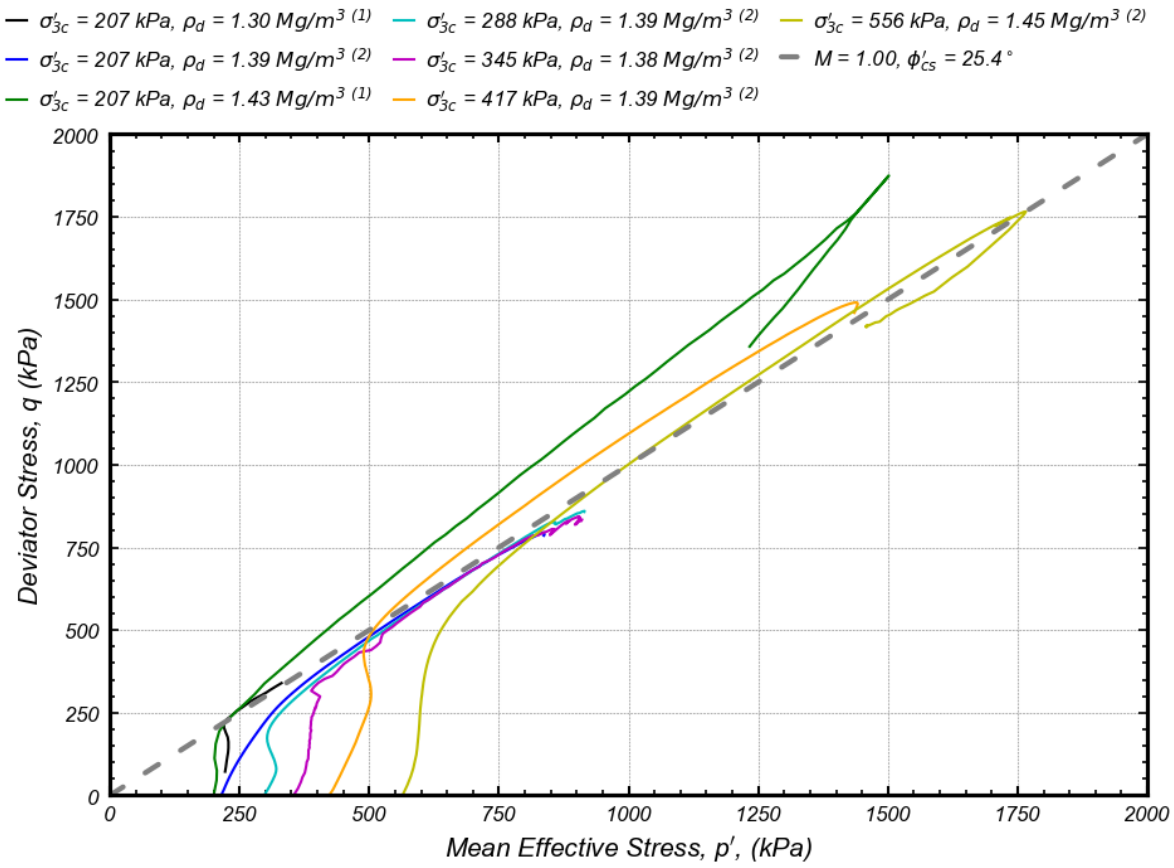

Figure 10. ICU-TXC tests: deviator stress vs. mean effective stress (EPRI 2020 [(1)] and 2021 [(2)]).

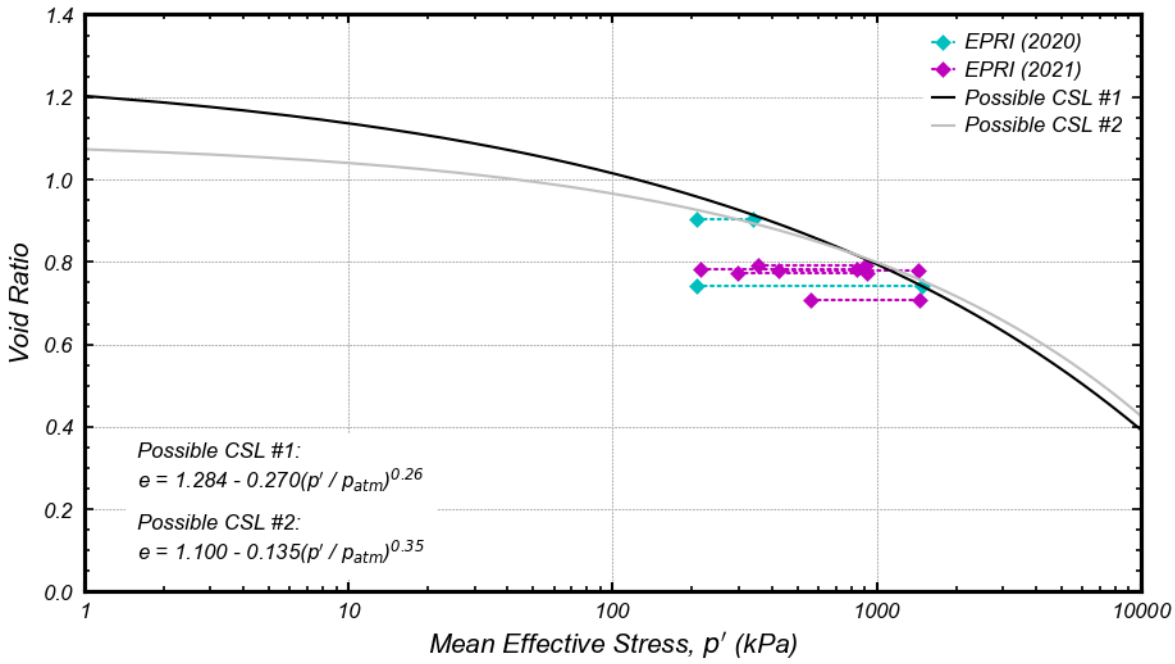

Figure 11. ICU-TXC tests: void ratio vs. mean effective stress with possible CSL lines. Note that all stress paths move from left to right.

2.2.5 Hydraulic Conductivity and Soil-Water Retention Curve

Vertical hydraulic conductivity, k_v, was determined in EPRI (2012 & 2021). EPRI (2012) determined a k_v value of $3.3 \cdot 10^{-5}$ cm/s but did not specify the water content or void ratio of the sample tested. EPRI (2021) found a k_v value of $1.7 \cdot 10^{-4}$ cm/s for a sample with a water content of 33.1% (with a void ratio calculated as 0.83). EPRI (2021) also performed hanging column, pressure plate, and relative humidity (Rh) box tests on the ash. This data was used to develop a soil-water retention curve (SWRC) for the material. Some uncertainty is present in the portion of the curve between volumetric water contents of 1 to 36%, due to a lack of data. From the given data, the air entry pressure can be approximated as 10 kPa.

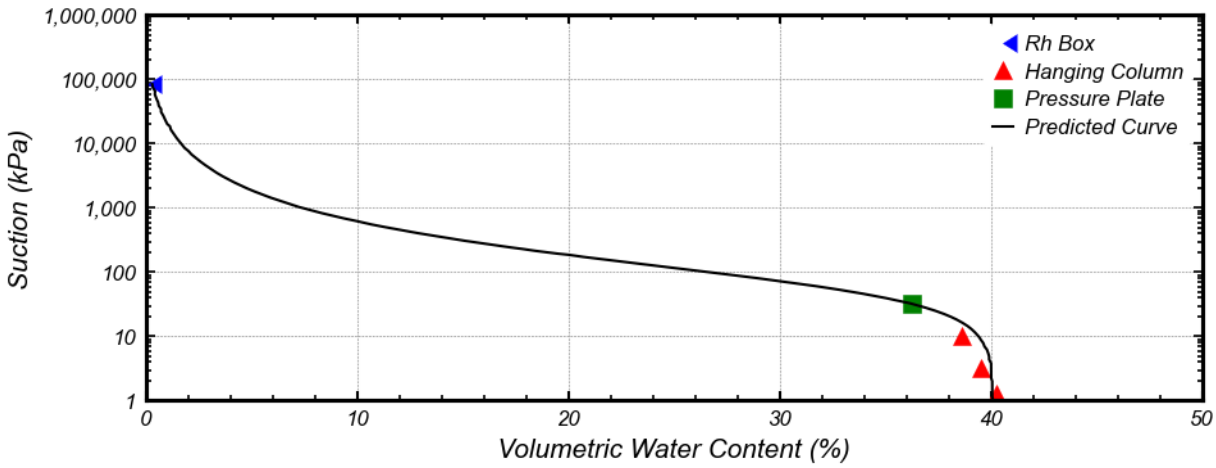

Figure 12. Soil-water characteristic curve (SWRC).

2.3 Specimen Preparation

To prepare the model impoundments, ash was combined with deionized water to form a slurry to place during deposition. Target water contents were determined for each slurry, with the mass percentage of solids being estimated from the ash source by water content tests (per ASTM D2974-20 for all water content tests in this thesis), and the water added being based on the measured mass percentage of solids.

Prior to centrifuge model preparation, slurry deposition trials were performed using 5-gallon buckets to determine the relationship between initial slurry water content and settled ash density. Slurries of water contents ranging from 30% to 400% were used in the trials. Figure 13. shows the calculated slurry dry density versus slurry water content (left) and settled dry density of the ash versus settled water content of the ash (right). Height readings were taken in the 5-gallon buckets with a plumb bob to perform the trials at specific volumes of water to increase the accuracy of measured volumes. The slurry dry densities were determined by dividing the total mass of solids by the estimated volume of slurry. Settled dry densities were determined by measuring the volume of the settled ash using the light-weight plumb bob (with a lighter weight used to increase the

accuracy of the height measurements of the soft ash mud line) and dividing the deposited mass of solids by this volume. An assumption in this method is that all solids have settled out of the slurry water, which was found to be a reasonable assumption during the specimen preparation of test FR06. The settled water content was measured by taking samples of the settled ash (after draining of pooled water) and performing water content tests.

Figure 14 shows the settled dry density measurements plotted against the slurry water contents, with a logarithmic trendline fitted to the data. The logarithmic trendline has an R^2 value of 0.50. Despite the poor fit, the trendline helps show the dependence that settled dry density has on initial slurry water content, with greater slurry water contents generally resulting in lower settled dry densities. Based on this trend, denser models were poured with lower slurry water contents in a single lift, while looser models were poured with higher slurry water contents and required multiple lifts (due to a lower ratio of settled ash volume to slurry volume).

For all tests performed in this study, slurry was prepared in 5-gallon buckets and subsequently poured into the ash container (in EPRI (2021), denser models were poured using an industrial mixer). The slurry in test FR06 (loose target density) was allowed to sit for 12 to 24 hours between lifts, with excess water siphoned off the settled ash before pouring of the next lift. **Figure 15** shows settled ash from the prior lift, which was exposed after siphoning of excess pooled water.

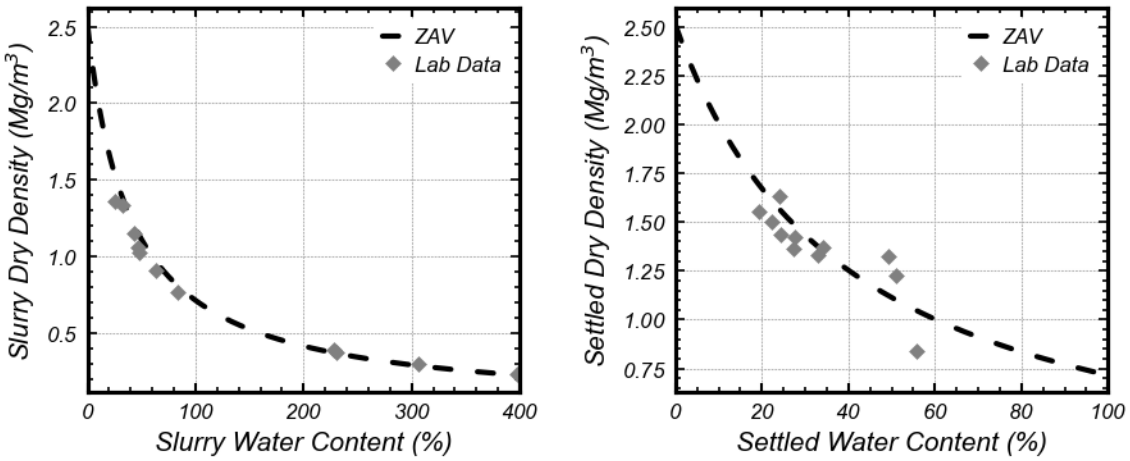

Figure 13. Left: Slurry dry density vs. slurry water content. Right: Settled dry density vs. settled water content.

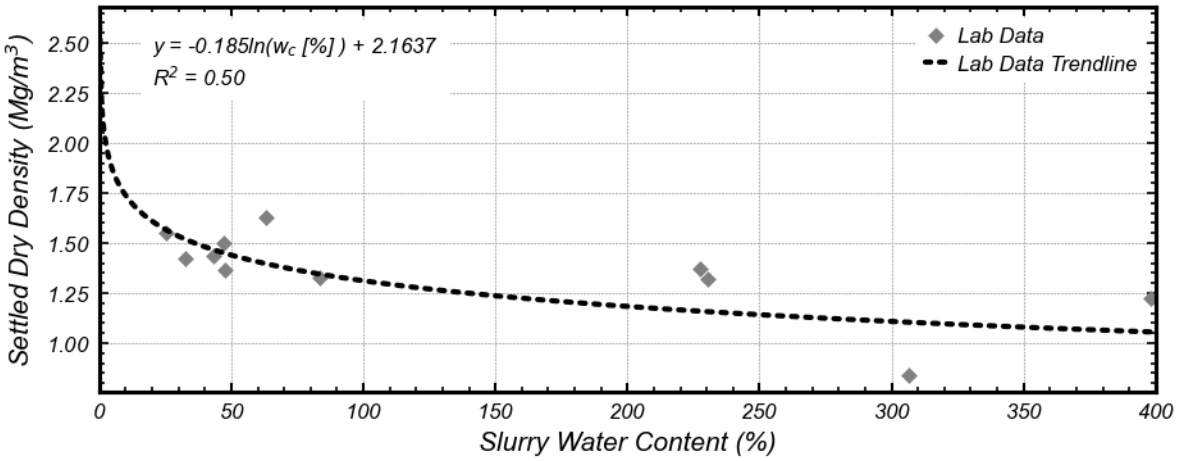

Figure 14. Settled dry density vs. slurry water content.

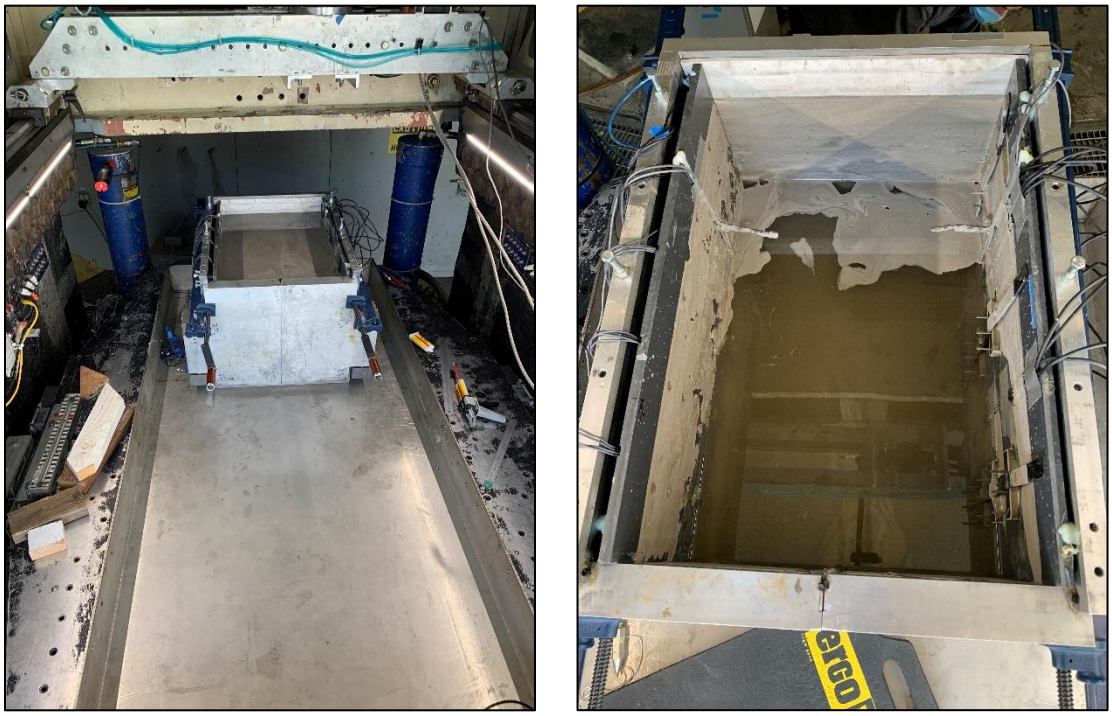

Figure 15. Left: Ash lift poured in container. Right: Excess water removed before pouring lift.

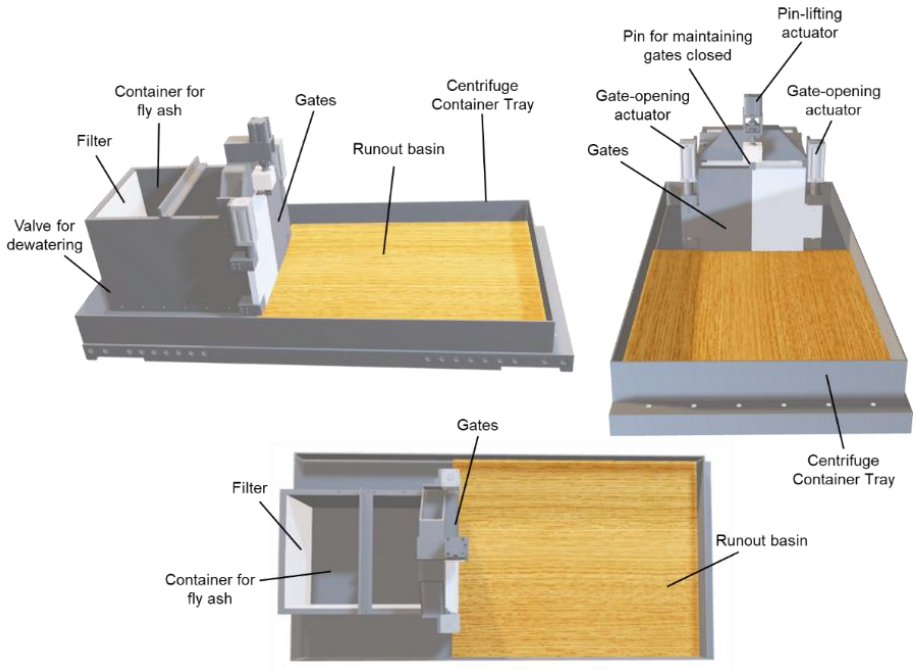

Figure 16. 3D visualization of novel centrifuge system (EPRI 2021).

2.4 Fly Ash Impoundment Model for Centrifuge Testing

To model failure of an ash containment structure in practice, a novel system was created at the CGM that subjects an impoundment to a sudden loss of lateral confinement. **Figure 16** shows three dimensional views of the system. The container for the fly ash is constructed of aluminum. A dewatering port is installed at the back of the container, which allows for in-flight draining using a pneumatic valve (the volume of water removed through this valve cannot be tracked during flight). This water exits from a line attached to the container tray. A porous plastic filter sheet is attached to the inside of the container between the dewatering valve and the deposited ash. Gates were installed at the front of the container using hinged connections, which can be opened when desired during flight. The gates are opened by a combination of rotary pneumatic actuators (with a stored air supply in an accumulator) and lateral pressure exhibited by the deposited ash. The gates are held in place by a metal pin during flight, which is hydraulically retracted at the time the gates are desired to be open (after air is pumped into the rotary pneumatic actuators). The front gates are sealed with 6.35 mm O-rings and high vacuum grease. Proof testing with water was performed to verify the seals adequacy prior to deposition of the ash. **Figure 17** shows the overall system prepared prior to flight (left) and the inside of the container during ash deposition (right). The opening of the gates simulates a sudden loss of lateral confinement of the modeled deposit, which acts as an idealized failure of a containment structure.

In prototype scale, the container houses a deposit 27.6 m in width, 24.0 m in length, and up to 24.0 m in height (model scale is 0.67 m length, 0.46 m width, and up to 0.40 m height). A smooth runout basin was constructed with plastic and has dimensions of 73.8 m length by 58.8 m wide (model scale is 1.23 m length and 0.98 m width). Plastalina modeling clay is placed at the

point of contact of the gates and the container tray, which was shown by EPRI (2021) to adequately dampen the impact of the gates and the sides of the container tray.

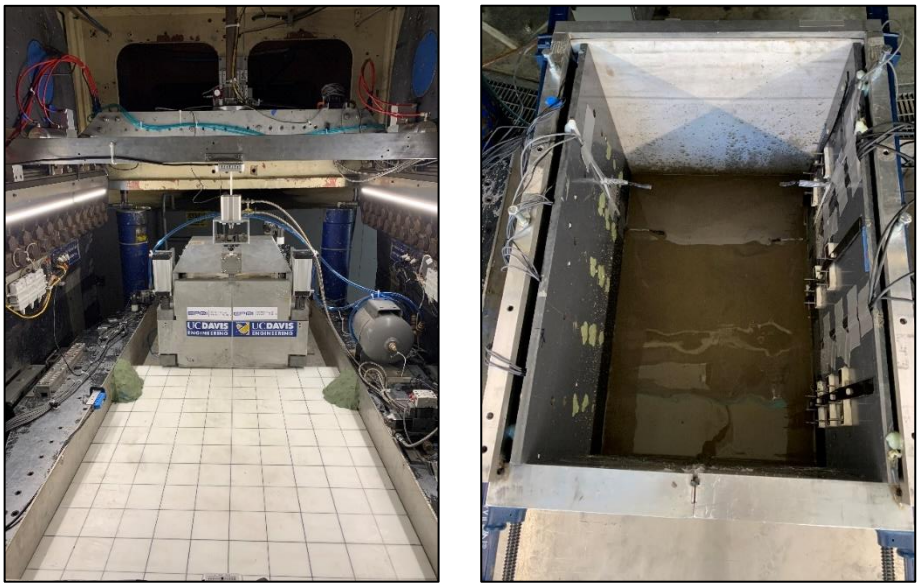

Figure 17. Left: final setup of centrifuge system prior to flight. Right: inside of container during ash deposition, with porous plastic filter at the top of the photo.

2.5 Instrumentation for Centrifuge Testing

2.5.1 Shear Wave Velocity

Shear wave velocity was measured using piezoelectric bender elements. Two pairs were used in test FR06, with one element in a pair sending a square wave and the other element acting as a receiver. Each pair ran separately during testing. The bender elements are made from nickel-electrode, center accessed, y-pooled elements, which are coated in a waterproof epoxy. **Figure 17** (right) shows the bender elements prior to being submerged in ash slurry, protruding from the container walls. The shear wave velocity (V_s) is defined by the following equation:

$$V_S = \frac{\textbf{Distance between benders}}{\textbf{Arrival time} - \textbf{lag time} - \textbf{trigger time}} \quad (1)$$

The arrival time is the time when the signal reaches the receiver bender element, and the lag time is the time it takes for the signal to travel from the source bender element to the receiver bender element (measured by running them in contact with each other in air). As discussed in section **3.4**, only the shallow bender pair worked during FR06. The lag time was calculated to be $7.5 \cdot 10^{-6}$ seconds for the shallow bender pair prior to specimen preparation, and the distance between the source and receiver was 0.246 m. The sampling frequency of the bender elements were set to 10^6 Hz.

2.5.2 Cone Penetration Test

Using a miniature CPT probe designed by Carey et al. (2018), shown in **Figure 18**, tip resistance (q_c) profiles with depth were measured in the ash deposit. The load at the tip of the probe is transferred through an isolated inner rod to an external load cell, separating the tip resistance from the combined resistance of the tip and the shaft. Pore pressure and friction sleeve measurements are not obtained with this system. The diameter of the tip used in test FR06 is 10 mm in model scale. The sampling rate used was 5,000 Hz.

Figure 18. Miniature CPT probe used for centrifuge testing (EPRI 2021).

The CPT probe was pushed in two locations in test FR06, with each location having a different penetration velocity. Based on EPRI (2021), the normalized penetration velocity (*V*) for the tests was determined by the following relationship (DeJong and Randolph 2012):

$$V = \frac{vd}{C_V} \quad (2)$$

The penetration velocity is *v*, *d* is the probe diameter, and C_V is the horizontal coefficient of consolidation. Price et al. (2019) performed centrifuge tests on silty soils and showed that a *V* of 40 and 2 can be associated with approximate undrained and drained behavior, respectively. Based on the centrifuge system's actuator capabilities, CPT soundings at rates of 100 mm/s and 2 mm/s were performed. Based on these velocities, a C_V of 0.6 cm^2/s for this ash, and a probe diameter of 1 cm, the normalized penetration velocities for undrained and drained soundings are 16.7 and 0.33, respectively. While the undrained value is slightly outside the bounds provided by DeJong and Randolph (2012) and Price et al. (2019), it is considered here as representative of undrained conditions.

2.5.3 Tensiometers

Miniature SMD pressure sensors (MS5407-AM, Intersema 2007) were used as tensiometers to measure pore pressures and suction in the ash deposit during flight. The sensors consist of a silicon micromachined pressure die attached to a ceramic carrier protected by a metal cap. Similar to Jacobsz (2018), porous ceramic stones with an air entry value of 100 kPa were glued to the sensors, with the exposed portion of the sensor being coated in a two-part epoxy. Exposed wires were wrapped in heat shrink tubing. **Figure 19** shows miniature SMD pressure sensor and a constructed tensiometer used for test FR06. The ceramic stones were saturated, and the sensors calibrated using the following procedure:

1. The constructed sensors were placed into a sealed metal chamber, with the sensors dangling vertically in the chamber close to the bottom and sealed with a test tube stopper.
2. A vacuum pressure of -80 kPa was applied, with the vacuum left running and connected to the chamber with a switch valve.
3. After closing the valve to the vacuum, gaseous carbon dioxide was flushed into the chamber at a pressure of about 60 kPa and left to sit for 5 to 10 minutes.
4. The valve to the carbon dioxide was closed, and then steps 2 and 3 repeated for an hour.
5. After flushing of carbon dioxide was completed, the vacuum was applied to the chamber and the valve to the vacuum closed after the vacuum pressure was reached.
6. Deaired, deionized water was siphoned out of a container into the calibration chamber, with enough water to fill the chamber between one half to two thirds of its capacity.
7. The chamber was placed under an air pressure between 200 to 250 kPa for a minimum of one hour.
8. Calibrations were performed on the sensors, and step 7 was repeated as needed if the stones did not appear to be saturated (hysteresis in the calibration curves).
9. After calibration, the chamber was allowed to return to atmospheric pressure, and the sensors were stored in deaired, deionized water until they were placed in the model.

Figure 20 shows the equipment necessary for steps 1 through 6, which is different than the typical pore pressure transducer calibration procedure used at the CGM. Care was taken during placement of tensiometers in the model to not allow for desaturation of the stones. The tensiometers were then placed into the corresponding sensor board with modeling clay to hold them in place (see **Figure 17**, right). Readings from the tensiometers were taken at sampling rates up to 5,000 Hz. At large sampling rates, the data was filtered using a fourth-order Butterworth low-pass filter, using

a low-pass frequency of 50 Hz. **Figure 21** shows the location of the tensiometers within the container for FR06.

Figure 19. Left: miniature SMD pressure sensor (MS5407-AM, Intersema 2007). Right: constructed tensiometer for FR06.

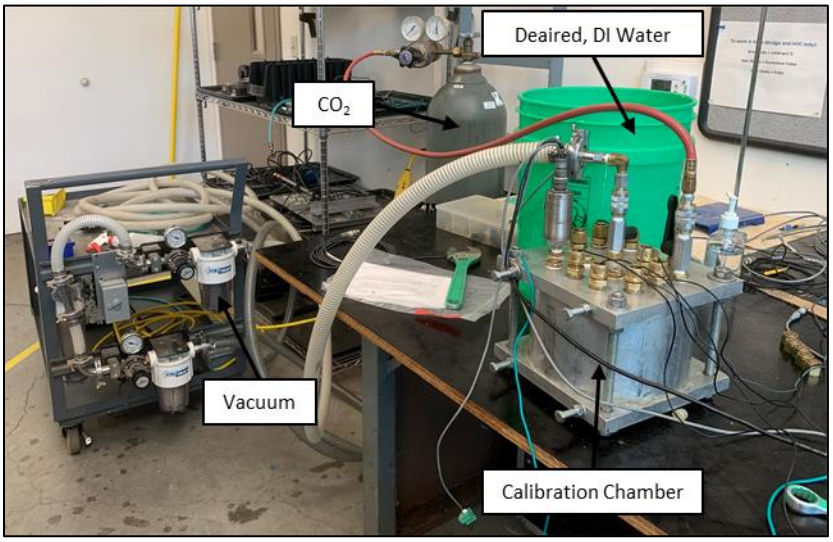

Figure 20. Tensiometer calibration system.

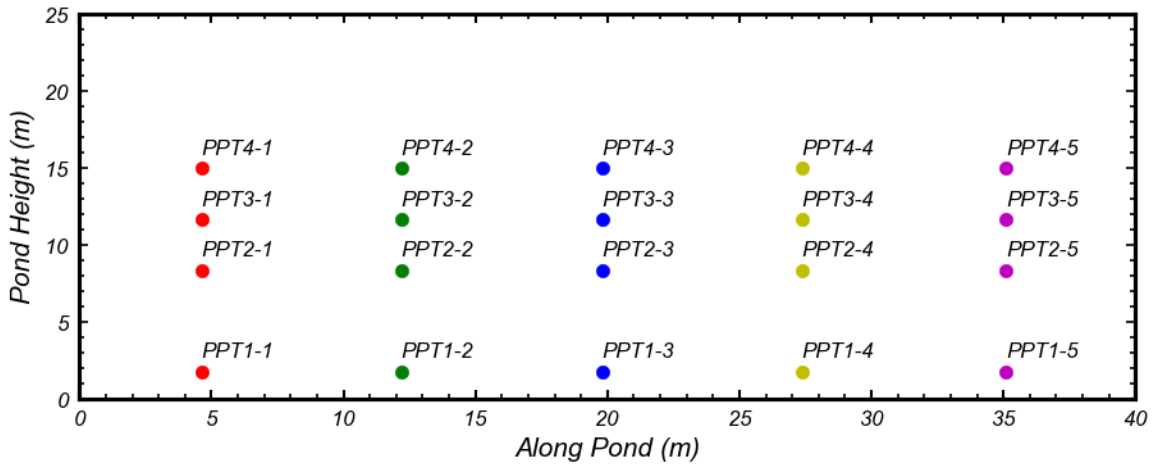

Figure 21. Tensiometer locations for test FR06.

2.5.4 Moisture Probes

ECH$_2$O GS3 Volumetric water content sensors from METER Group (2018) were used to estimate water contents of the deposited ash. The sensors measure the dielectric constant of the ash using capacitance/frequency domain technology. Temperature is measured using an internal thermistor and electrical conductivity by using a stainless-steel electrode array. **Figure 22** shows a schematic of a single sensor. The sensors measure dielectric permittivity (unitless), temperature (°C), and electrical conductivity (µS/cm) of the surrounding media. Samples were taken from the sensors at 0.01 Hz during specimen preparation and 0.1 Hz during flight and runout testing. The locations of the moisture probes are shown in **Figure 23**.

For unusual soils (such as fly ash), a soil specific calibration is necessary to correlate electrical readings from the moisture probes with water content. Additionally, with the metal probes at the stock length, dielectric permittivity and conductivity readings of the fly ash tested were found to reach a saturation level at a water content lower than desired by EPRI (2021). To explore potential options to increase the water content the electrical readings saturated at, EPRI tested the sensors with their metal probes cut to lengths of 10 mm and 20 mm. **Figure 24** shows

these results compared to uncut probes, with decreasing metal probe lengths resulting in saturation of dielectric permittivity and conductivity at higher water contents. Based on this data, the sensors used for centrifuge testing were cut to approximate probe lengths of 20 mm by EPRI but were not able to be cut to uniform lengths for each sensor. It is noted that the readings become non-unique at a water content of about 30% for dielectric permittivity and about 65% for conductivity, as shown in **Figure 25**.

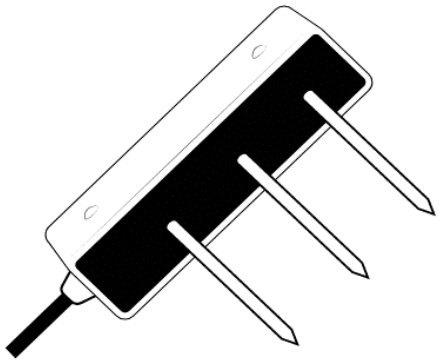

Figure 22. Drawing of GS3 moisture probe (METER 2018).

Due to uneven cut probe lengths between individual sensors, calibrations were also required for each individual sensor. A calibration procedure was undertaken to relate water content to the measured dielectric permittivity and conductivity of the moisture probes with approximate metal probe lengths of 20 mm, based on data from EPRI (2021) and this study. Using ash at water contents between 0 to 50%, numerous conductivity and dielectric permittivity readings were taken in a small plastic container (20 cm width, 20 cm length, and 10 cm depth). A logistics function was fitted to the dielectric permittivity data. A combination of linear logistic, logistic, and an average between the two was fitted to the conductivity data. **Appendix A** details the process to calibrate the sensors, the lab calibration data, and specific calibration factors used. The resultant

calibration curves for each individual sensor are shown in **Figure 26**. Due to dielectric permittivity readings saturating earlier than conductivity and hypothesized effects of density on dielectric permittivity, only conductivity was used to determine water content. **Figure 27** shows the non-linearity between dielectric permittivity and conductivity based on the laboratory calibration data, which demonstrates the quicker saturation of readings through dielectric permittivity than conductivity.

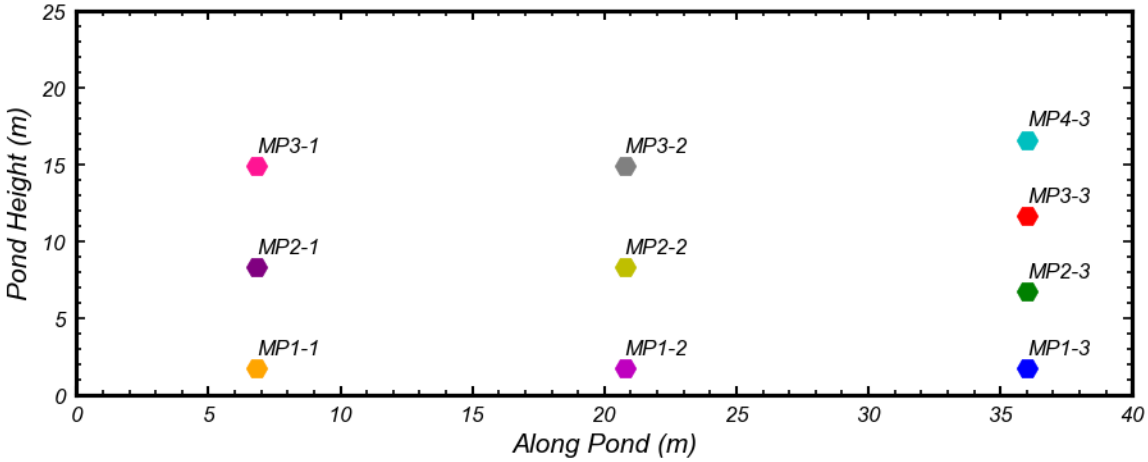

Figure 23. Moisture probe locations for centrifuge and 1 g tests.

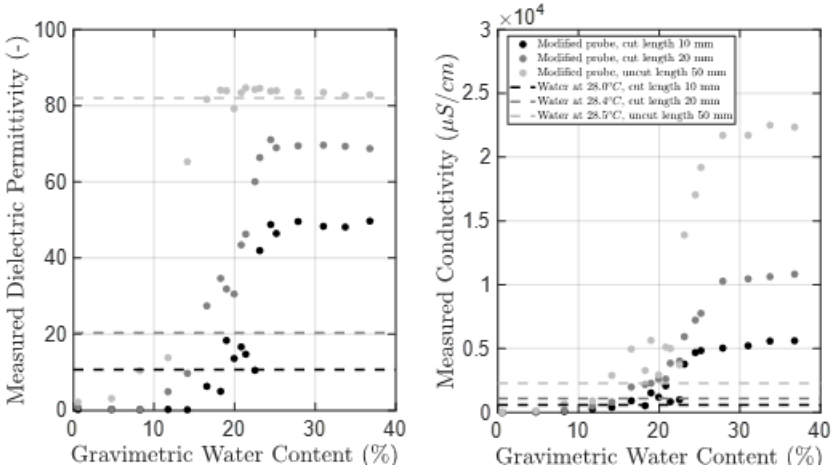

Figure 24. Effect of metal probe length on electrical readings. Left: dielectric permittivity. Right: conductivity (EPRI 2021).

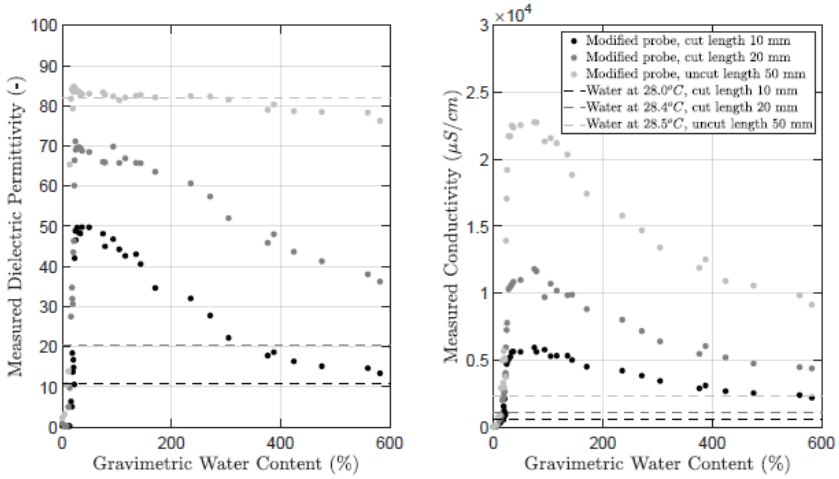

Figure 25. Non-uniqueness of electrical readings with water content. Left: dielectric permittivity. Right: conductivity (EPRI 2021).

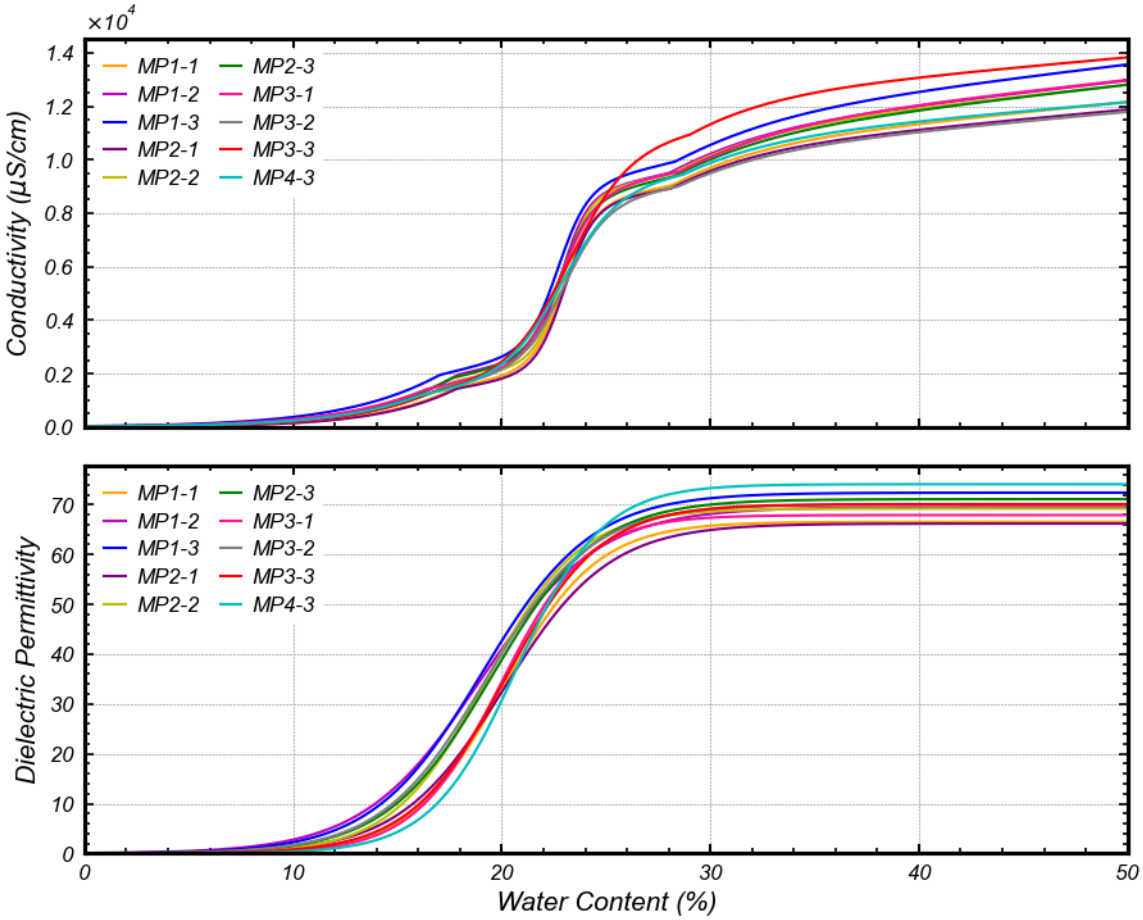

Figure 26. Calibration curves for determining water content from dielectric permittivity and conductivity from moisture probes (only conductivity was used in this study), based on data from EPRI (2021) and this study.

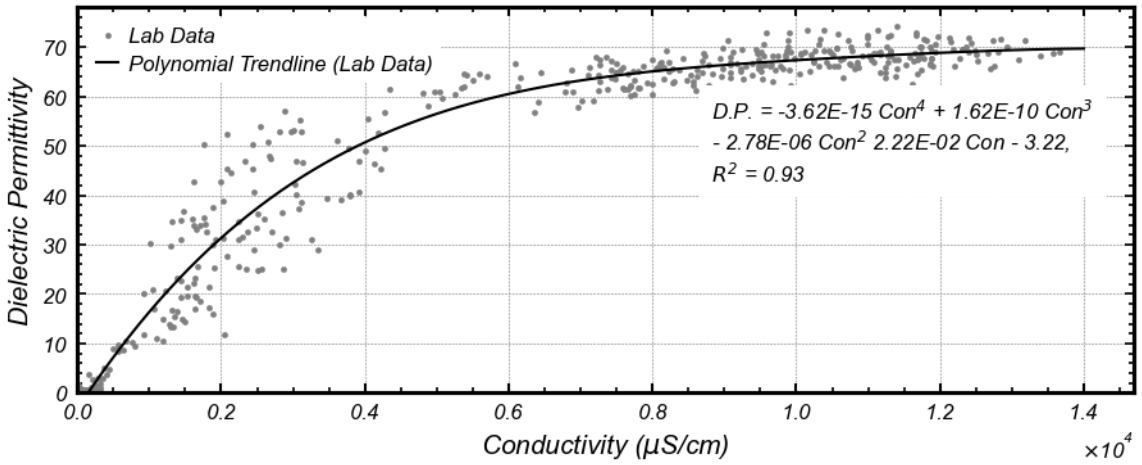

Figure 27. Dielectric permittivity vs. conductivity for laboratory data, based on data from EPRI (2021) and this study.

2.5.5 High Frame Rate Cameras

GoPro HERO3 cameras with capture rates of 240 frames per second were used to visually record the centrifuge test. Three cameras were used: one at the front of the container tray, one at the top of the back portion of the container, and one focused on the water line exiting the dewatering port.

2.5.6 Depth-Sensing Cameras

Intel RealSense™ D435 Depth Cameras (**Figure 28**) were used to record the centrifuge test. The cameras use stereoscopic vision technology, which calculates distance to individual pixels by using two parallel viewports and disparities between matching key points in the corresponding images, as shown in **Figure 29** (Dorodnicov 2018). Four cameras were used, each with a capture rate of 30 frames per second. The distance from the cameras to the exposed surfaces of the ash deposit are measured by the cameras and recorded in the Intel RealSense™ software. The data is then analyzed with a combination of MATLAB and Python codes to produce surface profiles and volumes of material exiting the container, using relative positions of a fixed object to

the known distances of the cameras. The cameras also record standard RGB footage in addition to the depth-measured data.

2.6 Scaling Laws for Centrifuge Modeling

From Kutter (1995), the scaling laws for centrifuge modeling can be written in terms of the scaled acceleration applied to the model. This scaled acceleration is typically expressed in terms of the ratio of increased acceleration to Earth's gravitational acceleration. This scaling factor *N* is used to convert measured properties at the model scale (dimensions as constructed) to prototype scale (dimensions being modeled). The following equations (Garnier et al. 2007) show the relevant scaling laws for the centrifuge testing performed (with model scale denoted with subscript *M*, and prototype with subscript *P*):

$$\boldsymbol{L_P = NL_M} \quad (\mathbf{3})$$

$$\boldsymbol{Z_P = NZ_M} \quad (\mathbf{4})$$

$$\boldsymbol{V_P = N^3 V_M} \quad (\mathbf{5})$$

$$\boldsymbol{\sigma_P = \sigma_M} \quad (\mathbf{6})$$

$$\boldsymbol{\rho_P = \rho_M} \quad (\mathbf{7})$$

$$\boldsymbol{t_P = Nt_M} \quad (\mathbf{8})$$

In the above, L is length, Z is depth within the ash deposit, V is volume, σ is normal stress, ρ is density, and t is time. As shown by the lack of the scale factor in Equations 4 and 5, stress and density do not scale differently in centrifuge modeling. The scaling law used for time is for dynamic processes, rather than diffusive processes. EPRI (2021) and the current study performed all tests at 60 g.

2.7 Fly Ash Impoundment Model for 1 g Testing

The system used for centrifuge testing was also used for 1 g runout tests, with minor modifications. The hydraulic pin used to hold the gates was removed and a pneumatic linear actuator was used to assist the opening of the gates (**Figure 30**). Dewatering was not performed during the 1 g tests, but excess water was siphoned prior to opening of the gates (as much as possible without disturbing the deposit). Slurry water content was varied between the three tests, ranging from 32% to 48%.

Figure 28. Intel RealSense™ D435 Depth Camera.

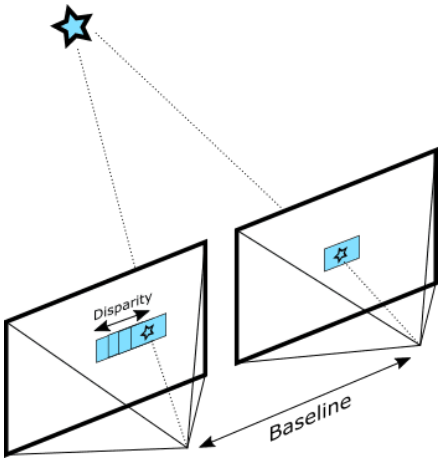

Figure 29. Demonstration of stereoscopic vision (Dorodnicov 2018).

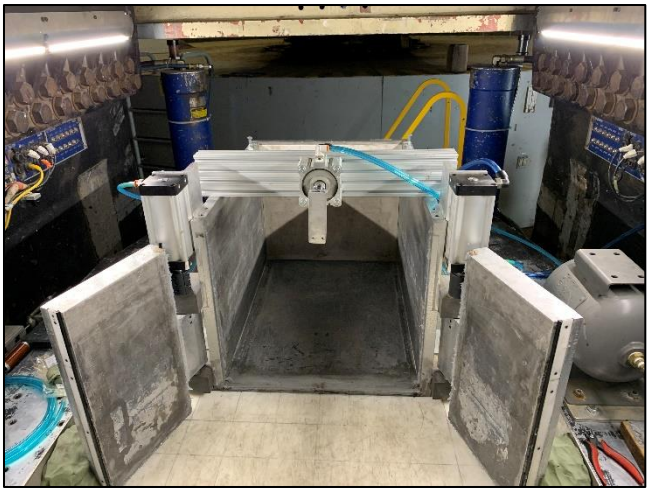

Figure 30. Modified fly ash impoundment model for 1 g tests.

2.8 Instrumentation for 1 g Testing

Due to the lower soil stresses in the 1 g tests than the centrifuge tests, bender elements, tensiometers, and cone penetrometers were not used. The same moisture probe system and depth-sensing cameras were used for the tests, as well as a T-Bar penetrometer. AXIS cameras were used in place of GoPro HERO3 cameras.

2.8.1 T-bar Penetration Test

Due to relatively low cone penetration resistances expected in the 1 g tests, a full-flow, T-bar penetrometer was used to increase the measured accuracy of strength parameters. The T-bar penetrometer was first used in centrifuge testing by Stewart and Randolph (1991) to profile soft clay and has been shown to have increased accuracy in very soft soils due to a larger volume of soil engaged during penetration (DeJong et al. 2011). From Randolph (2004), the penetration resistance of a T-bar is corrected for the imbalance in force above and below the probe with the following relationship:

$$q_{net} = q_m - [\sigma_{v0} - u(1-\alpha)]\left(\frac{A_s}{A_p}\right) \quad (9)$$

The measured tip resistance is q_m, σ_{v0} is the total overburden stress, u is the pore-water pressure, α is the load cell area ratio (similar to the α parameter for cone penetration testing), A_s is the projected shaft area, and A_p is the projected area of the penetrometer. Since u_2 is not measured, hydrostatic pressure (u_0) was used to calculate the penetration resistance, which leads to error in soft sediments due to generation of excess pore pressures (DeJong et al. 2011). **Figure 31** shows the penetrometer used for the 1 g tests, which has a projected penetrometer area of 2.7935 cm^2, a projected shaft area of 0.2827 cm^2, and a load cell area ratio of 0.60. An external load cell was used to measure the force applied to the penetrometer. The sampling rate used was 5000 Hz.

Figure 31. T-bar penetrometer used for 1 g tests.

2.8.2 AXIS Video Cameras

Two AXIS P1204 cameras were used to visually record the runout of the 1 g tests. One camera was placed directly in front of the container, attached to the container tray, and the other above and to the side of the system, aimed at the gates.

3 CENTRIFUGE TESTING

One centrifuge test (FR06) was performed to investigate the effects of dewatering on a looser ash specimen (compared to centrifuge models in EPRI 2021) and its runout behavior. As described in this chapter, the measured properties and responses were significantly different from that of a similar loose specimen previously tested due to the effects of dewatering as well as differences in initial density. Specifically, CPT tip resistances and stiffness increased in model FR06 in relation to the previously tested loose ash model, dilative pore pressure behavior occurred above and near the water table, and contractive pore pressure behavior occurred below the water table. Results from the five centrifuge tests are compared at the end of the chapter.

3.1 Procedural Sequence for FR06

Specimen preparation and testing for FR06 was conducted in the following order:

1. The container and container tray were loaded onto the arm of the 9-m centrifuge, with the container sealed and held closed by heavy duty pipe clamps.
2. The moisture probes, tensiometers, and bender elements were installed in the interior of the container, with the moisture probe wiring hooked up and the sensors ready to use during ash deposition.
3. Fly ash slurry was deposited into the container over the course of 11 days by the procedure described in section **2.3**. Lifts were poured at 12- to 24-hour intervals as needed. The moisture probes took readings during this process. Water content tests were performed on siphoned water to ensure a negligible mass of solids was being removed from the impoundment.
4. The tensiometers and bender elements were attached the DAQ system on the centrifuge arm, and the remaining instruments (CPT probe, high frame-rate cameras, depth-sensing cameras)

were installed in the proper locations. The rotary pneumatic actuators and the hydraulic pin were attached to the container, and the pipe clamps removed.

5. The model was spun up in steps to 20 g, 40 g, and 60 g accelerations. Bender element readings were performed at each level after stabilization of the applied acceleration.
6. Dewatering was performed in flight to a target water table of 59% of the height of the impoundment.
7. Two CPT soundings were performed after dewatering, at velocities of 100 mm/s and 2 mm/s.
8. All instrumentation was set to its maximum desired sampling frequency, and all cameras were set to record footage.
9. The pneumatic actuators were pressurized, with the air pressure monitored within the upstream accumulator and allowed to stabilize. The hydraulic pin was then retracted to allow the gates to open.
10. The gates opened and fly ash runout was allowed to occur until further changes were deemed unlikely (approximately 29 minutes in model time for FR06).
11. The model was spun down, with the centrifuge decreasing acceleration under its own weight.

3.2 As-Constructed Deposit Properties

During specimen preparation, masses of solid ash and water were tracked during preparation of the slurry, with water contents tests of the slurry used to determine the masses. The target slurry water content was 225% for FR06 but was measured to be 270%. However, some error may be present in these measurements, as ash was visibly observed to settle within the ladles used to take water content samples. The settlement of solids within the 5-gallon buckets could have resulted in higher water content measurements than what is present. Height measurements were taken of the impoundment using a light-weight plumb bob, which was then multiplied by the

cross-sectional area of the container to determine the volume of the impoundment. The deposit was determined to have the following properties: bulk density (ρ_{total}) of 1.80 Mg/m^3, water content of 34.0%, dry density (ρ_{dry}) of 1.35 Mg/m^3, and an impoundment height of 19.6 m (H_I, prototype scale). The water content was calculated using recorded masses of water and solids. Dry density was calculated using the calculated water content and assuming zero air voids, which was then used to calculate the bulk density. **Figure 32** and **Figure 33** show how the measured density and water content for the FR06 model compare to the laboratory data, with the data falling within previously observed trends. Note that FR06 plots directly on the zero air voids line in **Figure 32** due to the method of calculating the settled dry density.

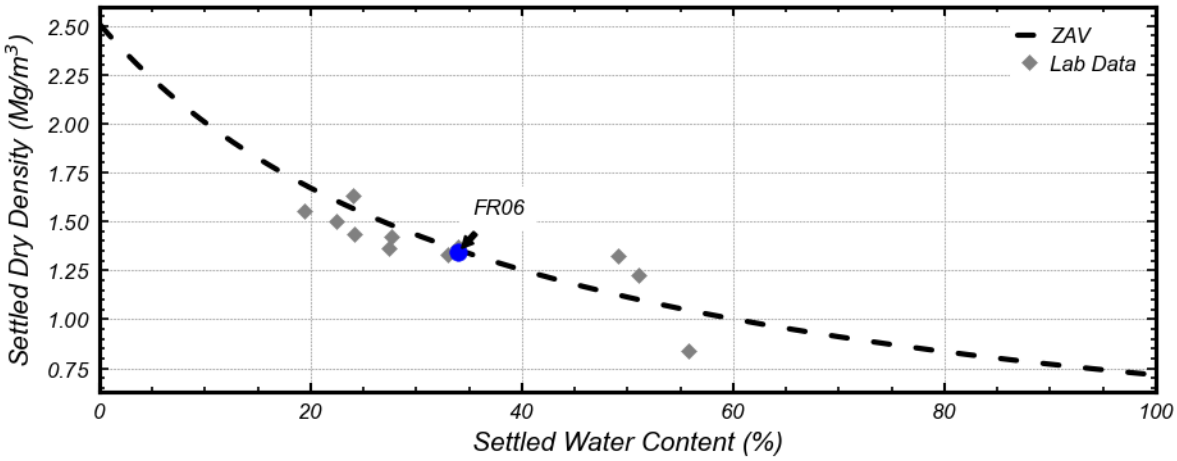

Figure 32. Settled dry density vs. settled water content, with FR06.

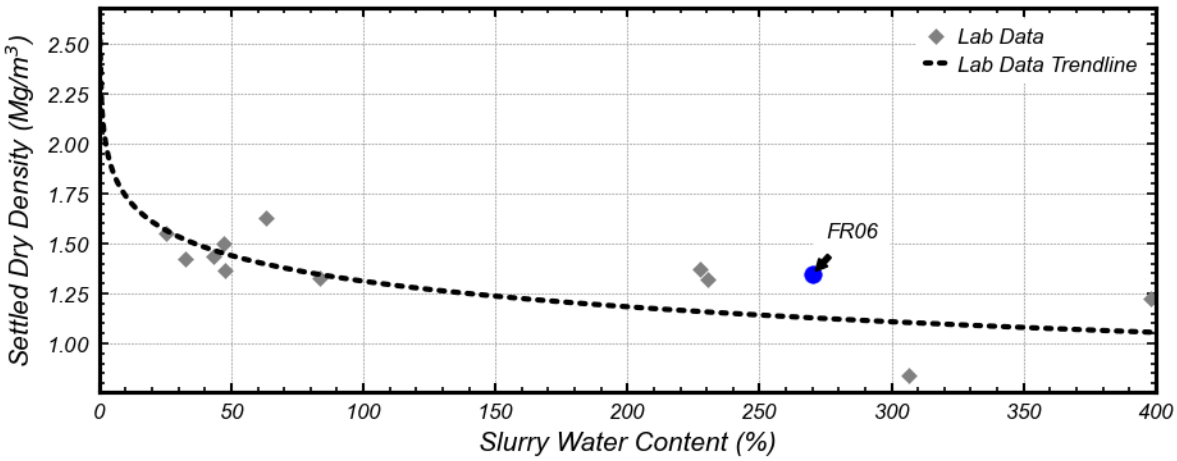

Figure 33. Settled dry density vs. slurry water content, with FR06.

3.3 Dewatering of the Deposit

After reaching an applied acceleration of 60 g during spinning, dewatering was performed in the deposit. Using the real time tensiometer data, the water table height was tracked during dewatering stages. The stages consisted of a set amount of time to open the dewatering port and allowing the deposit to return to hydrostatic equilibrium after closing of the port. This process was performed for about 90 minutes. The pore pressure behavior during dewatering is further discussed in section **3.6**. The final water table height in the deposit was determined to be 11.6 m (H_{WT}, prototype scale), which corresponds to a water table over impoundment height (H_{WT}/H_I) ratio of 0.59. Using the measured water table height, a hydrostatic pore pressure (u_0) distribution over the depth of the impoundment was developed. With the measured density of the deposit, total vertical stress (σ_v) was also determined. The vertical effective stress (σ'_v) for partially saturated soils was then typically be determined by the following relationship (Bishop and Blight 1963):

$$\boldsymbol{\sigma'_v = (\sigma_v - u_a) + \chi(u_a - u_w)} \qquad \textbf{(10)}$$

Where u_a is the air pore pressure, u_w is the water pore pressure, and χ is the effective stress parameter taken equal to the estimated degree of saturation. Based on the suctions measured in

FR06 and the SWRC presented in **Figure 12**, the smallest value saturation value, which is assumed to be equal to χ, is about 0.71 (at the surface of the ash). Assuming a χ of 1 (which reduces Equation 10 to Terzaghi's effective stress equation), the determined Q_{tn} and $Q_{tn,cs}$ profiles shown later have an underprediction of about 10% and 5% in the top 2 meters of the deposit, respectively. Due to the uncertainty in the SWRC at suctions greater than 20 kPa and the small effect on the stress normalized tip resistances, χ is assumed to be 1 at all depths for simplicity. The calculated stress distribution for FR06 after dewatering is shown in **Figure 34**.

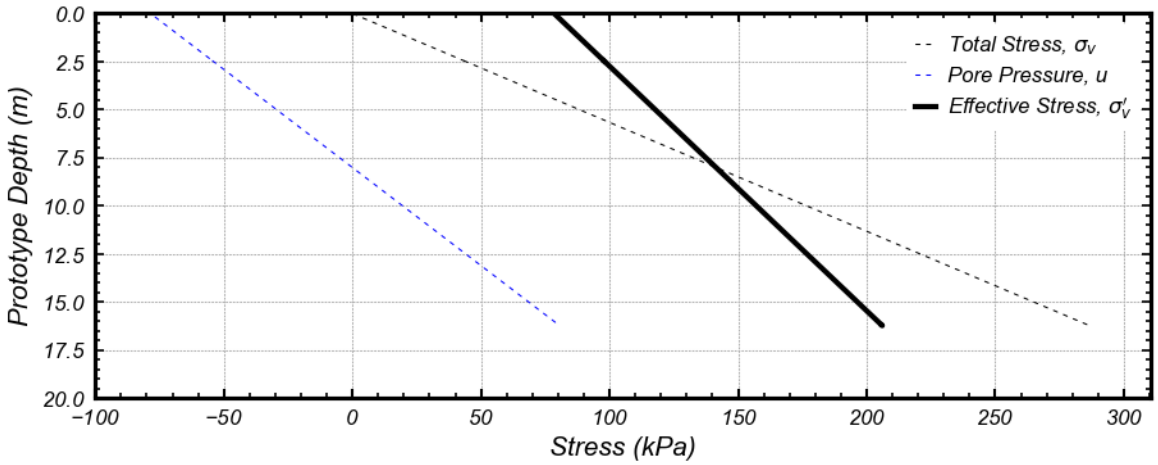

Figure 34. Stress profile with depth for FR06, after dewatering (χ is assumed as 1 at all depths).

3.4 Stiffness and Strength Prior to Gate Opening

Prior to opening of the gates, two CPT pushes and bender elements were used to characterize the strength and stiffness of the deposit. The CPT pushes were performed after dewatering, and the bender element readings were taken at each applied acceleration step (as well as before and after dewatering at 60 g). Due to issues in data collection, only the shallow bender pair was able to measure shear wave response, and only after dewatering at 60 g.

3.4.1 Bender Elements

Figure 35 shows the recorded response of the shallow bender element pair after dewatering. The shear wave velocity was determined to be 153.9 m/s. The small-strain shear modulus (G_{max}) is then determined by the following equation:

$$G_{max} = \rho_{total} V_s^2 \quad (11)$$

With a bulk density of 1.80 Mg/m^3 for FR06, G_{max} was 42.7 MPa at a depth of 3.42 m (prototype scale), after dewatering.

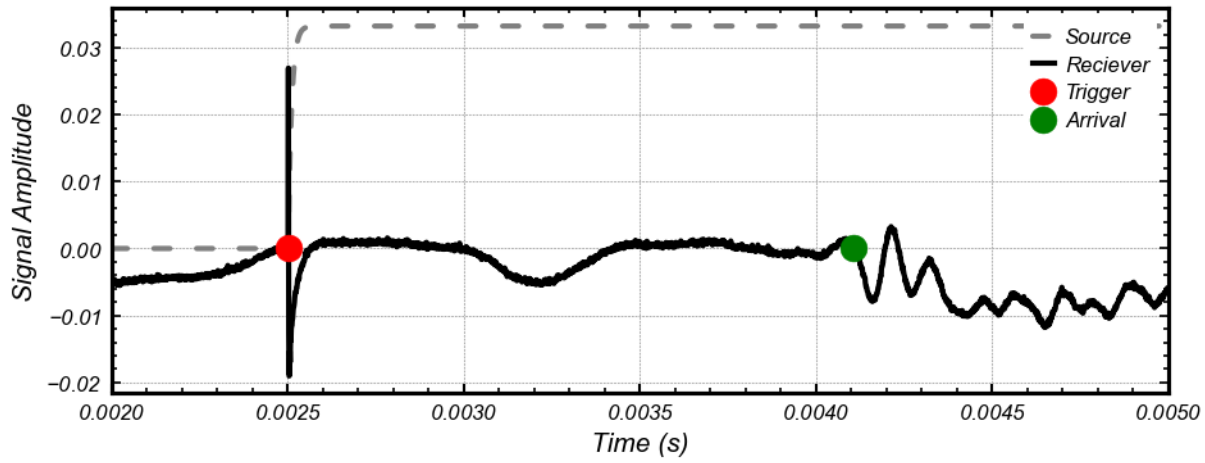

Figure 35. Determination of arrival time for shallow bender pair, after dewatering for FR06.

3.4.2 Cone Penetration Tests

An undrained (100 mm/s) and drained (2 mm/s) CPT push were performed in FR06 prior to opening of the gates, with q_c measured with depth. **Figure 36** presents the measurements. Based on critical state soil mechanics, when the undrained resistance is greater than the drained resistance, the material is assumed to be dilative. When the drained resistance is greater than the undrained resistance, the material is assumed to be contractive. Both pushes experienced resistances greater than 3 MPa at depths greater than 2 m (prototype scale). The drained push had

slightly greater resistance than the undrained push at depths less than 11.5 m. At greater depths, the drained resistance increases and the undrained resistance decreases. This suggests that the deposit has marginally greater drained strength than undrained strengths from the surface to 11.5 m, and a greater drained strength than undrained strength below 11.5 m, due to the generation of positive excess pore pressures during the undrained push. The undrained push may also have induced partially drained conditions rather than undrained above the water table, due to the partial saturation of the ash from dewatering. This would result in reduced magnitudes of excess pore pressures and dilatancy of the material, compared to when fully saturated, while the tendency to be dilative or contractive would remain the same. The increased difference between the drained and undrained resistance below 11.5 m indicates a more contractive material. It should be noted that displacement of the ash by the miniature CPT will also generate positive excess pore pressure in addition to that from shearing of the ash against the CPT shaft (termed an octahedral normal stress pore pressure component, from Burns and Mayne 1998), which would result in the undrained resistance being slightly smaller than the drained resistance for material that will exhibit zero shear-induced dilatancy.

Figure 36 also shows the correlated undrained shear strength (s_u) and the normalized cone tip resistance (Q_{tn}) with depth. s_u is determined by the following (Lunne et al. 1997):

$$\boldsymbol{s_u = \frac{q_c - \sigma_{v0}}{N_k}} \quad (\mathbf{12})$$

Where N_k is the cone factor, taken as 12 (from EPRI 2021). Q_{tn} was determined by the following:

$$\boldsymbol{Q_{tn} = \frac{q_c - \sigma_{v0}}{p_{atm}} \left(\frac{p_{atm}}{\sigma'_{v0}} \right)^n} \quad (\mathbf{13})$$

Where p_{atm} is atmospheric pressure. The exponent, n, was calculated using the relations defined in Robertson (1990). This value is limited to a maximum of 1.0 but was found to vary between 0.8

to 0.9. Since sleeve friction (f_s) is not obtained with the miniature cone penetrometer that was used, an assumption was made that the sleeve friction is 5% of the measured tip resistance to allow for calculation of the soil behavior index (I_c). This assumption is based on typical friction ratios for silt mixtures (clayey silt to silty clay) as specified in Robertson (1990) and has a negligible effect on calculated Q_{tn} values (see **Figure 37**). The following equations were used to calculate Q_{tn}:

$$\boldsymbol{F_r = \frac{f_s}{q_c - \sigma'_{v0}}} \quad (\mathbf{14})$$

$$\boldsymbol{Q_{t1} = \frac{q_c - \sigma_{v0}}{\sigma'_{v0}}} \quad (\mathbf{15})$$

$$\boldsymbol{I_c = [(3.47 - \log Q_{t1})^2 + (\log F_r + 1.22)^2]^{0.5}} \quad (\mathbf{16})$$

$$\boldsymbol{n = 0.381\, I_c + 0.05\left(\frac{\sigma'_{v0}}{p_{atm}}\right) - 0.15} \quad (\mathbf{17})$$

F_r is the normalized sleeve resistance and Q_{t1} is the stress normalized tip resistance. Q_{tn} was only analyzed for the undrained push.

Based on Robertson (2010), a correction factor (K_c) for normalized cone tip resistance in silty sands was used in EPRI (2021), to calculate an equivalent clean sand value ($Q_{tn,cs}$), using the following:

$$\boldsymbol{Q_{tn,cs} = K_c Q_{tn}} \quad (\mathbf{18})$$

Where K_c is a function of fines content, mineralogy, and plasticity, estimated using I_c with:

$$\boldsymbol{K_c = 1.0 \; if \; I_c \leq 1.64} \quad (\mathbf{19})$$

$$\boldsymbol{K_c = 5.581\, I_c^3 - 0.403\, I_c^4 - 21.63\, I_c^2 + 33.75\, I_c - 17.88 \; if \; I_c > 1.64} \quad (\mathbf{20})$$

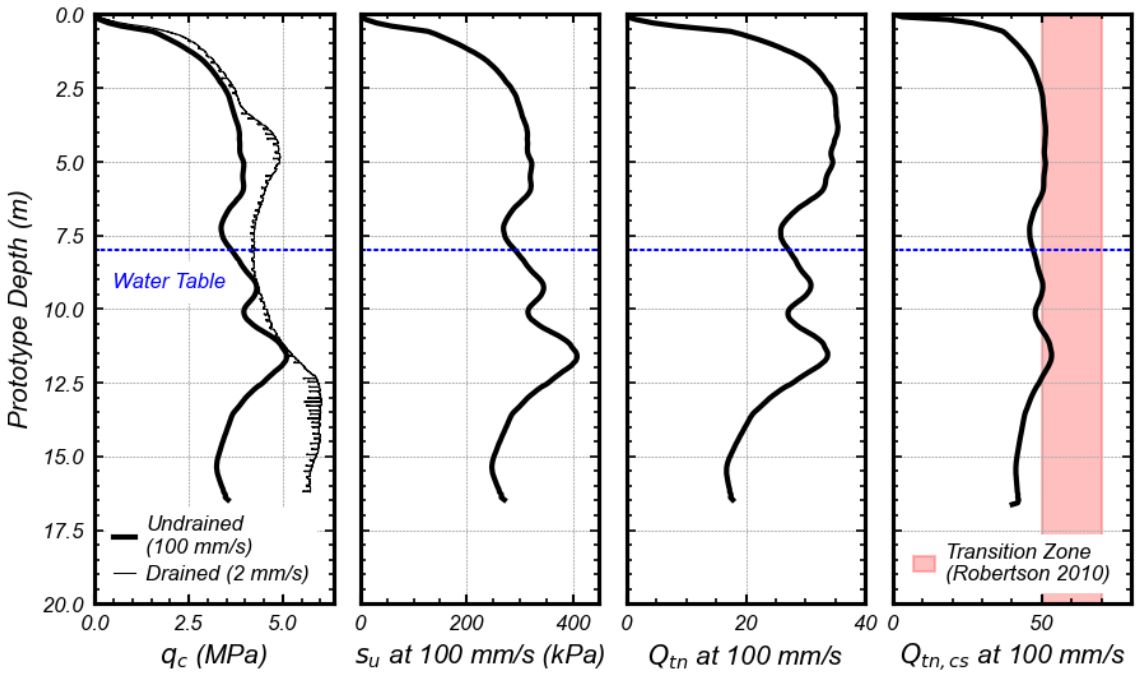

Figure 36. Measured q_c, and correlated s_u, Q_{tn}, and $Q_{tn,cs}$ for FR06.

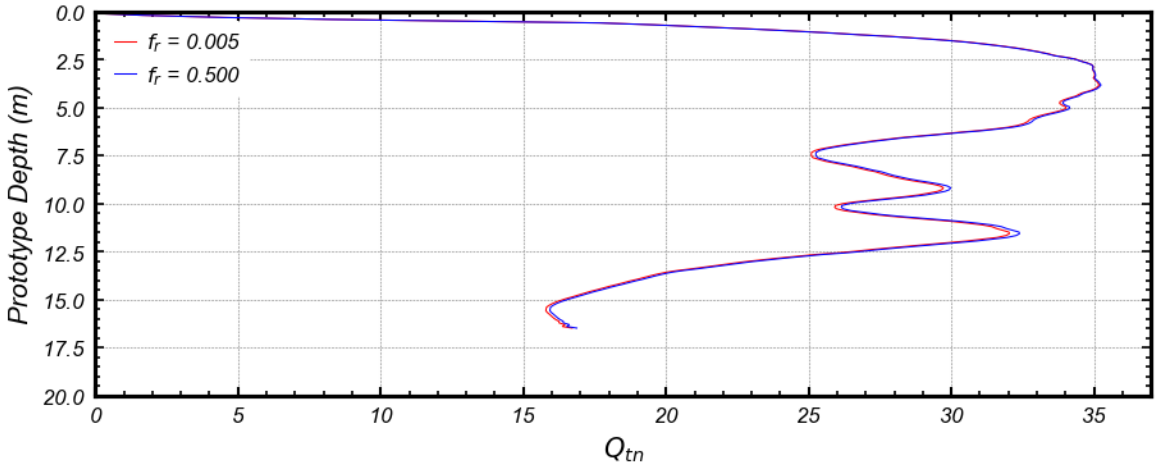

Figure 37. Effect of sleeve friction ratio, $f_r = f_s / q_c$, on Q_{tn}.

Robertson stated that a $Q_{tn,cs}$ value between 50 to 70 is the likely boundary between a contractive and dilative soil state, and is similar in form to the state parameter (ψ) in critical state soil mechanics. It should be noted that none of the case studies used to guide the recommendations in

Robertson (2010) are from fly ash impoundments, so the criteria provided by Robertson may not be applicable to ponded fly ash. FR06 generally has a $Q_{tn,cs}$ value close to 50 for the top 12.5 m and below 50 for the remainder of the push, suggesting that the ash deposit should exhibit more contractive behavior below 12.5 m than it would at shallower depths.

3.5 Runout Behavior

Using the GoPro HERO3 cameras, runout distance and general failure mechanisms were recorded during FR06. Upon opening of the gates, a slope instability mechanism became apparent on the exposed face of the deposit. **Figure 38** shows the deposit after the initial failure. The material that fell in front of the deposit appeared to have many clumps and visually has a dry texture. **Figure 39** shows the runout distance of the initial failure. About 7 minutes (model scale) after opening the gates, a second slide occurred, which appeared to cause more saturated ash to displace away from the deposit. **Figure 40** shows the smooth surface at the bottom of the slide, suggesting that this secondary failure was driven by ash with a higher water content than the initial slide. **Figure 41** shows a possible schematic of how the failure sequence could have occurred. Small streams of water were observed to exhibit the failure mass after the secondary failure, shown by the dried ash lines propagating from the bottom of the failure mass in **Figure 40**. **Figure 42** shows the change in runout distance experienced during the second slope failure, which resulted in a sudden increase of runout distance of 7 m over a period of 1 second.

Figure 38. Initial slope instability failure during FR06.

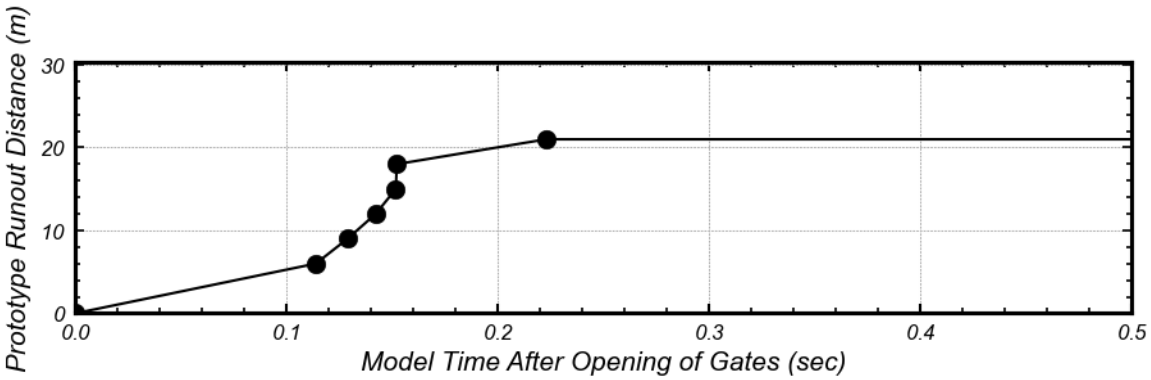

Figure 39. Runout distance of initial failure during FR06.

The final runout distance (R_L) of the deposit after opening the gates was 28.8 m in prototype scale, which was reached during the second slide at a prototype time of less than 7 hours (415 minutes). The model was held at an acceleration of 60 g for approximately 29 minutes (model time). The final runout distance over impoundment height ratio (R_L/H_I) for FR06 was 1.47. **Figure 40** and **Figure 43** show the deposit after the completion of spinning. **Figure 44** shows a closeup of the crest of the slide, with the displaced hole at the top of the deposit being from the final CPT push (drained), which could have influenced the location of the slide's crest. Due to a malfunction

in the software used to record the depth camera footage, quality surface profiles of the ash were not obtained during testing.

Figure 40. FR06 after completion of spinning.

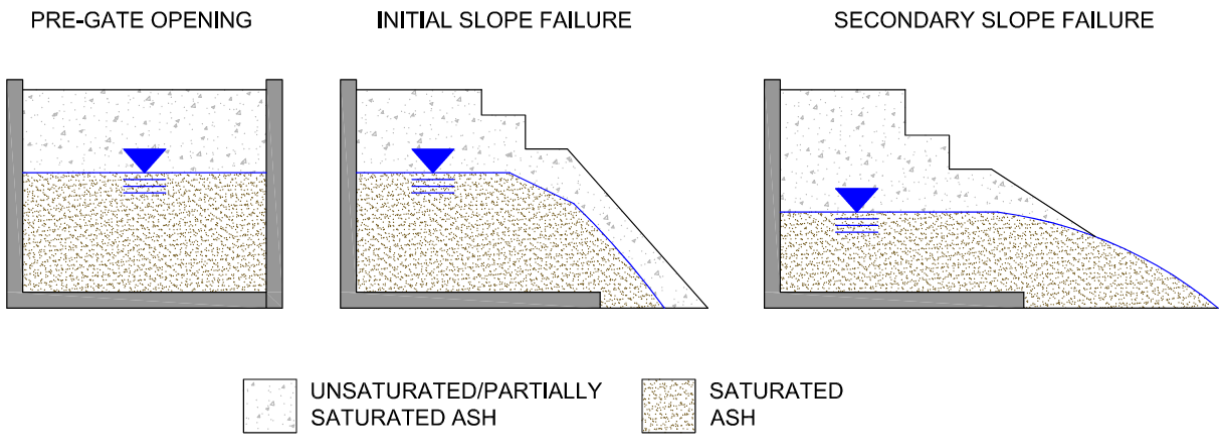

Figure 41. Possible schematic of observed slope failures during FR06, showing the initial failure of drier ash, followed by a secondary failure of wetter ash through the original failure mass (not to scale).

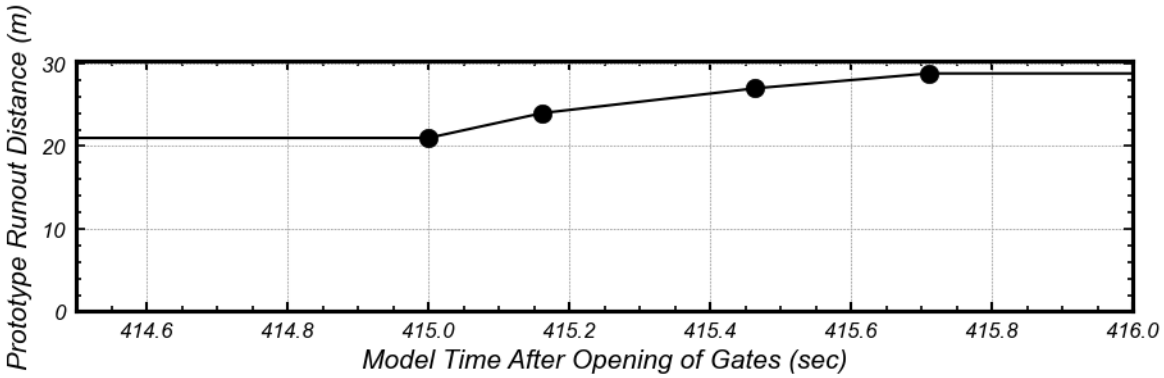

Figure 42. Runout distance of second failure during FR06.

Figure 43. View from top of container for FR06 after spinning.

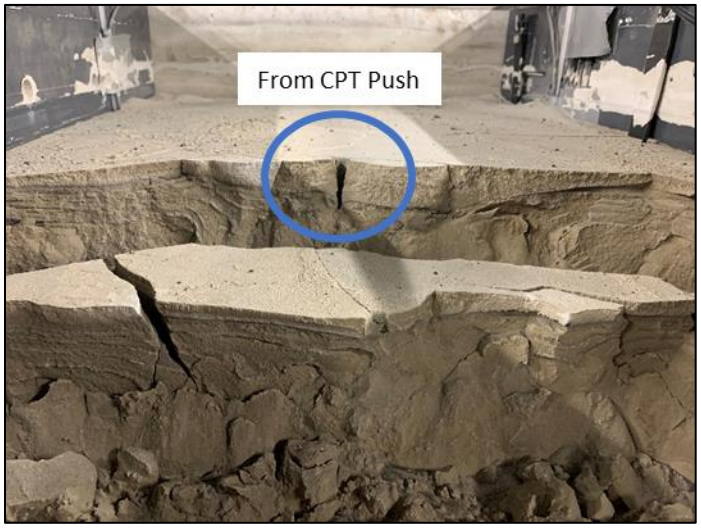

Figure 44. Start of slide of FR06, with middle hole at the surface resulting from a CPT push.

3.6 Pore Pressure Results

As noted in in EPRI (2021), not all 20 tensiometers placed in the model worked during centrifuge testing. This could possibly be due to electrical issues, non-watertight epoxy seals, or desaturation of pore stones during specimen preparation. For FR06, 14 of the 20 tensiometers placed in the model produced quality data. **Figure 45** shows a schematic indicating the locations of the working tensiometers.

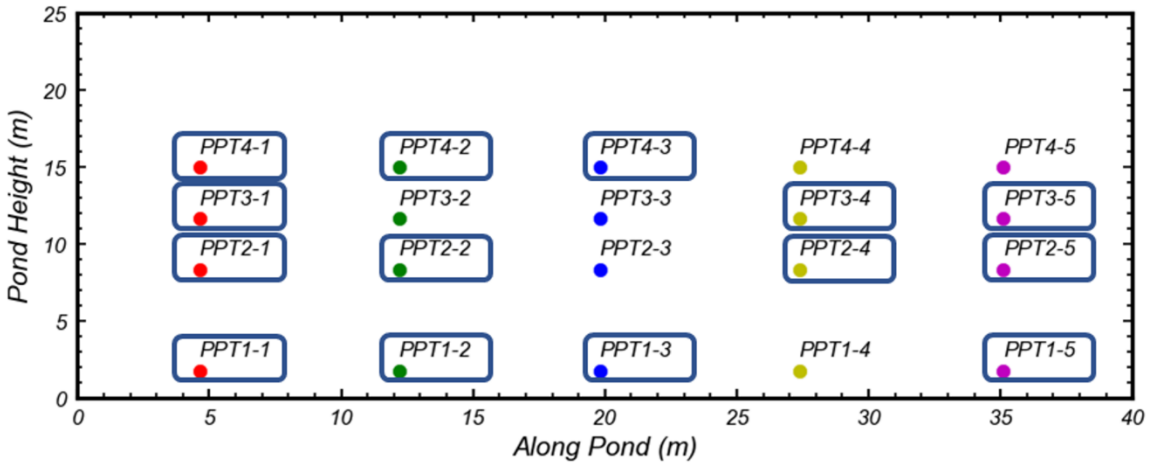

Figure 45. Tensiometers included in model FR06, with sensors that produced quality data indicated in blue boxes.

Readings were taken from the tensiometers at a frequency of 1 Hz through the duration of spinning, with the data presented in **Figure 46**. Excess pore pressures were developed as the g-level applied to the model was increased to 20 g, most likely because the increased acceleration loaded the model at a rate faster than the rate of pore pressure dissipation. In PPT row 1 (see **Figure 45**) for example, about 20 to 30 kPa of excess pore pressure was developed, whereas the calculated vertical effective stress at this level would be about 47 kPa at hydrostatic equilibrium. After reaching an acceleration of 60 g, the pore pressure continued to decrease slightly before dewatering, possibly due to a small amount of consolidation occurring in the deposit. Dewatering

occurs from 1.3 to 2.8 hours (model time) in nine stages. The dewatering port was left open on average for 6 minutes (model time) for the first eight stages, and about 22 minutes for the final stage. PPT row 1 shows how the transient pore pressures decrease more at the back of the container while the dewatering port is open, but the entire row returns to the same pressure when hydrostatic equilibrium is reached after closing of the dewatering port. A similar trend can be observed in PPT rows 3 and 4. PPT rows 3 and 4 recorded negative pore pressure values during dewatering, indicating suction was developed above the water table. After dewatering, the average pore pressure in PPT row 4 is about -32 kPa and -2 kPa in PPT row 3. A pore pressure spike is also observed at about 2.9 hours (model time) in all four PPT rows, which is the same time that the undrained (fast) CPT push was performed, indicating that positive excess pore pressures were developed during penetration. PPT2-1 appears to have a slight drift in readings starting at 1.6 hours but appears to measure changes in pore pressures to an accurate enough degree. PPT4-2 also shows a slight deviation from the rest of PPT row 4 during dewatering, but then suddenly decreases back to the suction level of the other two tensiometers, possibly due to desaturation of the ceramic stone. From the data shown here, it is clear that all pore pressures decrease after opening of the gates.

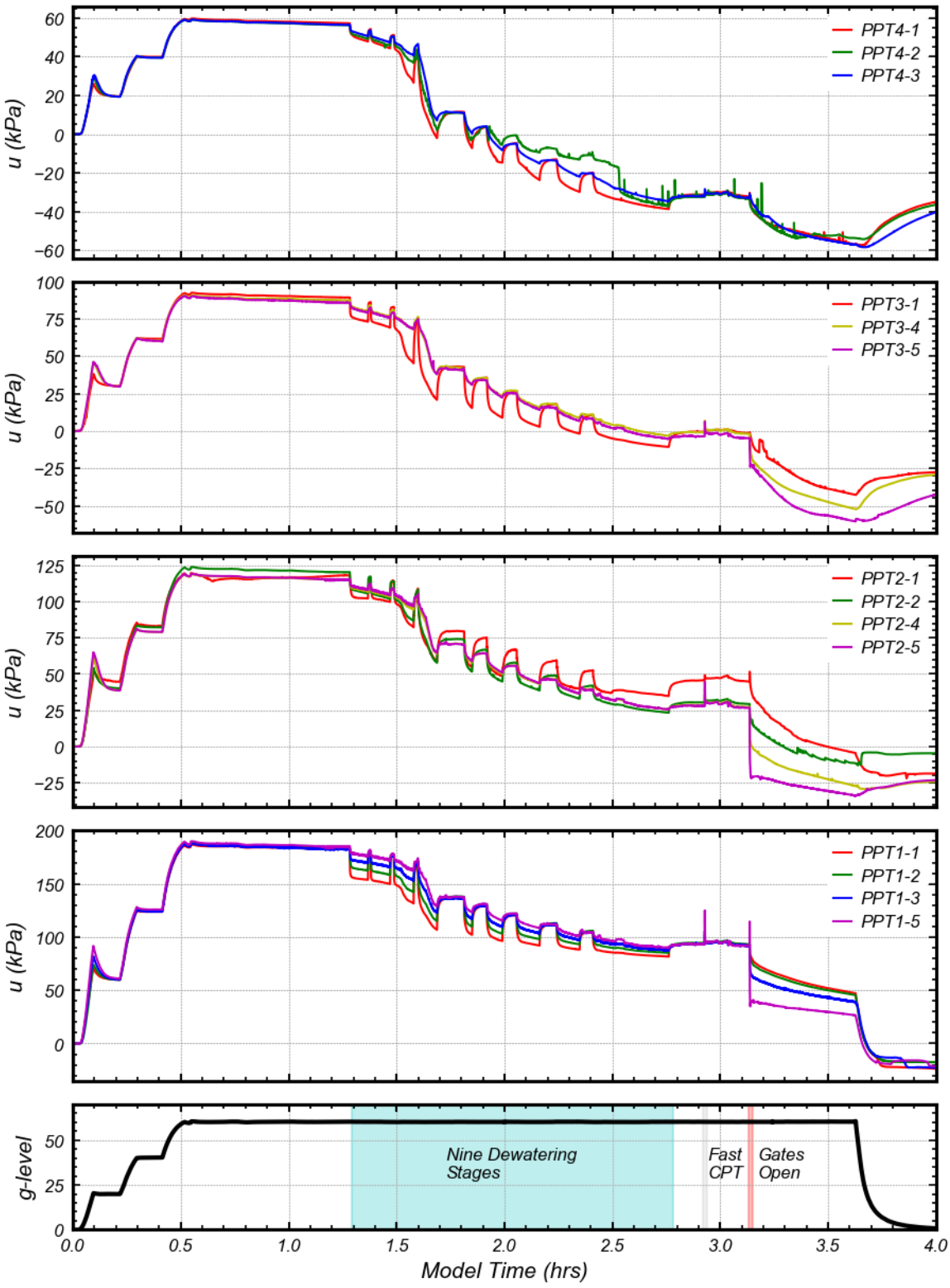

Figure 46. Pore pressure response during FR06.

Upon opening of the gates, excess pore pressure (Δu) is developed through two mechanisms: a decrease in mean total stress (Δp) and shear-induced dilatancy. It is assumed that there is no seepage immediately after opening the gates. To properly assess the shear-induced excess pore pressures, the decrease in mean total stress was estimated assuming the ash is a fully saturated (including above the water table), isotropic elastic soil. This decrease in mean total stress then results in an equal excess pore pressure:

$$\boldsymbol{\Delta u = \Delta p = \frac{\Delta \sigma_x + \Delta \sigma_y + \Delta \sigma_z}{3}} \quad (\mathbf{21})$$

σ_x is the stress perpendicular to the container side walls, σ_y is the stress perpendicular to the gates, σ_z is the stress in the vertical orientation, and Δ denotes the change of the noted stress. The initial state of stress at an element level is shown in **Figure 47**. Initial horizontal stress (σ_{h0}, which is equal to the initial σ_x and σ_y values) can be written in terms of vertical effective stress with the following:

$$\boldsymbol{\sigma_{h0} = K_0 \sigma'_{v0} + u_0} \quad (\mathbf{22})$$

Where K_0 is the at rest coefficient of lateral earth pressure, σ'_{v0} is the initial vertical effective stress, and u_0 is the initial pore pressure.

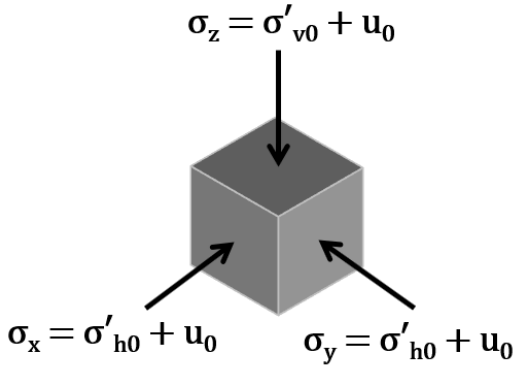

Figure 47. Initial state of stress to calculate excess pore pressure from a change in mean total stress.

Assuming the gates open very rapidly, $\Delta\sigma_y$ is taken as the negative of the initial horizontal stress, and $\Delta\sigma_z$ is zero. Assuming plane strain conditions allows for the calculation of $\Delta\sigma_x$ using the following:

$$\boldsymbol{\Delta\sigma_x = \nu_u(\Delta\sigma_y + \Delta\sigma_z)} \quad (\mathbf{23})$$

Where ν_u is the undrained Poissons ratio, taken as 0.5. The resultant $\Delta\sigma_x$ value is then one half of $\Delta\sigma_y$. Using Equations 21 through 23, the resulting excess pore pressure from the reduction in mean total stress can then be written as:

$$\boldsymbol{\Delta u = \Delta p = -\frac{1}{2}(K_0\sigma'_{v0} + u_0)} \quad (\mathbf{24})$$

K_0 was assumed to be 0.5. Despite the simplifications necessary to calculate the value, the excess pore pressure from a change in mean total stress provides an approximate benchmark to properly assess the shear-induced dilatancy from the pore pressure response during the opening of the gates.

For the first few minutes of the runout test, the tensiometers were run with a sampling frequency of 5000 Hz. **Figure 48** shows the excess pore pressures measured by the tensiometers immediately after opening of the gates, which occurs at about 0.15 seconds on the plots. The estimated excess pore pressures developed from the change in mean total stress are also shown (denoted by 'Estimated Δp', based on equation 24), with excess pore pressures below this likely indicating dilative behavior, and above likely indicating contractive behavior. At 0.2 to 0.3 seconds, PPT4-1 shows a positive spike in pore pressure of about 14 kPa, while PPT4-2 and 4-3 show negative pore pressure spikes of 8 and 20 kPa, respectively. At the same time, PPT3-1 remains relatively constant, while PPT3-4 and 3-5 exhibit negative pore pressure spikes of 32 and 20 kPa, respectively. PPT2-1 and 2-2 remain relatively constant during this time, while PPT 2-4 and 2-5 show negative pore pressure spikes of 25 and 45 kPa, respectively. Immediately after gate

opening, PPT1-1 and 1-2 exhibit a negative pore pressure spike of about 10 kPa, while PPT1-3 and 1-5 show positive pore pressure spikes of 15 and 55 kPa, respectively. PPT4-3, 3-5, and 2-5 all show a positive spike in pore pressure at about 0.7 seconds on the plot, which coincides with the large positive pore pressure spike in PPT1-5 quickly reducing. This may be caused by the dissipation of excess pore pressure from the front of the bottom of the container (PPT1-3 and 1-5) towards the front half of the surface of the deposit, as demonstrated by the positive spike in PPT4-3 being about 0.1 seconds after that of PPT3-5 and 2-5.

Based on the estimated excess pore pressure from the change in mean total stress, the only sensor to display shear-induced dilative behavior is PPT4-3. PPT1-5 displays shear-induced contractive behavior, with a positive measured excess pore pressure. PPT2-5 and 3-4 show marginally contractive behavior. Comparing the largest magnitude of measured excess pore pressures from each PPT row (PPT1-5, 2-5, 3-4, and 4-3) with the estimated excess pore pressures from the change in mean total stress, the shear-induced pore pressure response becomes more positive with depth, with significant contractive behavior in PPT row 1 (at a prototype depth of 17.8 m). A significant change in shear-induced behavior in the bottom of the deposit aligns with the divergence of the undrained and drained tip resistances (shown in **Figure 36**). Simplifications in calculating the excess pore pressure from the change in mean total stress (such as full saturation above the water table) could lead to error in assessing the shear-induced dilative tendencies, but the difference in the behavior in PPT row 1 (contractive) and PPT rows 2, 3, and 4 (marginally contractive to dilative shear-induced behavior) is apparent. Partial drainage effects may also lead to reduced excess pore pressures (from changes in mean total stress and shear-induced dilatancy) in PPT row 4 (prototype depth of 4.6 m). Differences in excess pore pressures within each PPT row are most likely due to differences in applied strain from opening of the gates, especially in

PPT4-1, which measured a positive excess pore pressure despite the observed shear-induced dilative behavior at PPT4-3.

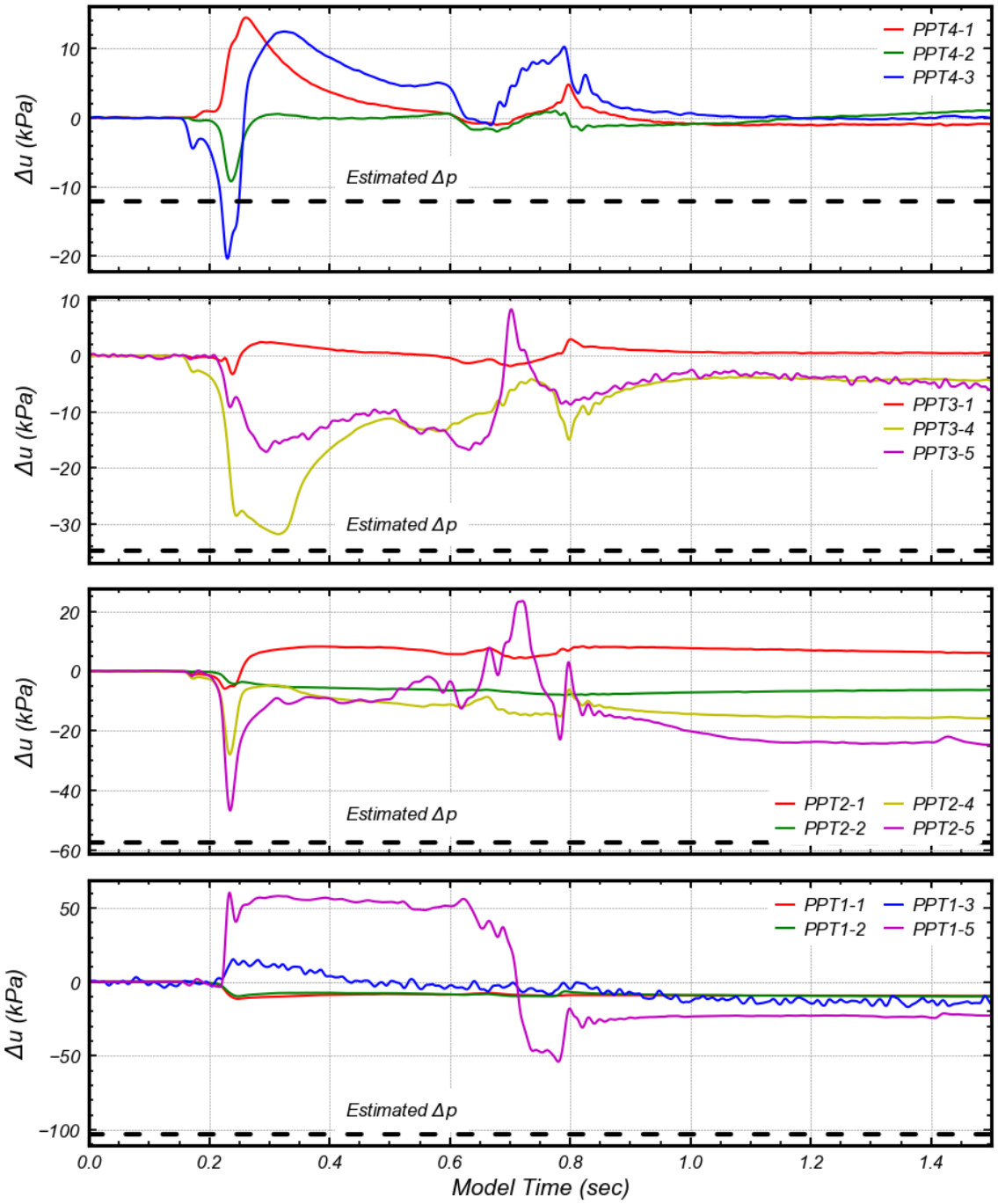

Figure 48. Pore pressure response immediately after opening of gates during FR06.

Lateral hydraulic gradients (*i*) at different time intervals were also calculated, based on the measured pore pressures using the following equation:

$$\boldsymbol{i = \frac{\Delta h_{t,i}}{\Delta l_i} = \frac{\left(\frac{u_x - u_{x+1}}{\gamma_w}\right)}{\Delta l_i}} \qquad (25)$$

Where $\Delta h_{t,i}$ is the total head difference between any two adjacent pore pressure sensors located at the same elevation, Δl_i is the horizontal distance between such pore pressure sensors, u_x and u_{x+1} are the pore pressures measured by both sensors, with the sensor measuring u_{x+1} being closer to the gates than the sensor measuring u_x. The calculated hydraulic gradients are shown in **Figure 49,** where negative gradients indicate flow towards the gates**.** At the opening of the gates, gradients at the bottom of the front and middle of the deposit are positive, indicating flow into the deposit, possibly from the generation of positive excess pore pressures or from exposure of the tensiometers to air during the initial slope failure. The shallower portions of the front and middle of the deposit show lower magnitude gradients at the opening of the gates, possibly due to the lowered water table (at 11.6 m pond height, prototype scale). The back of the deposit shows a negative gradient at a height of 8 m at the opening of the gates, which decreases with time, indicating a reduced flow from the back of the deposit after opening of the gates. The middle of the deposit then shows an increase at a time of 1.00 minutes in negative gradients below the water table, which then decreases after. Gradients at the bottom of the front of the deposit become negative at a time of 1.00 minutes and remain constant for the remainder of the test, while negative gradients above the water table slightly increase throughout the remainder of the test. The general flow of water inferred from the calculated hydraulic gradients matches the observed runout behavior, in which a secondary slope failure of wetter ash occurred at a model time of about 7 minutes, with continued flow of water out of the deposit onto the runout board for the remainder of the test.

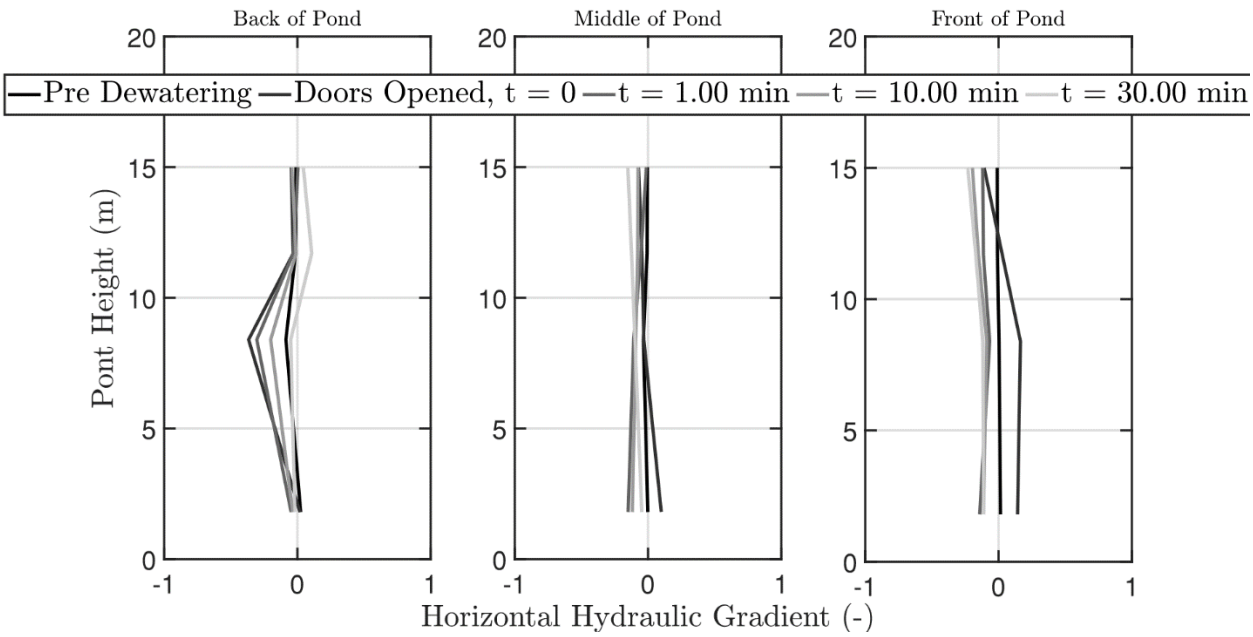

Figure 49. Lateral hydraulic gradients during FR06 (negative gradients indicate flow from back of container towards gates).

3.7 Water Content Results

The moisture probes were run at a sampling frequency of 0.01 Hz during specimen preparation. **Figure 50** shows the measured dielectric permittivity and conductivity during the deposition process. The sudden drops in the readings at 20, 46, 69, 75, 87, and 116 hours are due to siphoning of pooled water after completion of each lift. Dielectric permittivity tended to vary with time after each lift, whereas conductivity would only change during siphoning of pooled water. **Figure 51** shows the water contents calculated from the conductivity readings. The sudden drops in water content are also from siphoning of pooled water. Conductivity readings of around 5000 µS/cm are readings of the pooled water that has yet to be siphoned. It is noted that the probes were not calibrated in pure water, thus the calibration curves shown in **Figure 26** should not be used to estimate water content from conductivity readings obtained from pooled water. The water contents estimated from the conductivity readings indicate that the water contents stabilize

between 16 and 19%, suggesting little spatial variability. However, the water content values are inconsistent with the mass-calculated water content of the deposit of 34%. For this reason, the moisture probes were only relied on to provide relative changes in water content during FR06.

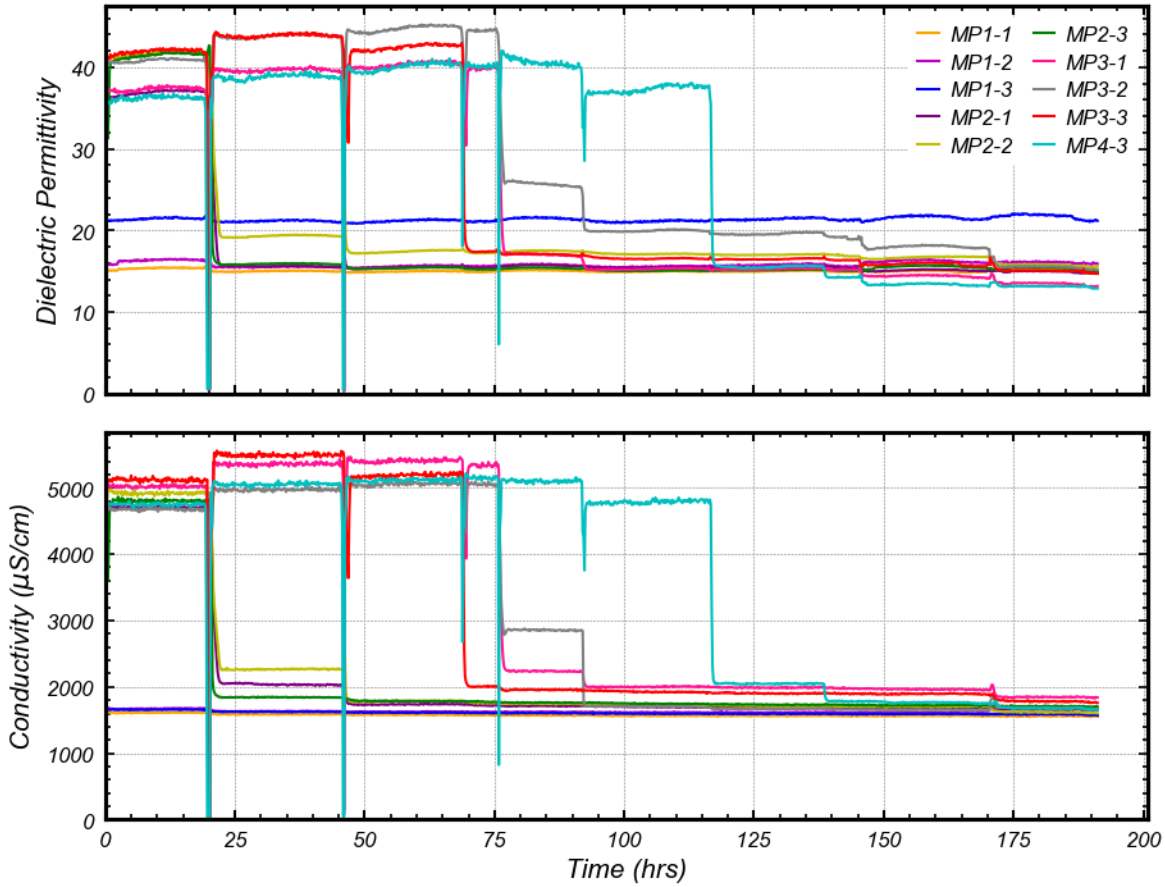

Figure 50. Dielectric permittivity and conductivity during specimen preparation for FR06.

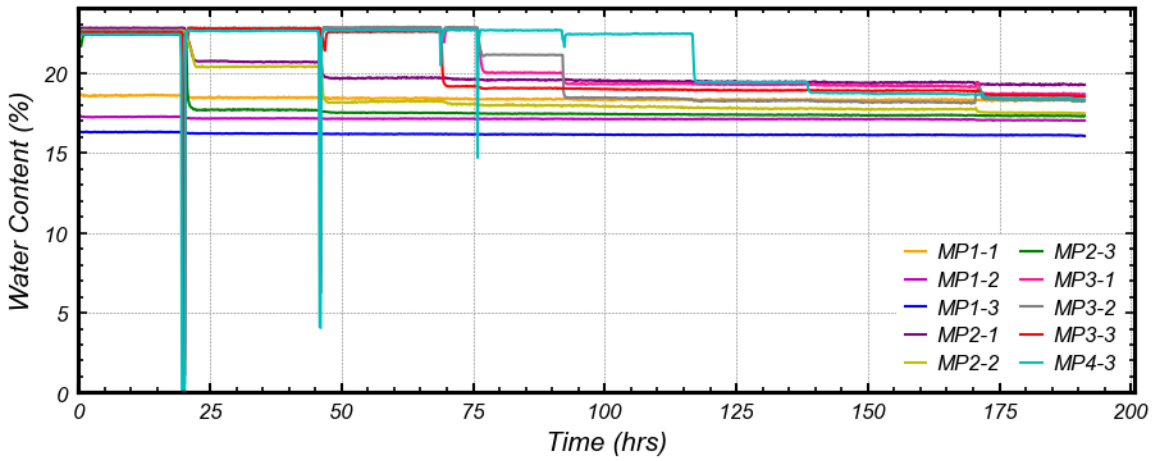

Figure 51. Correlated water content during specimen preparation for FR06.

During spinning, the moisture probes were run at a sampling frequency of 0.1 Hz. **Figure 52** shows the dielectric permittivity and conductivity readings during spinning. The dielectric permittivity readings trend upward prior to opening of the gates, except for MPs 3-1, 3-2, and 4-3, which are the shallowest sensors. These three sensors also show a significant decrease in permittivity during dewatering (which begins at 1.3 hours). As previously stated, it is hypothesized that there are unknown factors that influence the dielectric permittivity readings, such as density of the ash, thus making them less reliable than the conductivity data for determining water content. Differences in boundary effects between the plastic container used for calibration and the large metallic container the test was performed in could also contribute to the discrepancies. The conductivity measurements tend to decrease with time until 1.5 hours. The same three sensors located at the shallowest locations that showed decreases in permittivity from dewatering also showed decreases in conductivity. At the opening of the gates, MP3-3 and 4-3 show drastic decreases in the measurements, due to exiting of the ash surrounding the sensors from the container. MP3-2 also shows a significant decrease upon opening of the gates, likely caused by a tension crack that developed in the ash during the initial slope failure (see **Figure 43**).

Figure 53 shows the inferred water contents and water content changes during the test. The water contents spike upwards by about 0.1 to 0.3% between 0.1 and 0.2 hours, and then quickly decrease to the same or lower water contents, depending on the sensor. As discussed in the analysis of the pore pressure data in section **3.6**, this could be due to a buildup of excess pore pressure from increasing the g-level, with consolidation subsequently occurring. The water contents then slightly decrease until about 1.5 hours. The shallowest sensors, MP3-1, 3-2, and 4-3, all show reductions in water content due to dewatering, with MP3-1 and 3-2 decreasing by about 2.5%, and MP4-3 decreasing by about 10%, indicating that water content of the ash decreased the farther it was above the water table. MP1-1, which is the closest sensor to the dewatering port at the bottom of the back wall of the specimen, shows an increase in water content throughout dewatering, which could be due to the flow of water towards the dewatering port. The other two moisture probes in the deepest row show a similar trend of an increase in water content throughout dewatering. At the opening of the gates, MP3-3 and 4-3 were exposed during the slope failures of the deposit, which is why the measured water contents of these sensors are near-zero. A sudden decrease is also shown in MP3-2, likely due to the tension crack formed in the ash. MP3-1 and 3-2 show a steady decrease in water content after opening of the gates, indicating flow of water away from the back of the container above the water table.

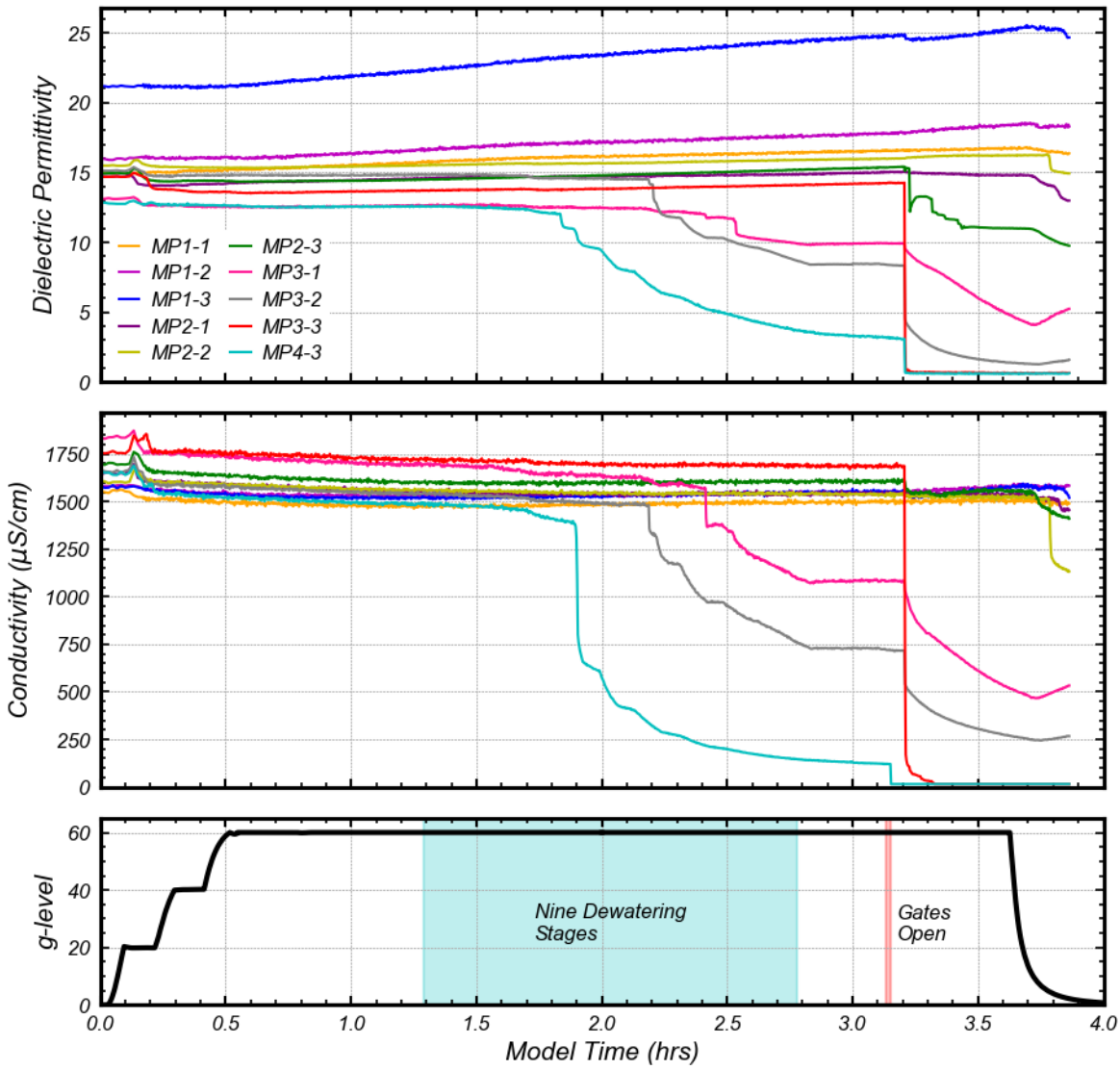

Figure 52. Dielectric permittivity and conductivity during spinning for FR06.

Figure 54 plots the measured dielectric permittivity in specimen preparation and spinning of FR06 against the corresponding conductivity values, which is compared to the trendline obtained from the laboratory calibrations. The data shows that the permittivity and conductivity exhibited a more linear relationship than what was found from the laboratory data, with permittivity not increasing as much with increasing conductivity as what was previously found. Density appears to influence dielectric permittivity readings, as shown by the increasing values

over time, during which slight consolidation of the ash occurred. And as previously discussed, differences in boundary effects could also contribute to this discrepancy.

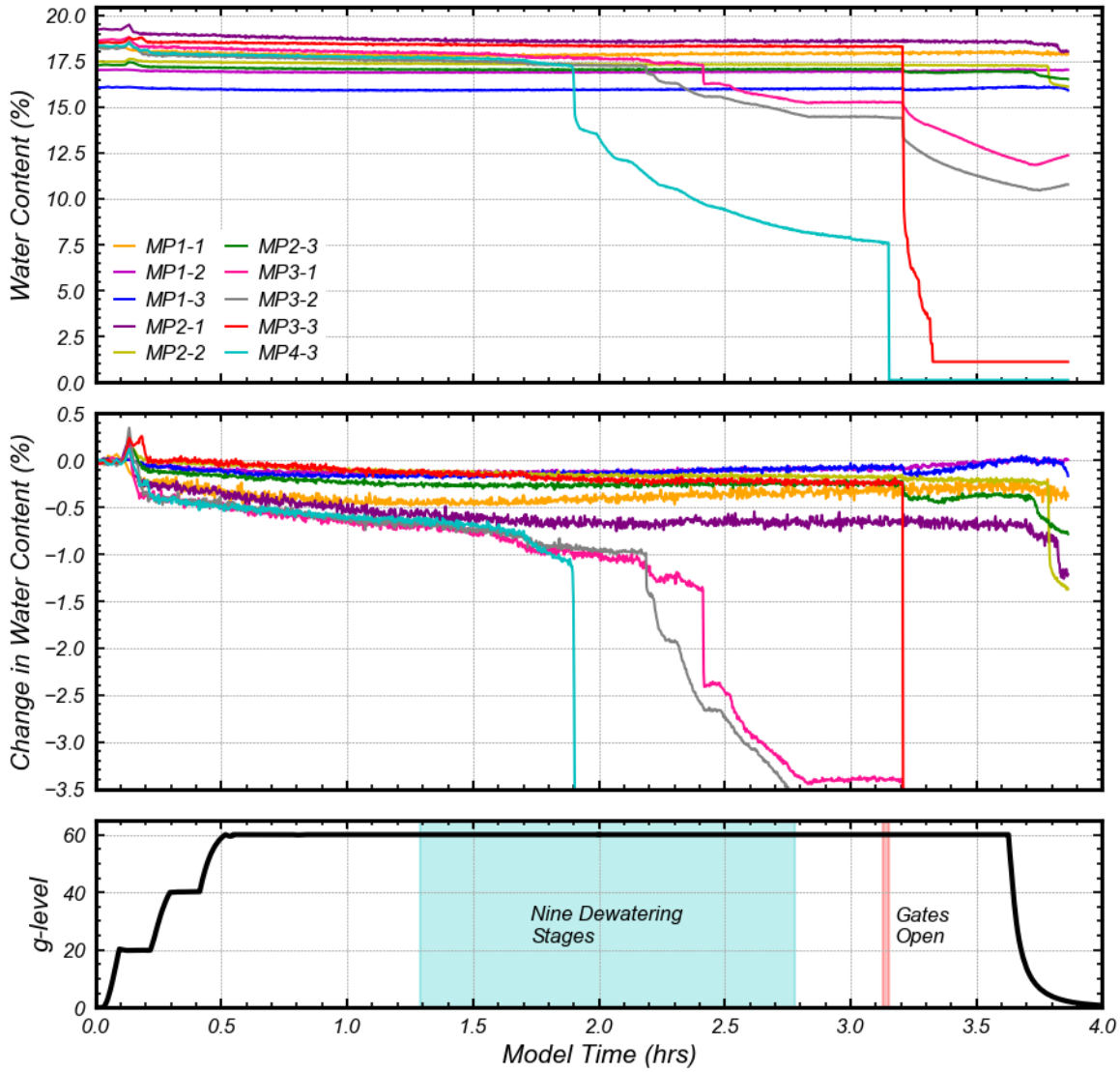

Figure 53. Correlated water content and change in water content during spinning for FR06.

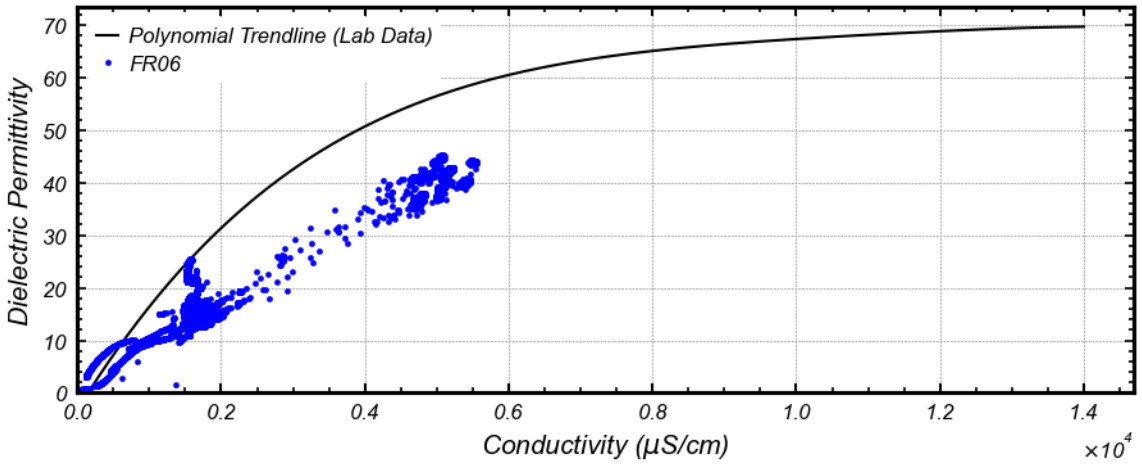

Figure 54. Dielectric permittivity plotted against conductivity for FR06.

Combining the data from the moisture probes and the tensiometers allows generation of SWRCs as a function of conductivity or change in water content, as shown in **Figure 55** and **Figure 56**, with the predicted SWRC curve from **Figure 12** included in **Figure 56**. Conductivity and change in water content data from MP3-1, 3-2, and 4-3 was used to generate the plots, as these were the only moisture probes that experienced significant reductions in conductivity and measured water content during dewatering. The suction values at the corresponding elevations were determined based on the water table elevation during dewatering at times of hydrostatic equilibrium (inferred from **Figure 46**). **Figure 56** shows a difference in the turning point of the SWRC from the lab data and the moisture probe data of about 20 to 30 kPa. This suggests that the air-entry value inferred from the moisture probes is higher than what was determined from the lab data, but this could also be due to issues in the calibrations of the moisture probes that have been previously discussed or uncertainty in the lab-measured SWRC. The lab data SWRC and the data from MP4-3 show agreement at changes in water content greater than 2%.

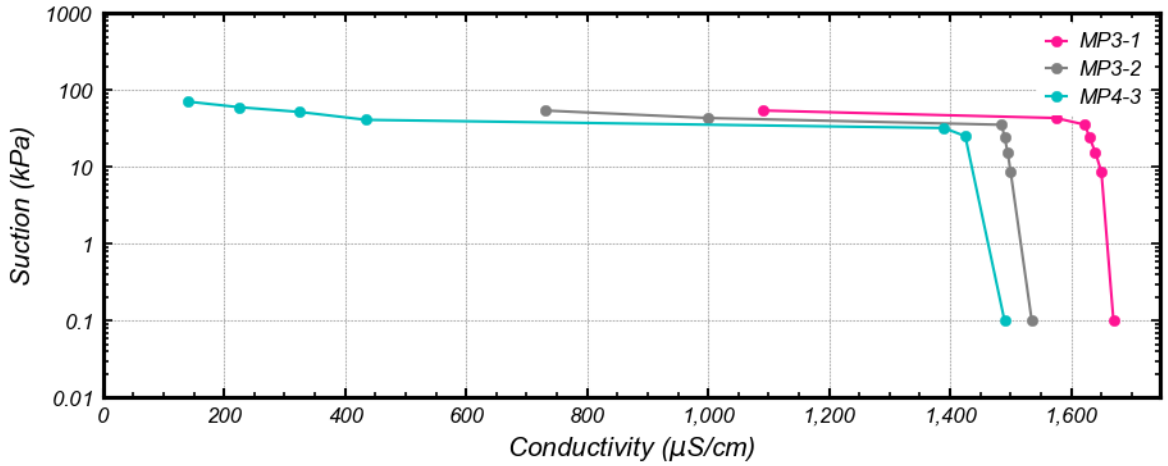

Figure 55. SWRC based on conductivity for FR06.

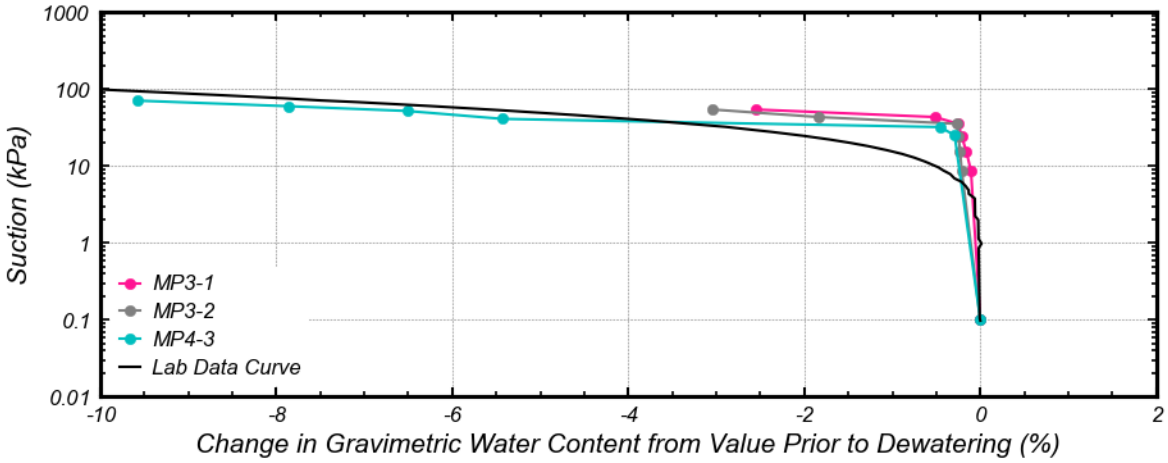

Figure 56. SWRC based on change in water content from value prior to dewatering for FR06.

3.8 Comparison to Previous Centrifuge Tests

The following sections compare the results of FR06 to the 9-m centrifuge tests previously performed in EPRI (2021) on the same ash: FR01, FR02, FR03, and FR05. The measured properties of the deposits and observed failure modes are presented in **Table 2**. FR01, FR02, and FR03 were all performed with a denser specimen than FR06 was, with the H_{WT}/H_I ratio increasing with each test, up to 1.10 for FR03. A leak in the gates occurred during FR01, which resulted in a

water table that sloped downwards towards the gates. Test FR02 was performed with the water table just below the ash surface (H_{WT}/H_I = 0.96), while Test FR03 was performed with water pooled over the ash impoundment (H_{WT}/H_I = 1.10). Tests FR01, FR02, FR03 exhibited slope instability failure mechanisms after opening of the gates. FR05 was performed on a looser specimen than FR06 and exhibited a sudden flow failure upon opening of the gates. As shown in later discussions, FR05 had significantly less strength and stiffness than the four other tests. **Figure 57** and **Figure 58** show that tests FR02, FR03, and FR05 fit into the general settled dry density trends discussed in section **2.3** (slurry water content was not measured in FR01). **Figure 59** shows the calculated effective stress profiles for all centrifuge tests after dewatering and prior to gate opening (with χ assumed as 1 for all tests). A low and high bound estimate were plotted for FR01, using the highest and lowest measured water table heights after dewatering, respectively. From dewatering, FR01 and FR06 have the largest effective stresses of the centrifuge tests as a result of the lower water tables.

Figure 60 plots calculated void ratios from the centrifuge tests versus mean effective stress, along with the two possible CSL's and ICU-TXC data previously referenced. Void ratio was calculated based on the specific gravity of the ash and the calculated dry density. Mean effective stress was calculated using the following equation:

$$\boldsymbol{p' = \frac{\sigma'_v + 2\sigma'_h}{3} = \frac{\sigma'_v + 2K_0\sigma'_v}{3}} \qquad (\mathbf{26})$$

K_0 was assumed to be 0.5. Vertical effective stress was taken from **Figure 59**, with depths of one-quarter, one-half, and three-quarters of the depth of the impoundment analyzed. The vertical effective stress of FR01 was taken as an average of the low and high bound estimates at the corresponding depths. The void ratios for the centrifuge tests were calculated using the average measured densities of the models, so effects of spatial variability are not accounted for. It should

be noted that FR06 could have significant variability of void ratio above and below a prototype depth of 11.5 m, based on the divergence of the undrained and drained tip resistances in **Figure 36**. Consistent with the measured average densities, FR01, FR02, and FR03 plot well below the possible CSL's, while FR05 plots above them. FR06 plots below the possible CSL's, but closer than FR01, FR02, and FR03. This correlates well with the CPT and pore pressure results later discussed. The initial states also agree with the observed failure modes and runout lengths listed in **Table 2**.

Table 2. Measured properties and observed failure modes of the five centrifuge tests.

Test	60 g ρ_{total} (Mg/m^3)	60 g Water Content (%)	60 g ρ_{dry} (Mg/m^3)	Impound-ment Height, H_I (m)	H_{WT}/H_I	R_L/H_I	Failure Mode
FR01	1.959	25.4%	1.562	20.8	0.59 - 0.73	0.88	Slope Instability
FR02	1.860	24.7%	1.492	22.1	0.96	1.75	Slope Instability
FR03	1.891	24.1%	1.524	20.8	1.10	2.63	Slope Instability
FR05	1.590	37.7%	1.155	18.8	0.96	3.95*	Flow Failure
FR06	1.802	34.0% †	1.345	19.6	0.59	1.47	Slope Instability

* Max runout length reached in test FR05

† Calculated using measured water and ash masses

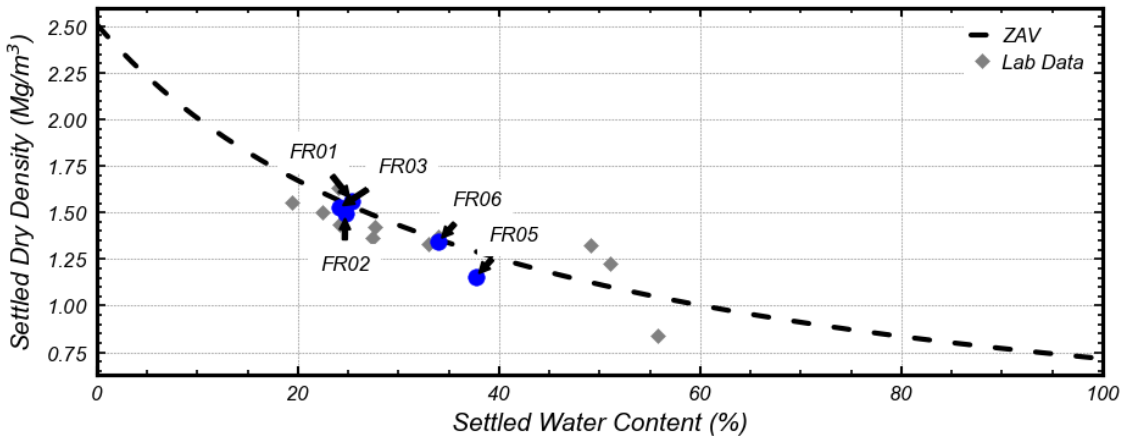

Figure 57. Settled dry density with settled water content for all centrifuge tests.

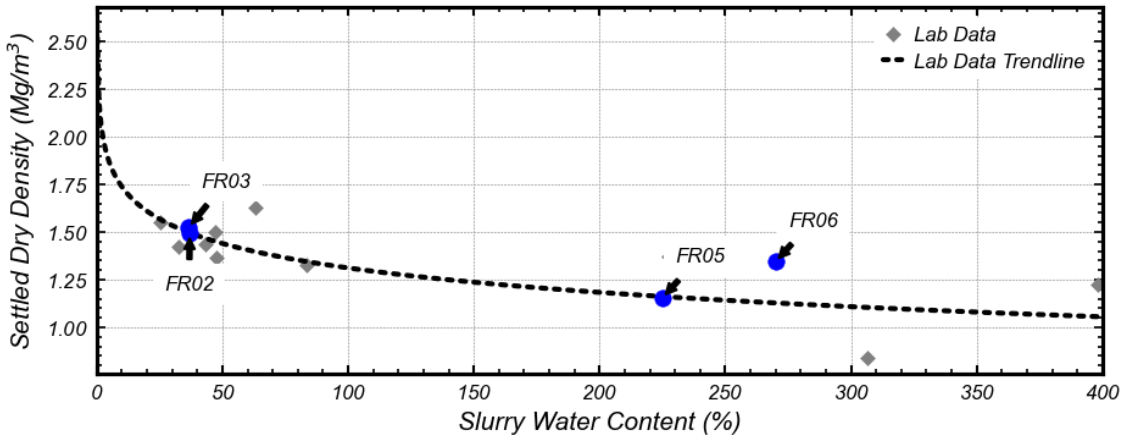

Figure 58. Settled dry density with slurry water content for all centrifuge tests.

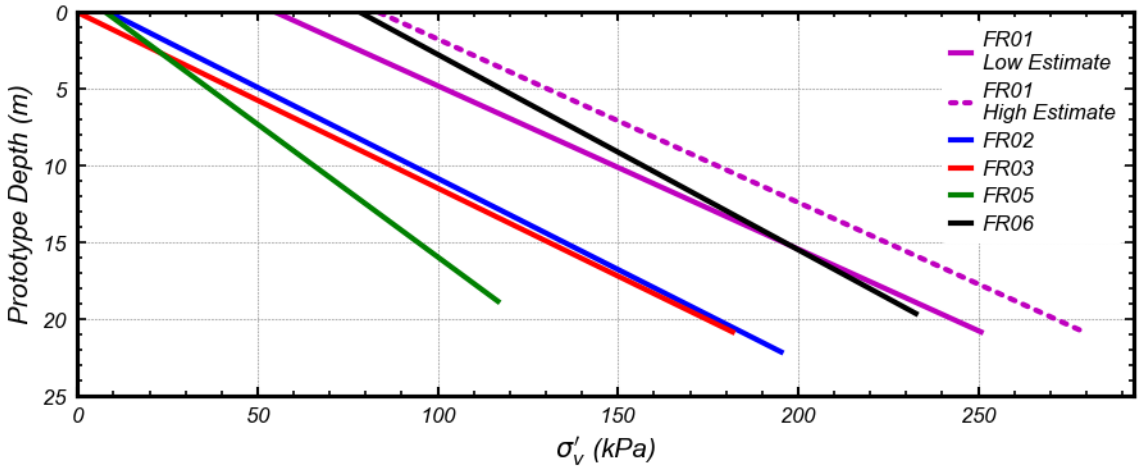

Figure 59. Effective stress profiles with depth for centrifuge tests (χ is assumed to be 1 for all tests).

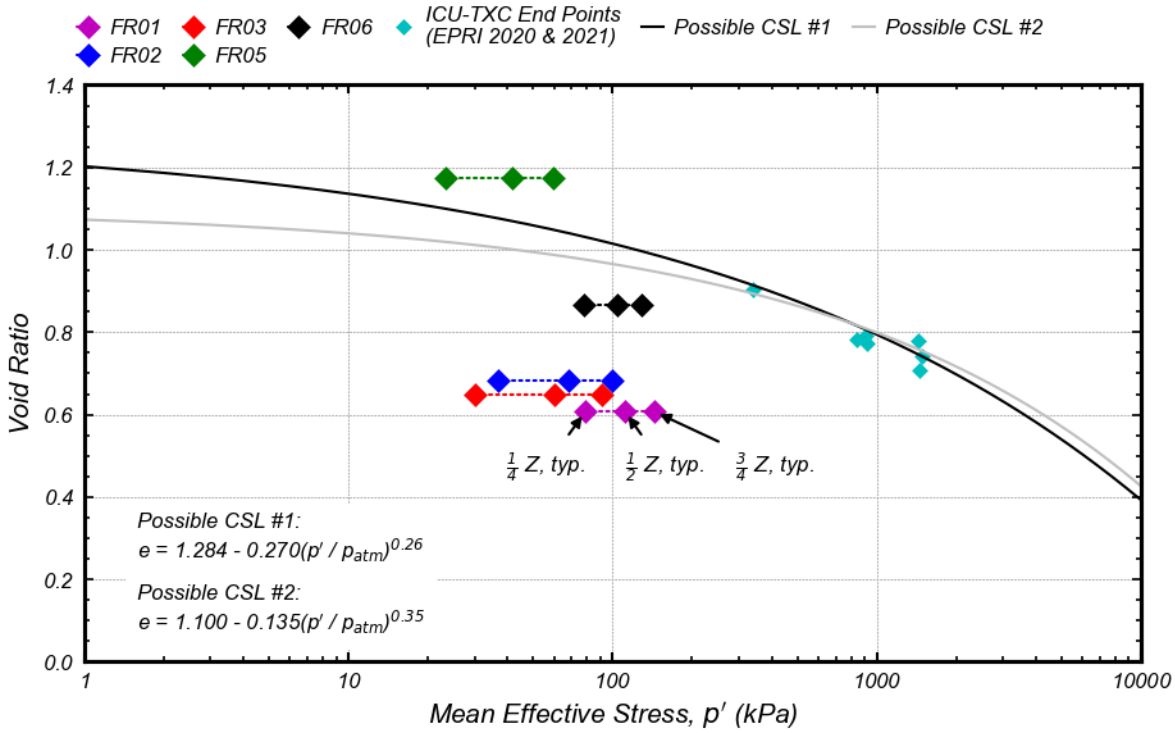

Figure 60. Void ratio vs. mean effective stress for centrifuge and ICU-TXC tests (EPRI 2020 and 2021). *Z* is the depth within the impoundment.

3.8.1 Runout Behavior

Figure 61 and **Figure 62** show the failed deposits for all five tests after the conclusion of spinning. FR01, FR02, and FR06 all have failure masses with clumpy textures, while FR03 has a smoother failure mass. The smoother failure mass in FR03 is most likely due to surficial erosion from pooled water, as the water table height was 10% higher than the deposit height. FR02 and FR06 also have a smoother portion of the failure mass farther out from the container, whereas FR01 has clumps of ash over most of its failure mass, most likely due to a reduction in saturation of ash above the water table. It was also observed that FR01, FR02, and FR03 held a near vertical face for less than one second (model time) after opening of the gates. FR05 experienced a sudden flow failure, which is why the material is spread to the farthest extent of the runout basin. Using

depth-sensing cameras, it was determined in ERPI (2021) that only 24% of the volume of the deposit remained within the container after failure in FR05, which formed a 16° angle with the horizontal plane. **Figure 63** through **Figure 65** show the surface profiles of the deposits after opening of the gates, generated from the depth cameras, for FR02, FR03, and FR05. FR02 and FR03 developed similar surface profiles with time after the opening of the gates, with deformations over time being slow. In contrast, FR05 surface profiles show a quick sinking of the surface within the container, resulting from the rapid flow failure. Comparing runout distances between the tests, FR06 had a smaller final runout length than FR02 and FR03, likely from the decreased water table height. FR01 had a smaller final runout length than FR06. With a similar water table height at the front of the container between the two tests, the difference in runout is most likely due to the decreased density of FR06 compared to FR01. The larger runout distance of FR05 (and flow failure) compared to FR06 is likely due to a reduced density and a higher water table.

Figure 61. FR01, FR02, FR03, and FR06 after spinning.

Figure 62. FR05 after spinning.

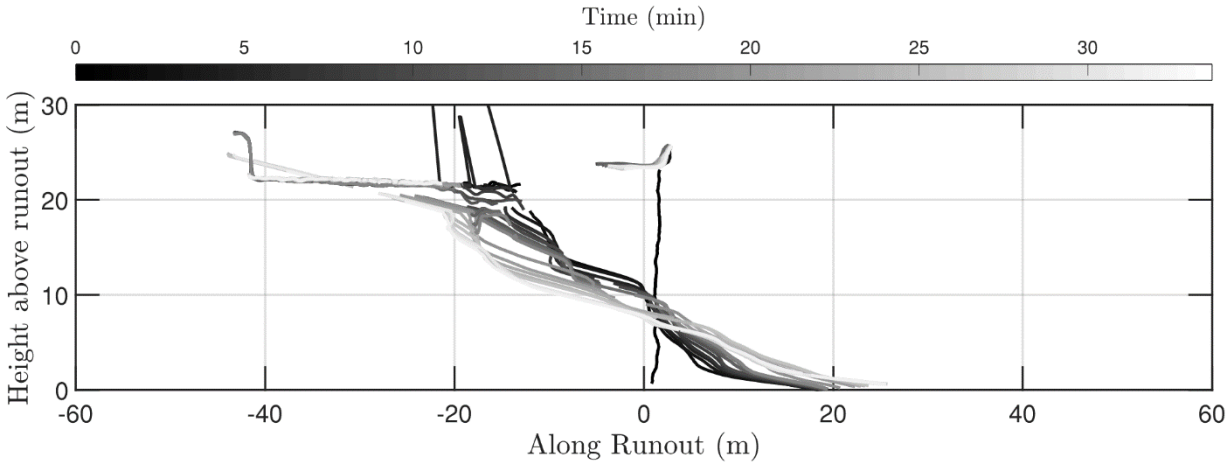

Figure 63. Ash surface profiles from depth sensing cameras for FR02 (EPRI 2021).

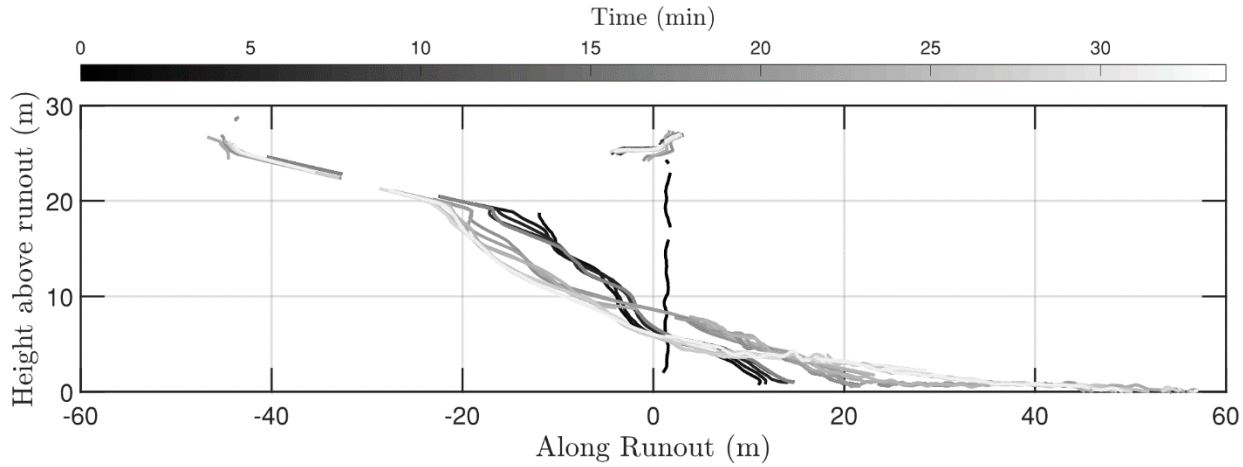

Figure 64. Ash surface profiles from depth sensing cameras for FR03 (EPRI 2021).

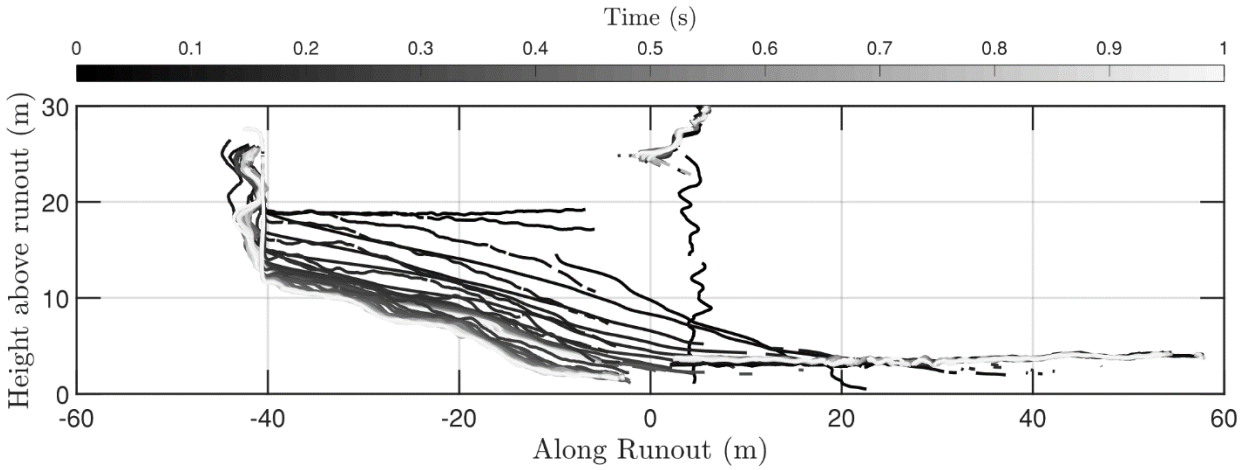

Figure 65. Ash surface profiles from depth sensing cameras for FR05 (EPRI 2021).

3.8.2 Stiffness and Strength Comparisons

The single V_s measurement obtained in FR06 is compared to previous measurements in **Figure 66**. The value matches the general trend found in the denser tests (FR01, FR02, FR03, see **Table 2**), which were measured at various vertical effective stresses. For FR06, the vertical effective stress was calculated using Equation 10, assuming χ is 1. EPRI (2021) fitted the denser tests and the loosest test (FR05, see **Table 2**) with the following power-law form, based on Bachus et al. (2019):

$$\boldsymbol{V_s = \alpha \sigma_v'^{\beta}} \quad (\mathbf{27})$$

Where α and β are material parameters. It was shown in EPRI (2021) that these fitting parameters agree with published values from Bachus et al. (**Figure 67**). The measured V_s in FR06 appears to fit with the determined trendline for the denser tests, which agrees with the observed runout behavior between the four tests. G_{max} is similarly plotted with the previous data in **Figure 66**, with the trendline for the denser tests developed in EPRI (2021) also appearing to fit the data point. Accounting for the lower overall measured density of FR06 compared to the denser tests, the similar V_s measurement is most likely a result of the dewatering performed on the deposit, which

could have resulted in consolidation and a subsequent increase in shear stiffness at the elevation of the measurement. As expected from the results of the runout tests, the measured V_s and G_{max} values for FR05 are much lower than what was measured in the other four tests, indicating that the stiffness of the deposit was much lower than the other four.

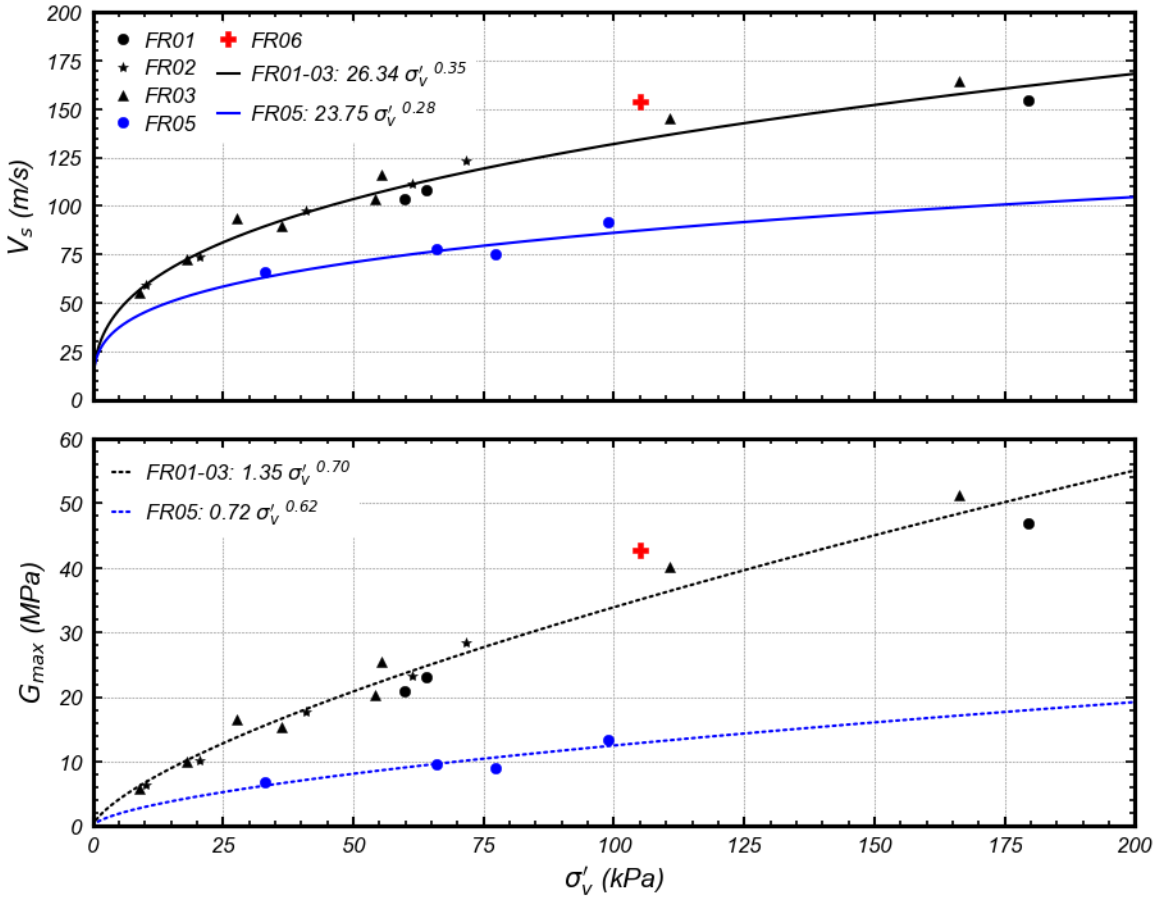

Figure 66. V_s and G_{max} with respect to σ'_v, for all centrifuge tests.

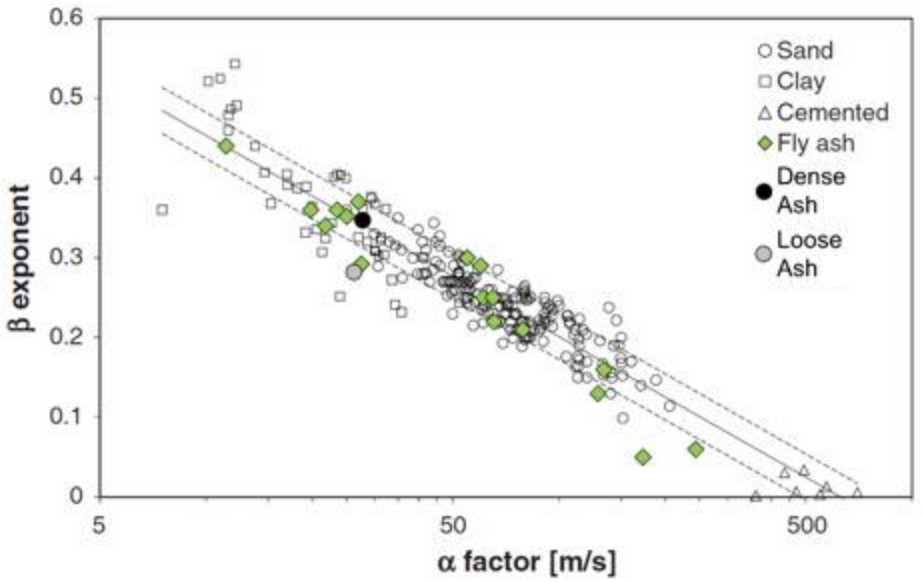

Figure 67. Fitting parameters for determining V_s, based on Bachus et al. 2019 (taken from EPRI 2021).

Undrained (i.e. fast) and drained (i.e. slow) CPT pushes were performed in EPRI (2021) for FR02, FR03 and FR05, while only an undrained push was performed in FR01. Because of the sloping water table after dewatering in FR01 and a lack of a drained push, FR01 CPT data is not included in these comparisons.

Figure 68 shows the undrained and drained resistances obtained from the CPT soundings in the four tests. Note that the rapid increases in resistance for FR02 and FR03 at depths greater than 16 m for both penetration velocities are due to proximity to the bottom of the container. It should also be noted that the effective stress in FR06 is significantly greater than that of FR02, FR03, and FR05 (see **Figure 59**). In the undrained pushes, FR03 has the largest resistance, followed by FR02 and FR06 having similar resistances. FR05 has a maximum measured q_c value of about 0.35 MPa, which is considerably smaller than the other three tests. In the drained pushes, FR06 has the largest resistance, followed by similar resistances in FR02 and FR03, with FR05

having the lowest resistance. The drained q_c values obtained in FR05 are significantly lower than the other three tests, but not to the degree of difference that was shown with the undrained values.

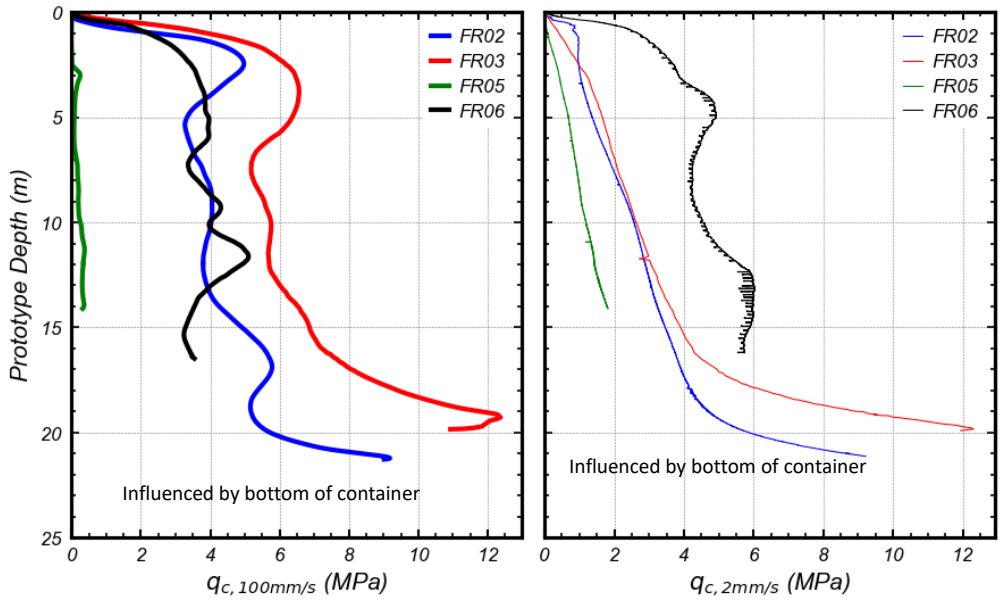

Figure 68. Undrained and drained q_c for FR02, FR03, FR05, and FR06.

Figure 69 plots the ratio of undrained q_c to drained q_c for the tests. FR02 and FR03 have larger ratios of undrained to drained resistance than the other tests, especially in the upper 5 m (prototype scale). This is likely due to the generation of negative shear-induced excess pore pressures during undrained penetration, indicating a dilative tendency and a larger undrained strength than drained strength. The ratio of undrained to drained resistance decreases with depth for these two tests, which is likely from the increase in confining stress with depth, which would suppress shear-induced dilatancy. FR05 has an undrained to drained ratio below 1 for the entire depth, with a ratio close to zero to a depth of 2.5 m, due to the undrained push encountering near-zero resistance until this depth. The low undrained to drained tip resistance ratio suggests that the material would behave contractively under shear (due to generation of positive shear-induced

excess pore pressures during undrained CPT penetration, suggesting a smaller undrained than drained strength), which matches the runout test observations. FR06 has an undrained to drained resistance ratio slightly below 1 until a depth of 11.5 m, with the ratio decreasing below this depth, due to a decrease in undrained and increase in drained resistances, which indicates an increase in contractive behavior below 11.5 m. Partial drainage conditions may have also been present during the undrained push for FR06 above the water table (8 m depth), which would suppress the shear-induced dilatancy of the ash (whether dilative or contractive). The undrained to drained resistance ratio may also be less than 1 at the top of the deposit in FR06 due to positive excess pore pressures generated during displacement of the ash by the CPT probe, as discussed in section **3.4.2**, despite negative shear-induced pore pressures observed at a depth of 4.6 m. Undrained strength ratio (s_u/σ'_v) is also plotted in **Figure 69**, with similar trends to the undrained to drained resistance ratio measurements. A cone factor (N_k) of 12 was used for all the centrifuge tests to determine s_u (from EPRI 2021). The undrained strength ratio exceeded 1 in all tests, except for FR05 where it ranged from 0.1 to 0.6. Average values of undrained strength ratio for FR02, FR03, FR05, and FR06 at depths of 10 m to 15 m were 2.80, 4.47, 0.15, and 1.87, respectively.

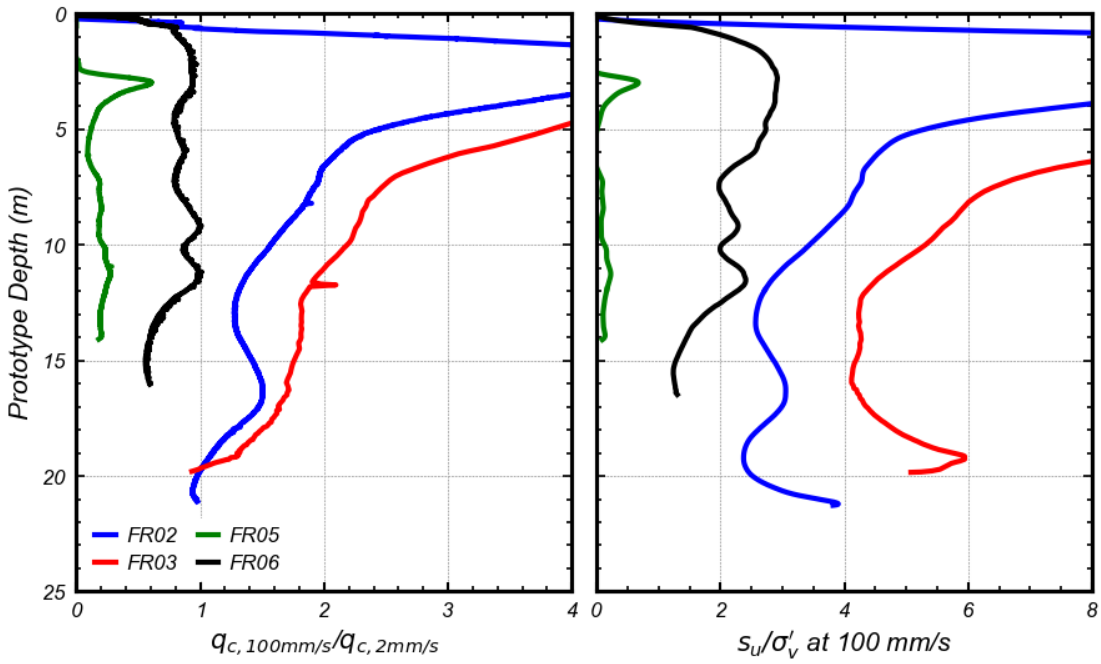

Figure 69. 100 mm/s to 2 mm/s q_c comparison and s_u/σ'_v for FR02, FR03, FR05, and FR06.

The Q_{tn} values for the four tests are compared in **Figure 70**, based on the undrained pushes. The effective stress normalization of tip resistance used to determine Q_{tn} results in a large spike for FR02 and FR03 in the top 5 m, similar to the undrained to drained resistance ratios, with a more constant value obtained below this depth for the two tests. Q_{tn} also provides a metric to account for the increased effective stress in FR06 that resulted from dewatering, which helps compare its results to the other three CPT test results, which were not significantly dewatered. FR03 has the highest Q_{tn} values, followed by FR02 and FR06, respectively. FR05 has the lowest Q_{tn} values, consistent with the other CPT measurements. Both FR02 and FR03 plot in or greater than the Robertson (2010) transition zone for $Q_{tn,cs}$, as shown in **Figure 70**, indicating strong dilative behavior in the upper 5 m and slightly dilative behavior below. FR05 has significantly lower $Q_{tn,cs}$ values than the transition zone, which supports the static liquefaction behavior

observed. FR06 has lesser values than FR02 and FR03, likely from a reduced density, and much larger values than FR05 due to an increased density and lower water table.

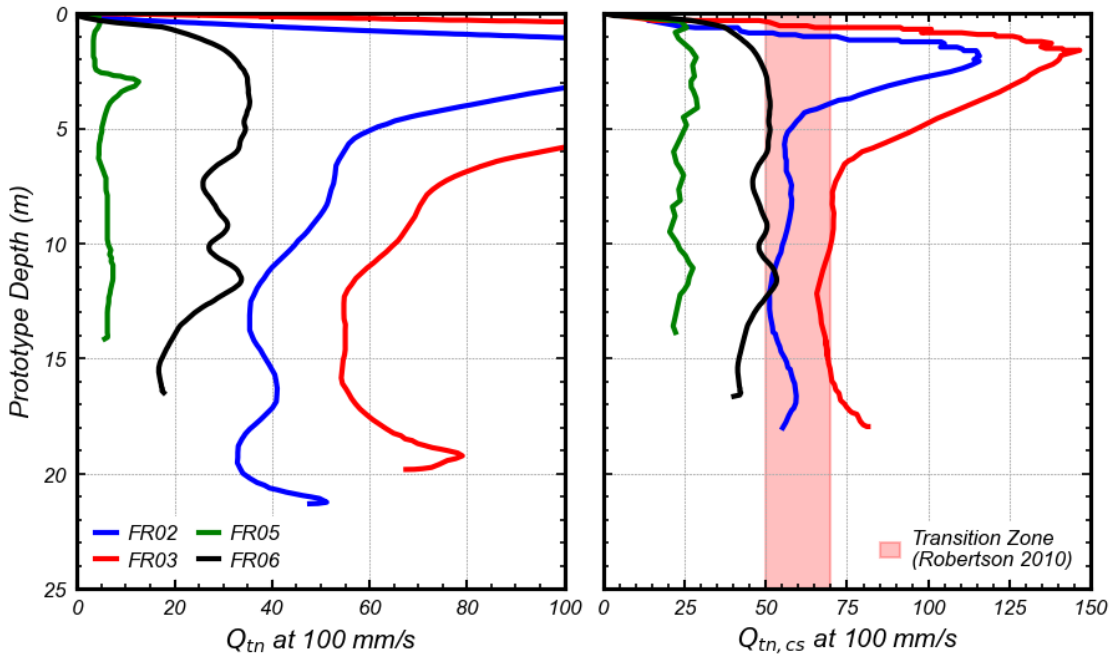

Figure 70. Q_{tn} and $Q_{tn,cs}$ with depth for FR02, FR03, FR05, and FR06.

The CPT results generally agree with the runout lengths observed for the four tests, with the higher q_c, $q_{c,\ 100\ mm/s}/q_{c,\ 2\ mm/s}$, Q_{tn}, and $Q_{tn,cs}$ values being found for FR02, FR03, and FR06, and FR05 significantly lower. This agrees with the much greater runout length and sudden flow failure during FR05. Differences between FR02/FR03 and FR06 are likely due to the lowered water table and smaller density in FR06.

3.8.3 Pore Pressure Comparisons

Excess pore pressure readings at the opening of the gates from the previous tests are shown in **Figure 72** through **Figure 75**, with **Figure 71** being the legend for the past pore pressure data. FR01 developed negative excess pore pressures at the opening of the gates, which remained constant after small spikes to a less negative value. The amount of negative excess pore pressure

was greater towards the front of the container than the back. EPRI (2021) reported that no water was observed to exit the model, so the negative pore pressures can be assumed to be from dilation of the ash. FR02 also developed negative excess pore pressures upon opening of the gates, with larger and slower spikes than what was observed in FR01. Similarly, the change in pore pressure was greater towards the front of the container. Tensiometers towards the bottom front of the container also show a slow decrease after spikes in pore pressure. FR03 shows very similar behavior to FR02, with large negative pore pressure spikes and tensiometers towards the bottom front showing a slow decrease in pore pressure. The magnitude of the negative pore pressure spikes increases from FR01 to FR02, and again from FR02 to FR03, all of which had similar densities. FR05 only had three working tensiometers during the test. After opening of the gates, a small spike in positive pore pressure is shown in PPT1-1 and 3-3, with pore pressures decreasing immediately after. This decrease coincides with a significant volume of material exiting the container. Differences in excess pore pressures at each PPT row in the tests may be due to differences in applied shear strain, similar to what was observed in FR06.

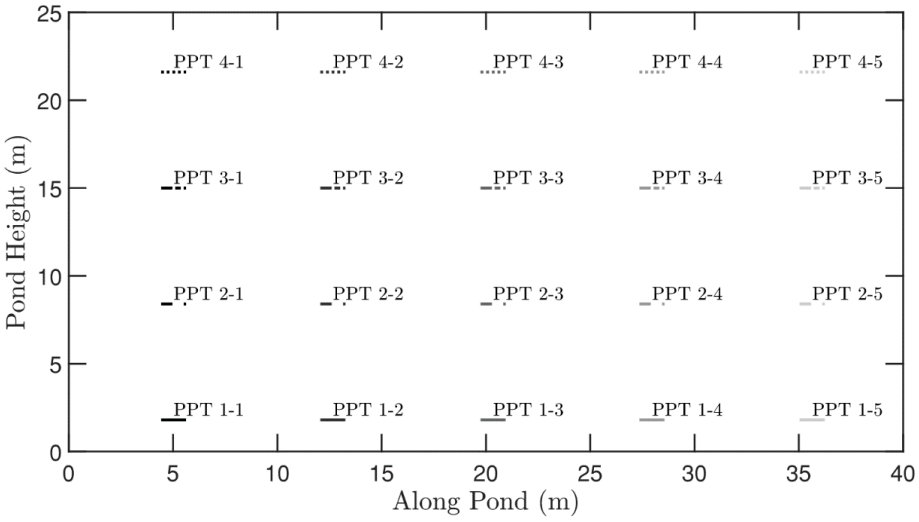

Figure 71. Legend for EPRI (2021) pore pressure data (gates are at 40 m).

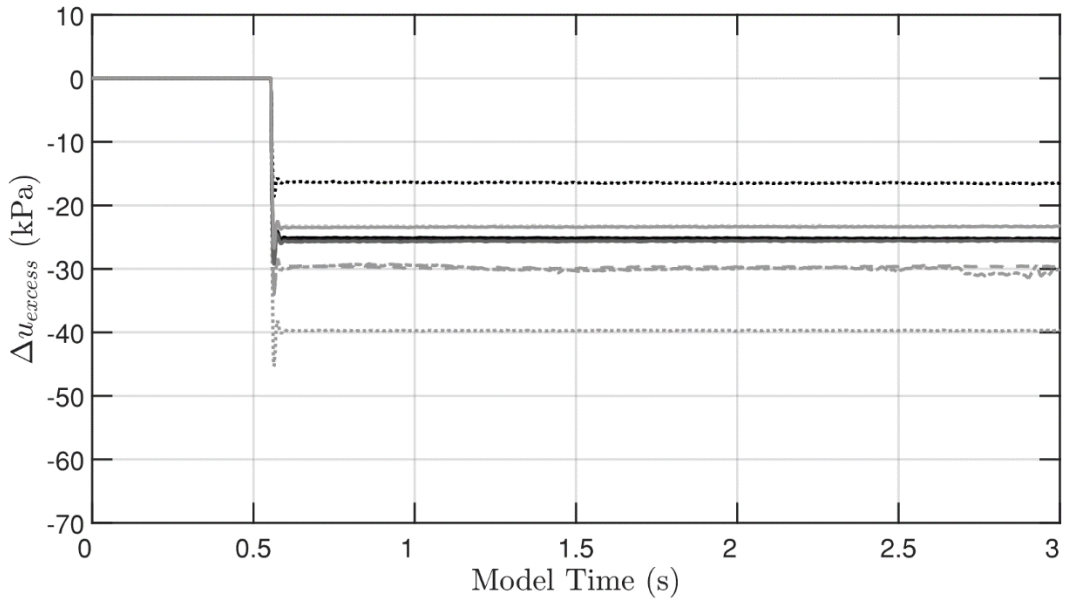

Figure 72. Pore pressure response during gate opening for FR01 (EPRI 2021).

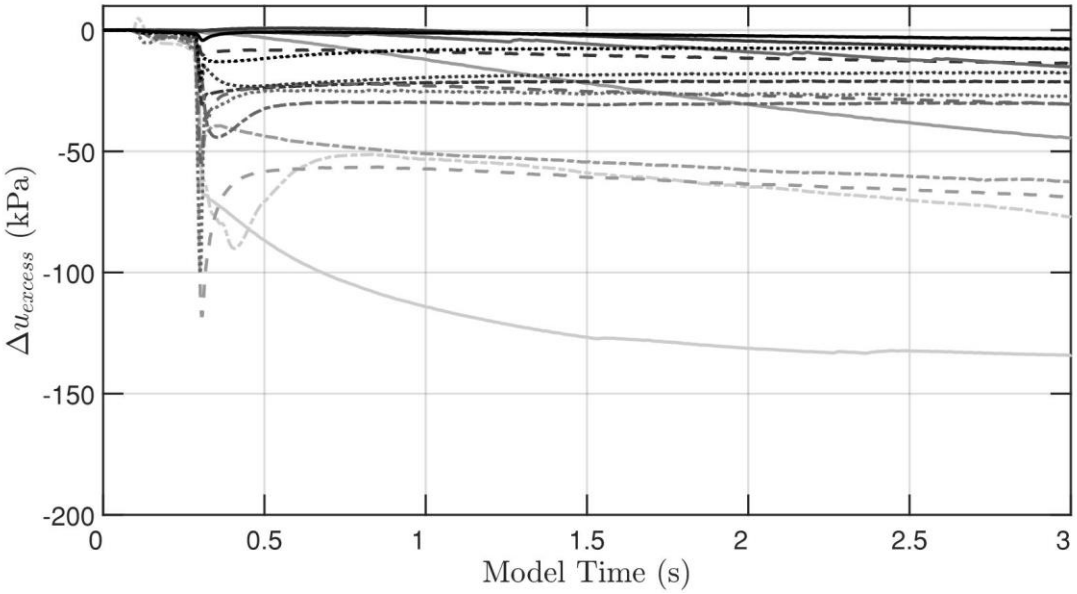

Figure 73. Pore pressure response during gate opening for FR02 (EPRI 2021).

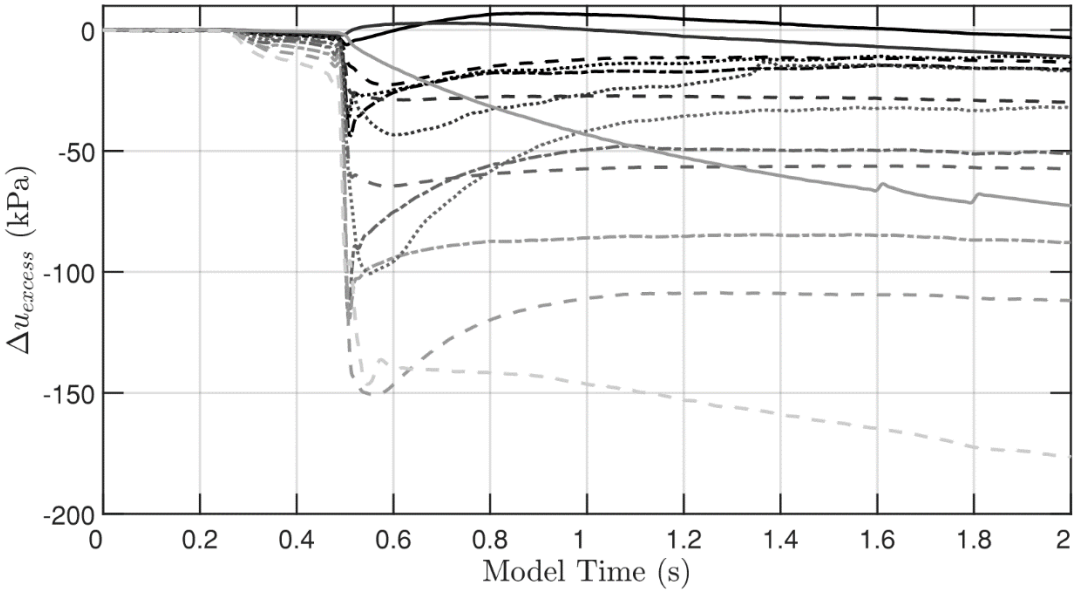

Figure 74. Pore pressure response during gate opening for FR03 (EPRI 2021).

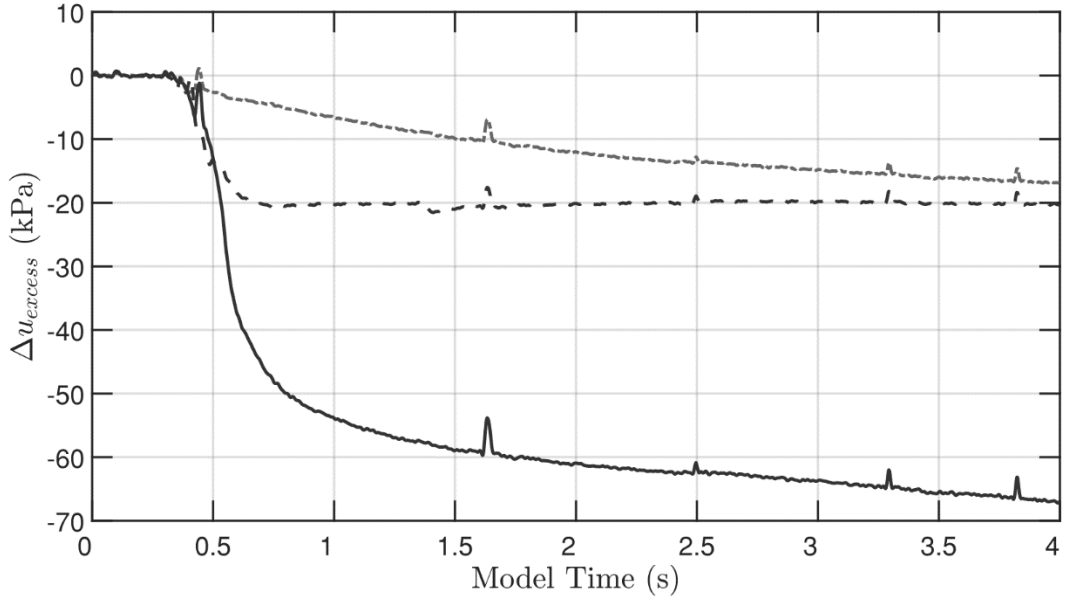

Figure 75. Pore pressure response during gate opening for FR05 (EPRI 2021).

Similar to what was done to analyze FR06, Equation 24 was used to calculate the change in mean total stress upon opening the gates at PPT rows 1, 2, and 3, which results in an equal

excess pore pressure. It is assumed that the ash is a fully saturated (including above the water table), isotropic elastic soil. Similar to what was done for **Figure 60**, the average of the low and high bounds of vertical effective stress were used to calculate the change in mean total stress for FR01. The difference between the change in mean total stress and the maximum measured excess pore pressure at each PPT row is shown in **Table 3**. Assuming there is no seepage immediately after opening the gates, these values can be approximated as the shear-induced excess pore pressures. From these values, FR01 exhibits dilative behavior at PPT row 3, negligible dilatancy at PPT row 2, and contractive behavior at PPT row 1. FR02 and FR03 both show dilative behavior in PPTs rows 2 and 3, and contractive behavior in PPT row 1. FR05 shows dilative behavior at all three PPT rows, consistent with the observed flow failure.

Table 3. Maximum Δp* minus $\Delta u^{\dagger}$ (kPa), after opening of the gates.

Loc. \ Test	FR01	FR02	FR03	FR05
PPT Row 3	-43.9	-46.8	-78.2	19.3
PPT Row 2	4.0	-28.9	-62.8	59.7
PPT Row 1	59.2	67.6	128.7	100.7

* Change in mean total stress calculated based on equation 24 and K_0 of 0.5. † Maximum magnitude of excess pore pressure measured by each PPT row.

As shown in **Figure 48**, FR06 showed dilative behavior at a prototype depth of 4.6 m, marginal dilatancy at depths of 7.9 and 11.2 m, and contractive behavior at depth of 17.8 m. The general trends of shear-induced excess pore pressures are similar between FR01 and FR06, which were both dewatered in flight. The larger magnitude of shear-induced dilation at the top of the deposit and smaller magnitude of shear-induced contraction at the bottom of FR01 are most likely

due to the larger ash density in FR01, compared to FR06. FR02 and FR03 exhibited dilative behavior to deeper depths than FR01 and FR06, possibly due to the reduced confining stress with depth since dewatering was not performed below the surface of the ash in FR02 and FR03.

Figure 76 through **Figure 78** show the calculated hydraulic gradients in FR01, FR02, and FR03. Due to only three of the tensiometers working for FR05, lateral hydraulic gradients were not calculated for this test. Highlighted with gray shading in Figure 74, positive hydraulic gradients at the front of the pond are not representative of actual data, due to the tensiometers used to generate these gradients being exposed to air after the initial slope failure of FR01. FR01 (with an H_{WT}/H_I ratio ranging from 0.73 at the back to 0.59 at the front of the deposit) shows a similar gradient profile with depth in the back and middle of the deposit, with gradients increasing to a time of 1.03 minutes (model scale) and then decreasing after. This indicates that flow is heading towards the front of the deposit. FR02 shows greater negative hydraulic gradients, as the water table was higher than in FR01, indicating greater flow out of the deposit. FR03 experienced small hydraulic gradients at the back of the deposit. Large negative hydraulic gradients were shown to occur at the middle and front of the deposit at a time of 10 minutes, which decreased at a time of 30 minutes, indicating a large initial flow that decreased over time. The pooled water on top of the deposit most likely contributed to the high hydraulic gradients, which is consistent with the increased runout length observed in FR03.

From the lateral hydraulic gradient data in the four tests analyzed, the magnitude of the hydraulic gradients was found to depend on the water table height, which directly corresponds with the total head drop of the system after the opening of the gates. FR01 and FR06 had lowered water tables and exhibited the least negative hydraulic gradients, FR02 had a water table at the

surface of the ash and had higher hydraulic gradients, and FR03 had a water table above the surface of the ash and had the largest hydraulic gradients.

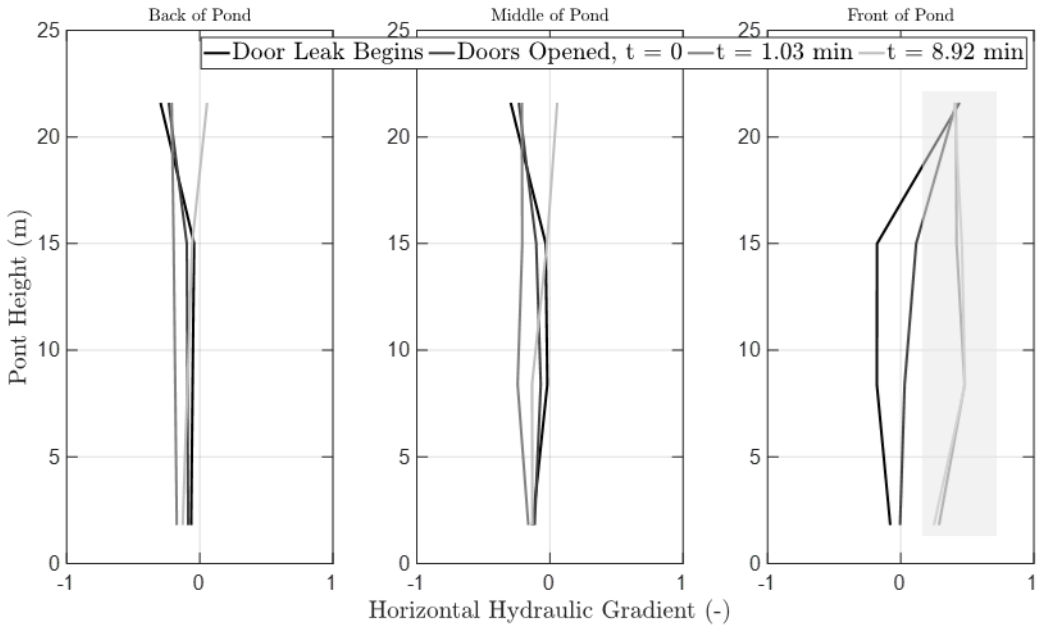

Figure 76. Lateral hydraulic gradients during FR01 (negative gradients indicate flow from back of container towards gates, EPRI 2021). Note that the positive gradients highlighted in gray at the front of the pond are not representative of actual data, due to material runout after opening of the gates.

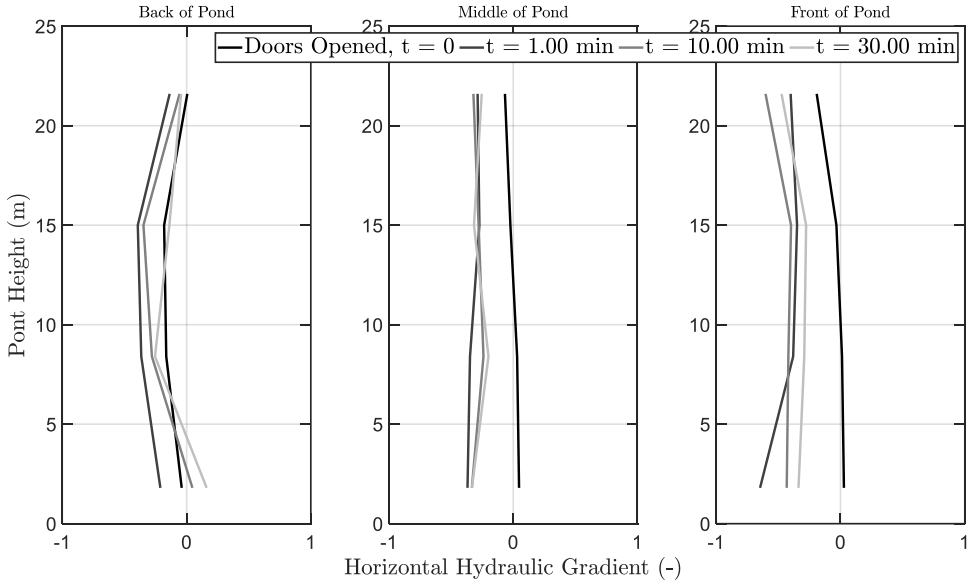

Figure 77. Lateral hydraulic gradients during FR02 (negative gradients indicate flow from back of container towards gates, EPRI 2021).

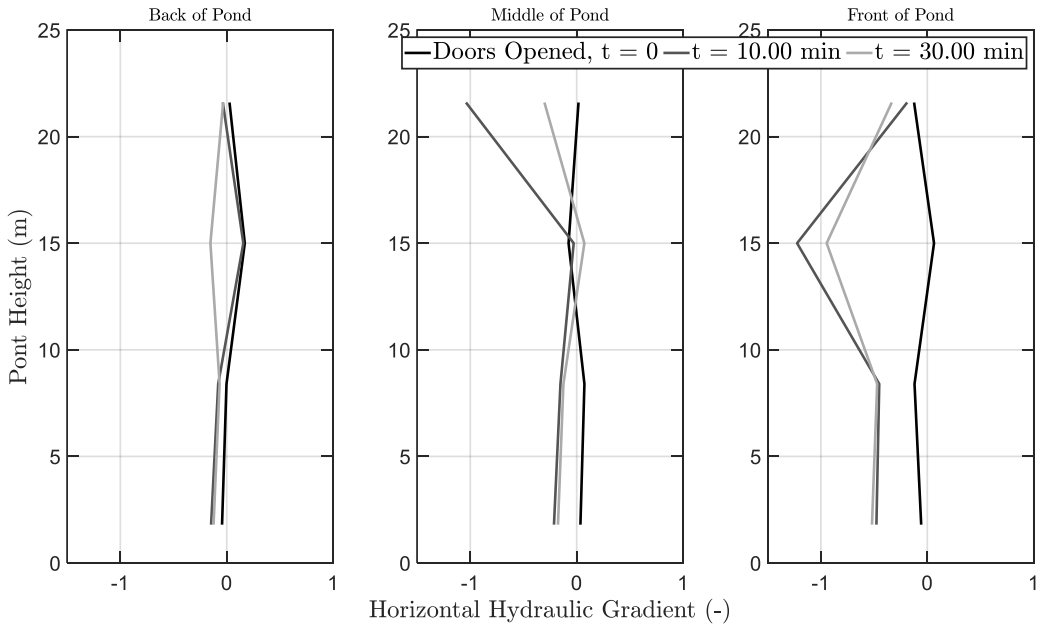

Figure 78. Lateral hydraulic gradients during FR03 (negative gradients indicate flow from back of container towards gates, EPRI 2021).

3.8.4 Water Content Comparisons

Figure 80 through **Figure 82** present the water content data in EPRI (2021), **Figure 83** plots the conductivity data for FR05, and **Figure 79** is the legend for the data. FR01 only had three moisture probes installed, while the other three tests used 10 moisture probes. FR05 was judged by EPRI to not have representative readings of water content, due to the measured conductivities of roughly 1800 to 3700 µS/cm (corresponding to approximately 16 to 23% water content) not matching with the estimated bulk water content of about 38%. This is similar to FR06, which had measured water contents of 15 to 20% but was estimated to have a bulk water content of 34%. Measured water contents for FR01, FR02, and FR03 are all roughly 25%, which is the estimated liquid limit of the ash. Water contents after opening of the gates are also relatively constant in FR01. FR02 had decreases in water content at MP3-1 and 3-2, while FR03 had decreases in water content at MP2-3, 3-1, and 3-2. MP3-3 and 4-3 are both exposed during the slope instability

failures of FR02 and FR03. After the sudden flow failure in FR05, only MP1-1, 1-2, and 1-3 remain within the ash deposit, as shown by their relatively stable conductivity values compared to the other seven moisture probes, which were exposed after the failure. FR06 shows similar behavior for exposed moisture probes after opening of the gates to FR02 and FR03, shown by MP3-3 and 4-3 in **Figure 52** and **Figure 53**. Water content readings in MP3-1 and 3-2 are also shown to decline by 3 to 4% overt time after opening of the gates, consistent with what was observed in FR02 and FR03. Based on the centrifuge results, the point of non-uniqueness in the calibration of conductivity readings to water content may be different than what was determined from the laboratory calibrations, possibly due to differing boundary conditions between the plastic container used for calibration and the metallic container used for centrifuge testing. Certain water content measurements at the front of the deposit in tests FR02, FR03, and FR06 decrease with time, indicating flow of water out of the front of the ash during these tests (FR01 did not have moisture probes at the front of the deposit).

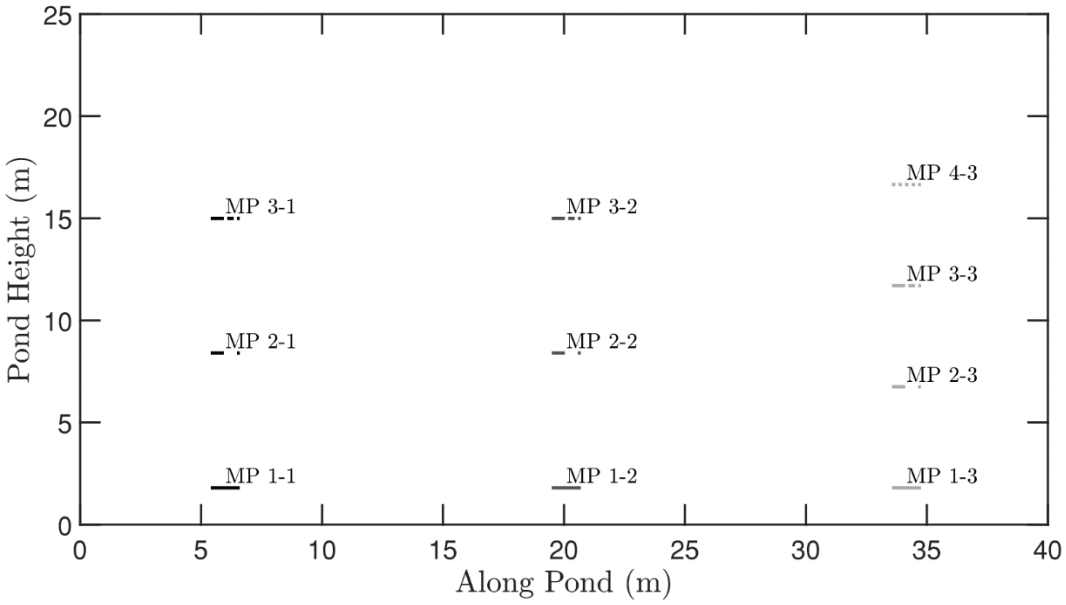

Figure 79. Legend for EPRI (2021) water content data (gates are at 40 m).

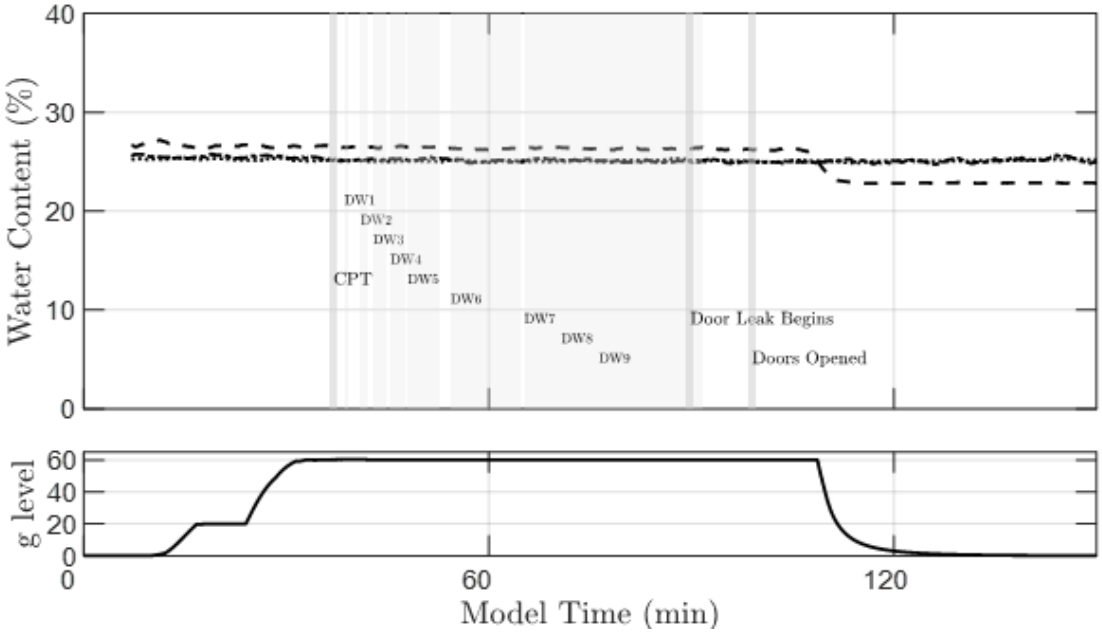

Figure 80. Correlated water content with time during FR01 (EPRI 2021).

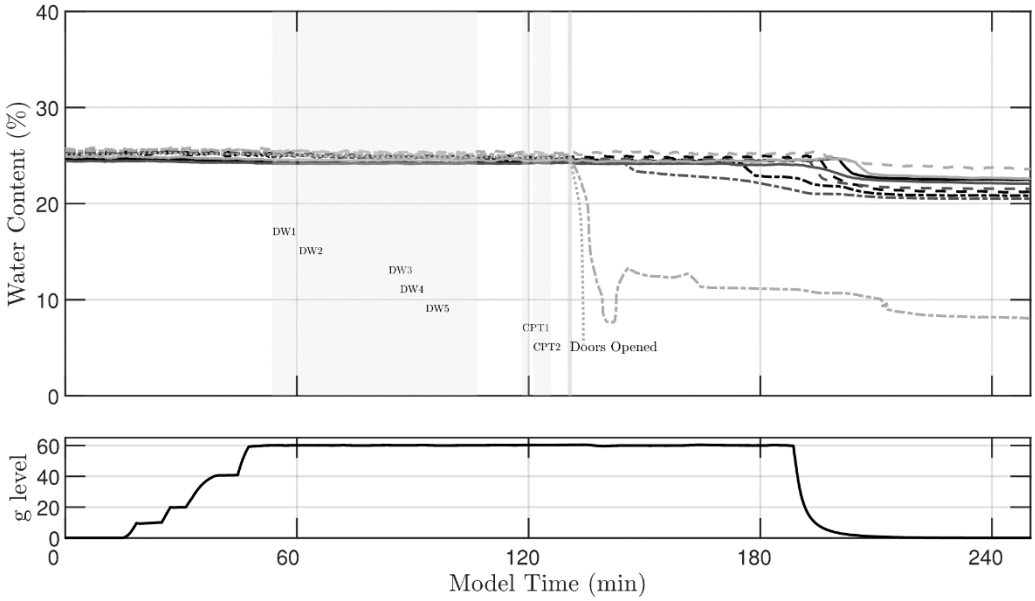

Figure 81. Correlated water content with time during FR02 (EPRI 2021).

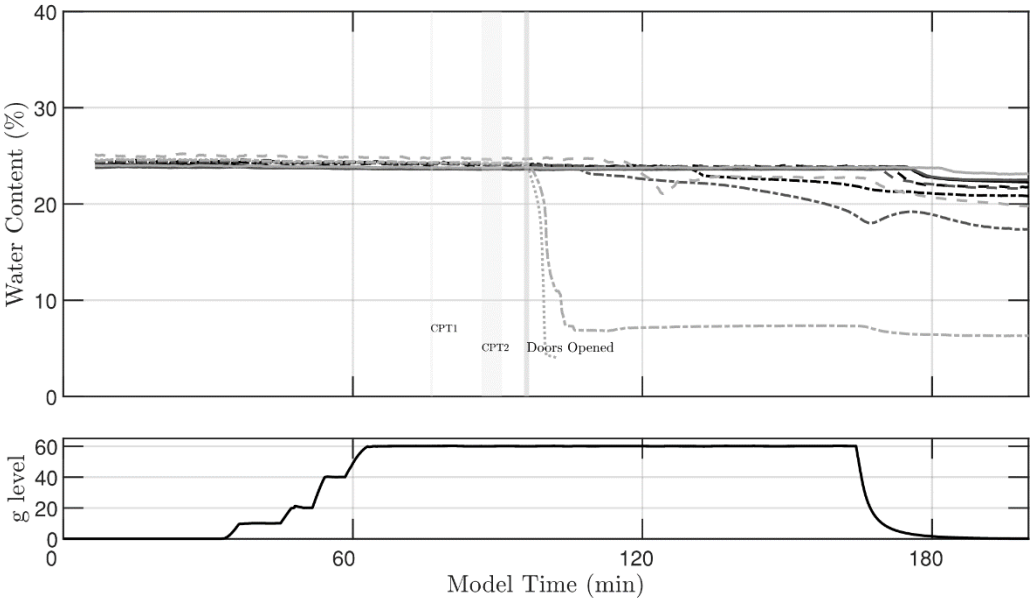

Figure 82. Correlated water content with time during FR03 (EPRI 2021).

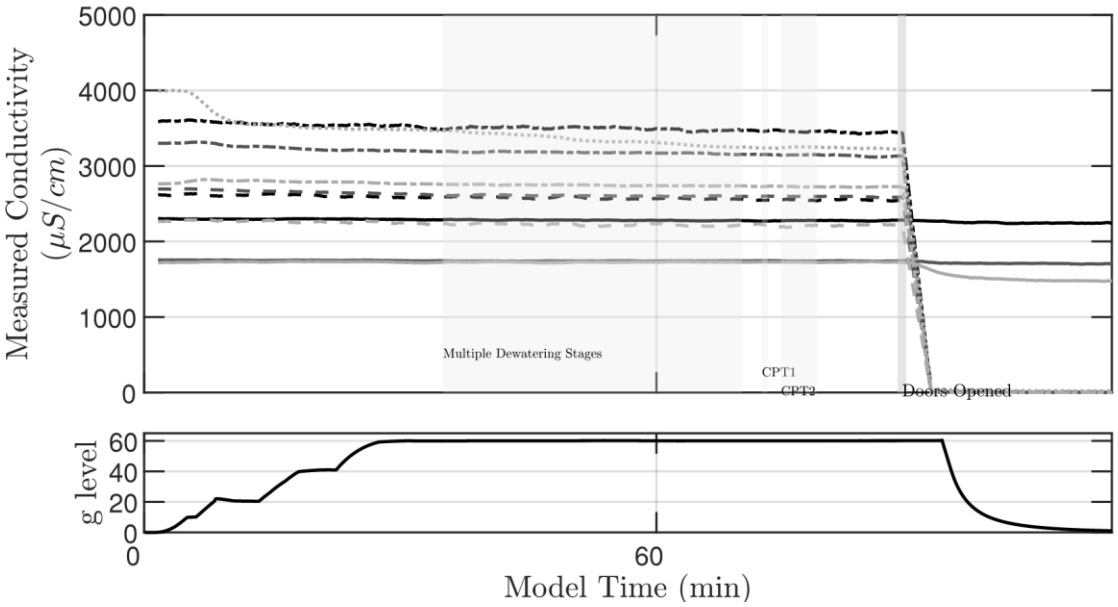

Figure 83. Conductivity with time during FR05 (EPRI 2021).

4 1 G TESTING

Three 1 g tests (T1, T2, and T3) were performed to refine the relationship between initial density of the ash and its runout behavior and to compliment the five 9-m centrifuge tests. Three T-bar penetration tests were performed per model and moisture probe readings were taken during specimen preparation and runout testing. Despite the density measurements for the 1 g tests being inconclusive, a clear correlation of runout behavior and T-bar penetration resistance was found. Issues in the moisture probe calibrations were again found in the 1 g tests, with dielectric permittivity and conductivity data with measurements greater than that taken during FR06 able to be added to the comparison to the laboratory calibrations.

4.1 Procedural Sequence for 1 g Testing

Specimen preparation and testing for the 1 g tests were conducted in the following order:

1. The container and container tray were loaded onto the arm of the 9-m centrifuge, with the container sealed and held closed by heavy duty pipe clamps. The 9-m centrifuge was used to allow for T-bar penetration testing using a hydraulic linear actuator, which is generally used to push miniature CPT probes during centrifuge testing (the centrifuge was not spun during 1 g testing). The rotary pneumatic actuators were attached to the container.
2. The moisture probes were installed in the container with the wiring hooked up and the sensors ready to use. The plastic board that holds the tensiometers for centrifuge testing was placed in the container as well, with the empty holes filled with modeling clay to match the setup of the centrifuge tests.
3. Fly ash slurry was deposited into the container over the course of two to three hours for each test, using the procedure described in section **2.3**.
4. The models were allowed to sit for 4 to 7 days (7 for T1 and T3, 4 for T2).

5. Three T-bar pushes were performed. One 100 mm/s push was performed one to two days before opening of the gates, and one 100 mm/s and one 2 mm/s push were performed the day of the runout test, prior to opening of the gates.
6. As much pooled water was siphoned off as possible without disturbing the deposit.
7. The pneumatic linear actuator for opening the gates was attached to the container.
8. All instrumentation was set to its maximum desired sampling frequency, and all cameras were set to record footage.
9. The upstream air accumulator was pressurized, and the pressure was allowed to stabilize.
10. The gates were opened by activating a manual air valve to pressurize the linear and rotary pneumatic actuators. Fly ash runout was allowed to occur until further changes were deemed unlikely.

Between T1 and T2, and T2 and T3, cleanup and sealing of the container for the following test was performed on the centrifuge arm.

4.2 As-Constructed Deposit Properties

The three models were constructed with slurry water contents ranging from 32 to 48%. Specimen preparation and density measurements were performed using the same procedure used for FR06. **Table 4** presents the measured deposit properties. Since the tests were performed at 1 g, no scaling factor is used to communicate the test results. Measured settled densities of the three models ranged from 1.32 to 1.40 Mg/m^3, with the results compared to previous laboratory data in **Figure 84** and **Figure 85**. As a result of the low target for slurry water content, specimen preparation of T2 proved difficult from the thickness of the slurry. Technical difficulties also occurred in the drill used to mix the slurry, resulting in only being able to pour about two thirds of the desired deposit height. The last bucket poured into T2 became thicker after sitting for slightly

extra time during a malfunction of the mixing drill, resulting in a thicker slurry than what was poured for the rest of the model. Even after mixing again, this bucket maintained a thick consistency, causing an uneven surface to form after pouring into the container (see **Figure 86**). At the time of the runout test for T2, some of the clumps at the ash surface visually appeared to have dried from the time of slurry deposition. The heterogeneity and the drying of the ash in T2 may have affected the runout and T-bar test results. Due to the difficulties in measuring the volume of T2, error may be present in the density reported in **Table 4**. For this reason, the tests were not compared to the centrifuge tests from the perspective of critical state soil mechanics, such as was done in **Figure 60**. T1 and T3 each had approximately 1 cm of pooled water at the top of the deposit that could not be removed with a siphon, which also contributed to the uncertainty of the measured water content and density of the sedimented ash, due to difficulties in volume measurement.

Table 4. Measured properties of the 1 g tests.

Test	ρ_{total} (Mg/m^3)	Settled Water Content (%)	ρ_{dry} (Mg/m^3)	Slurry Water Content (%)	H_I (m)	R_L/H_I
T1	1.848	35.5%	1.364	48.1%	0.34	3.62*
T2	1.846	32.0%	1.398	32.0%	0.25	1.44
T3	1.787	35.6%	1.318	40.0%	0.37	3.33*

* Max runout length reached in tests T1 and T3

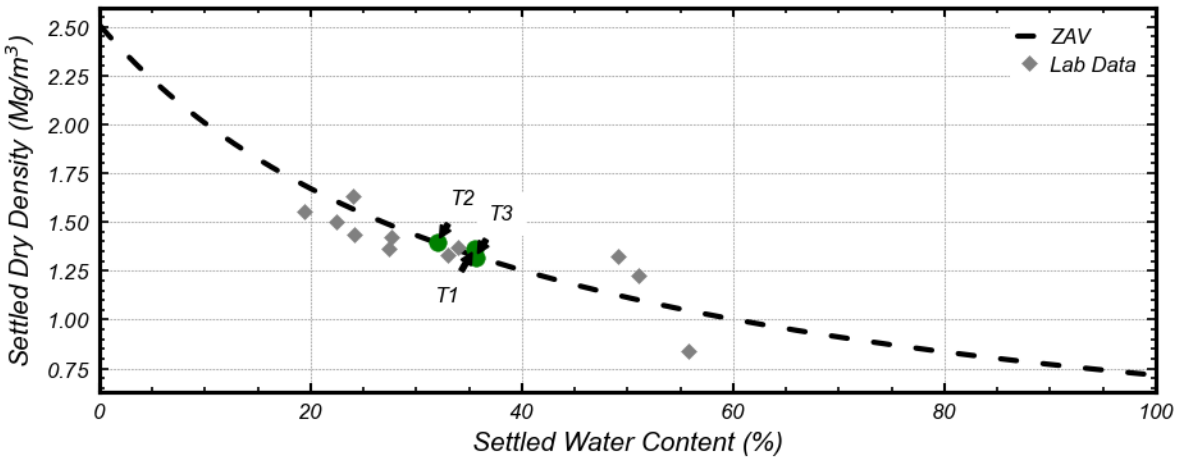

Figure 84. Settled dry density with settled water content for all 1 g tests.

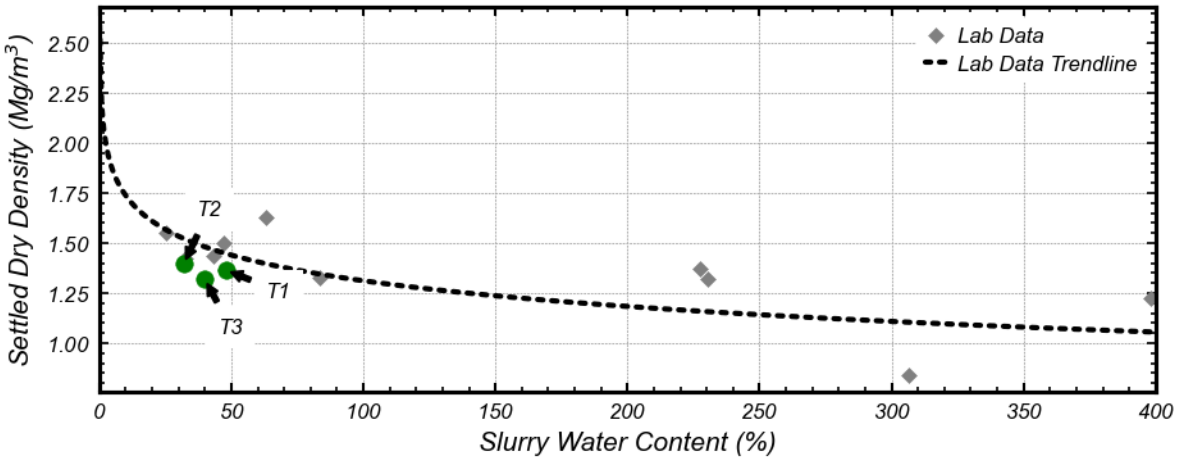

Figure 85. Settled dry density with slurry water content for all 1 g tests.

Figure 86. Uneven ash surface formed during specimen preparation for T2.

4.3 Runout Behavior

The runout length of T1 and T3 both reached the extents of the runout basin, with flow failures occurring. T1 was also observed to have a more liquid-like flow than T3 at the time of testing and on the recorded footage, suggesting a weaker ash deposit. T2 had an R_L/H_I ratio of 1.44 and experienced a slumping-like failure after opening of the gates. **Figure 87** shows the deposits after the runout tests. The ridge at the lower middle of the failure mass of T2 appears to have been influenced by the container, most likely through adhesion with the high vacuum grease used to seal the vertical meeting point of the two gates. **Figure 88** through **Figure 90** show the measured runout length with time of the impoundments, using the Intel RealSense™ D435 Depth Cameras. The runout distance of T1 and T3 both reached the extents of the runout basin within 1 second of opening of the gates. The exact time of the gate opening in T1 was not able to be determined due to an error in the location of one of the depth cameras, which resulted in the time of gate opening not being able to be determined from the recorded footage. Despite similar runout velocities, T1

was visually observed to have a more liquid-like flow out of the container than T3, which agrees with the T-bar results later discussed. T2 experienced most of its runout over the first 30 seconds, with a much slower rate of movement between 30 seconds to 9 minutes after opening of the gates.

Figure 87. T1, T2, and T3 after opening of the gates.

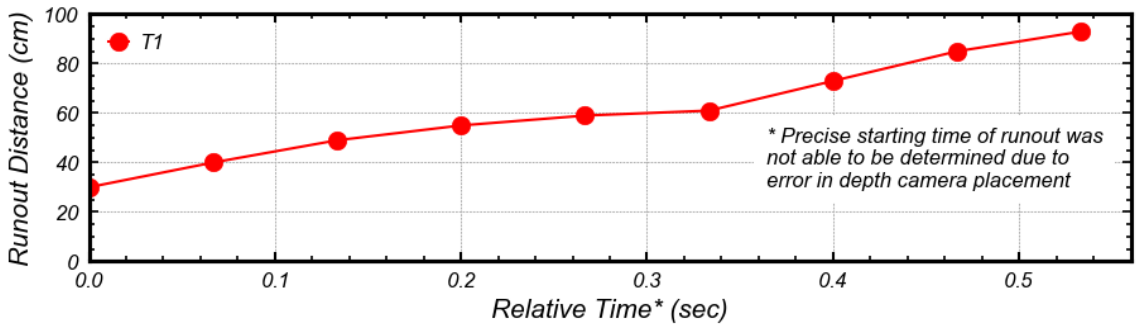

Figure 88. Runout distance during T1.

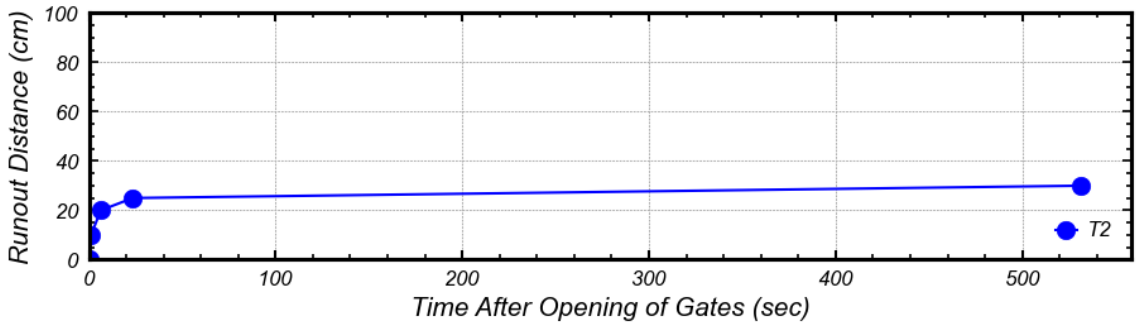

Figure 89. Runout distance during T2.

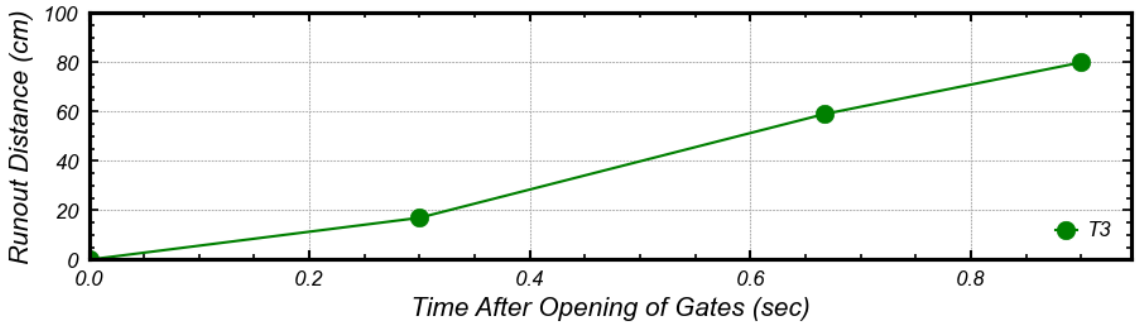

Figure 90. Runout distance during T3.

4.4 Strength Prior to Gate Opening

To assess the changes in strength over time, one fast (100 mm/s) T-bar push was performed one to two days before opening of the gates. One fast and one slow (2 mm/s) T-bar push were then performed the same day as the runout test, prior to the opening of the gates. The extraction of the

T-bar in only the fast pushes was recorded. A small signal to noise ratio of the load cell led to significant noise in the recorded data, as shown in **Figure 91**. A rolling average was used to smooth the data, which was then offset corrected for load and displacement.

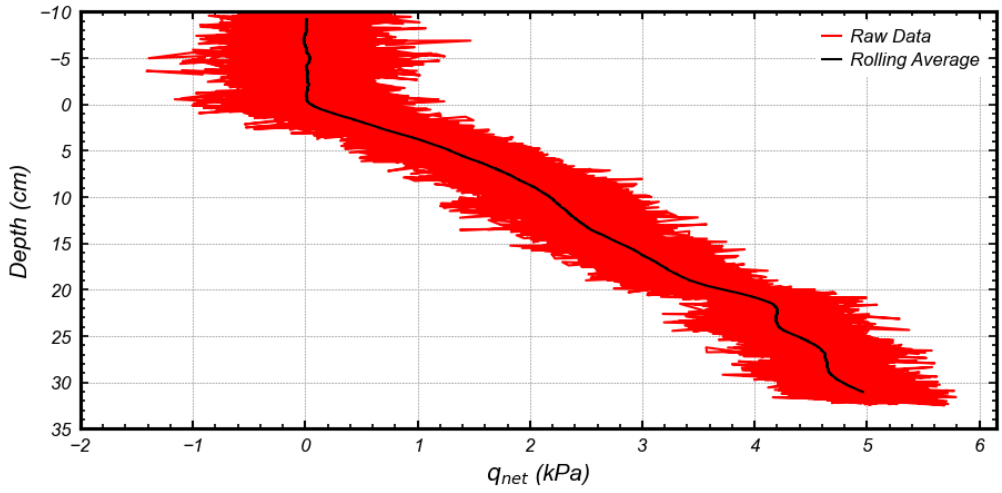

Figure 91. Example of rolling average used for smoothing q_{net}.

Figure 92 through **Figure 94** show the T-bar data for the three tests. For the fast pushes, both the downward resistance (q_{in}) and the extraction resistance (q_{ext}) are plotted. The rapid increases in q_{net} at greater depths shown in blue in T2 and T3 are due to proximity of the bottom of the container. T1 and T3 show a relatively homogenous profile, characterized by smooth curves increasing linearly over depth, with the slow push experiencing smaller resistance than the fast pushes. In T2, the q_{net} profiles vary with depth, possibly due to the difficulties in pouring the thicker slurry required for this model. However, the fast and slow pushes encountered relatively similar resistances. It does not appear drainage conditions varied significantly between the fast and slow pushes.

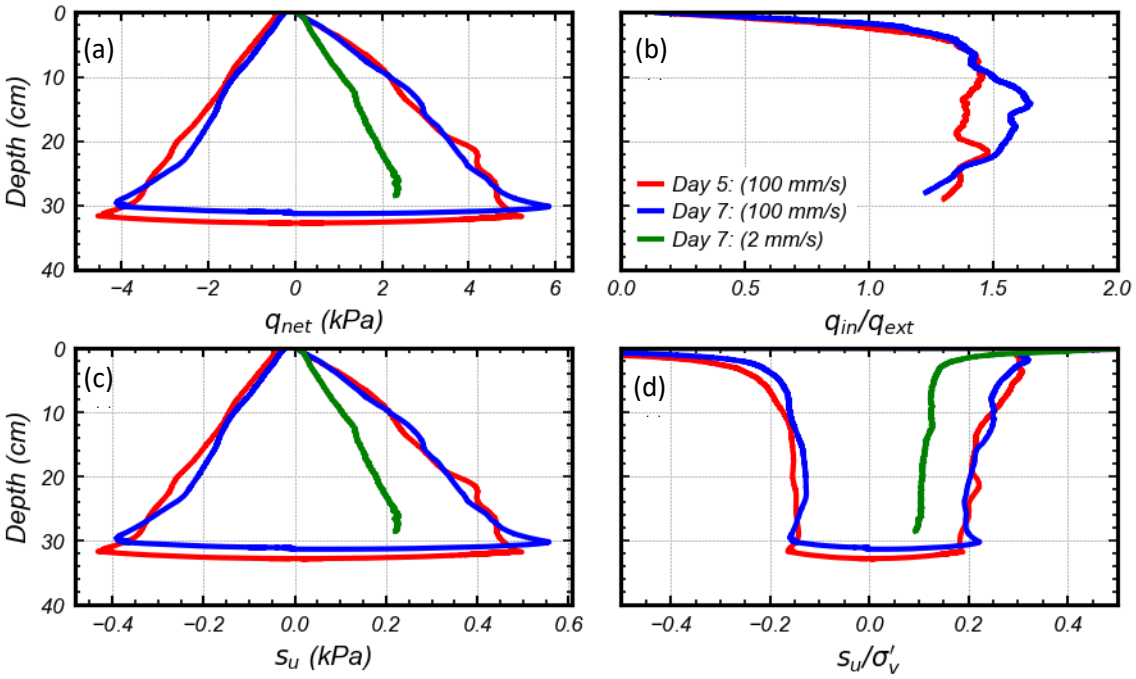

Figure 92. T-bar data with depth for T1; (a) q_{net}. (b) q_{in}/q_{ext}. (c) s_u. (d) s_u/σ'_v.

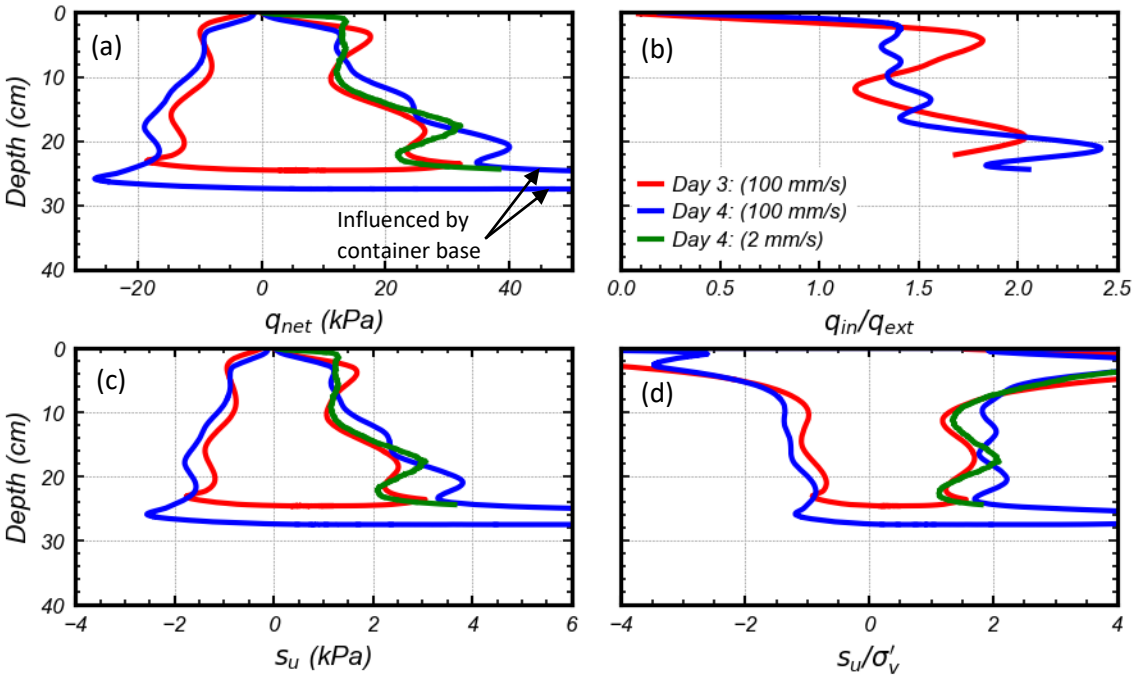

Figure 93. T-bar data with depth for T2; (a) q_{net}. (b) q_{in}/q_{ext}. (c) s_u. (d) s_u/σ'_v.

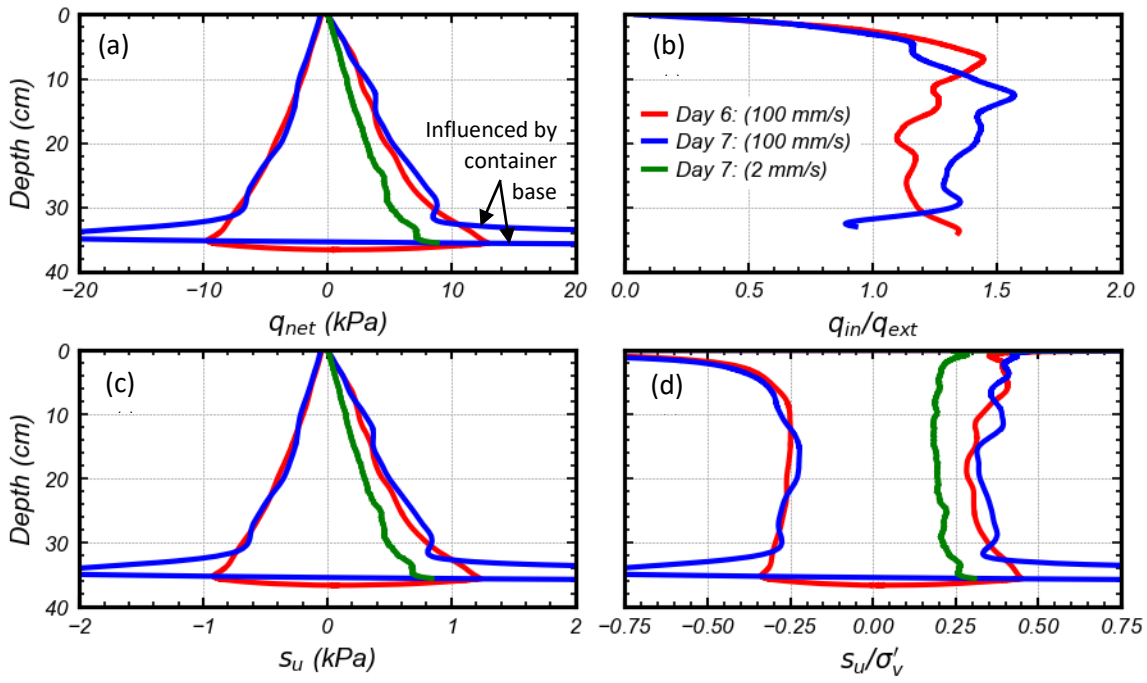

Figure 94. T-bar data with depth for T3; (a) q_{net}. (b) q_{in}/q_{ext}. (c) s_u. (d) s_u/σ'_v.

The extraction ratio (q_{in}/q_{ext}) for each fast push is also shown, which was calculated for selecting a strength factor ($N_{T\text{-}bar}$). Undrained shear strength was determined using the following equation:

$$s_u = \frac{q_{net}}{N_{T-bar}} \tag{28}$$

From DeJong et al. (2011), $N_{T\text{-}bar}$ can be calculated as:

$$N_{T-bar} = 12 - \frac{6.5}{1 + \left(\frac{q_{in}/q_{ext}}{1.8}\right)^{-20}} \tag{29}$$

With the strength factor varying between 6 to 12. Significant scatter was present in the extraction ratio data between the three 1 g tests, so a strength factor of 10.5 was used (similar to Price et al. 2019), which corresponds with an extraction ratio of about 1.7.

Maximum values of undrained shear strength (ignoring the values influence by the bottom of the container) for T1, T2, and T3 were 0.5 kPa, 3.5 kPa, and 1 kPa, respectively. The undrained shear strength obtained from the slow pushes in T1 and T3 is lower than that for the fast pushes, most likely from strain-rate effects. This was not found to occur in T2. Undrained strength ratios from the fast pushes for T1 and T3 were 0.2 and 0.35, respectively. This is consistent with the runout of T1 observed to be more liquid-like than T3. T2 had an undrained strength ratio of about 1 to 2. Initial spikes at the top of profile for undrained strength ratio are a result of full-flow penetration not yet occurring.

4.5 Water Content Results

Similar to FR06, the moisture probes were run at a sampling frequency of 0.01 Hz during specimen preparation and 0.1 Hz during the runout test. **Figure 95** through **Figure 100** show the measured dielectric permittivity, conductivity, and correlated water content during specimen preparation for each test. The initial spikes in the first five hours of T1 and T3 are from the pouring of the slurry and subsequent sedimentation of the ash around the moisture probes. Once the ash is sedimented, the electrical readings of the moisture probes remain constant while the deposit is allowed to sit, indicating that there was little change in water content during this process. Due to the mechanical issues previously described in the specimen preparation of T2, only the bottom seven moisture probes were embedded in the deposit (MP3-1, 3-2, and 4-3 were exposed).

Based on the moisture probes, water contents of about 18%, 26%, and 27% were predicted for T1, T2, and T3, respectively. This does not match what was measured for the deposits by mass measurements (see **Table 4**), with T1 wrongly being predicted as the driest model, when it was wetter than T2. The magnitudes of the predicted water contents for T2 and T3 are similar, but it is correctly predicted that T3 has a higher water content than T2. As shown in **Figure 25**, the

conductivity readings at about 65% water content become non-unique with increasing water content, and the change in conductivity at a range of water contents between 30 to 65% is negligible. It is possible that the water content at which the relationship between conductivity and water content becomes non-unique is lower than what was found in the calibration process, possibly due to differing boundary conditions between the plastic container used for calibration and the metallic container used for runout testing.

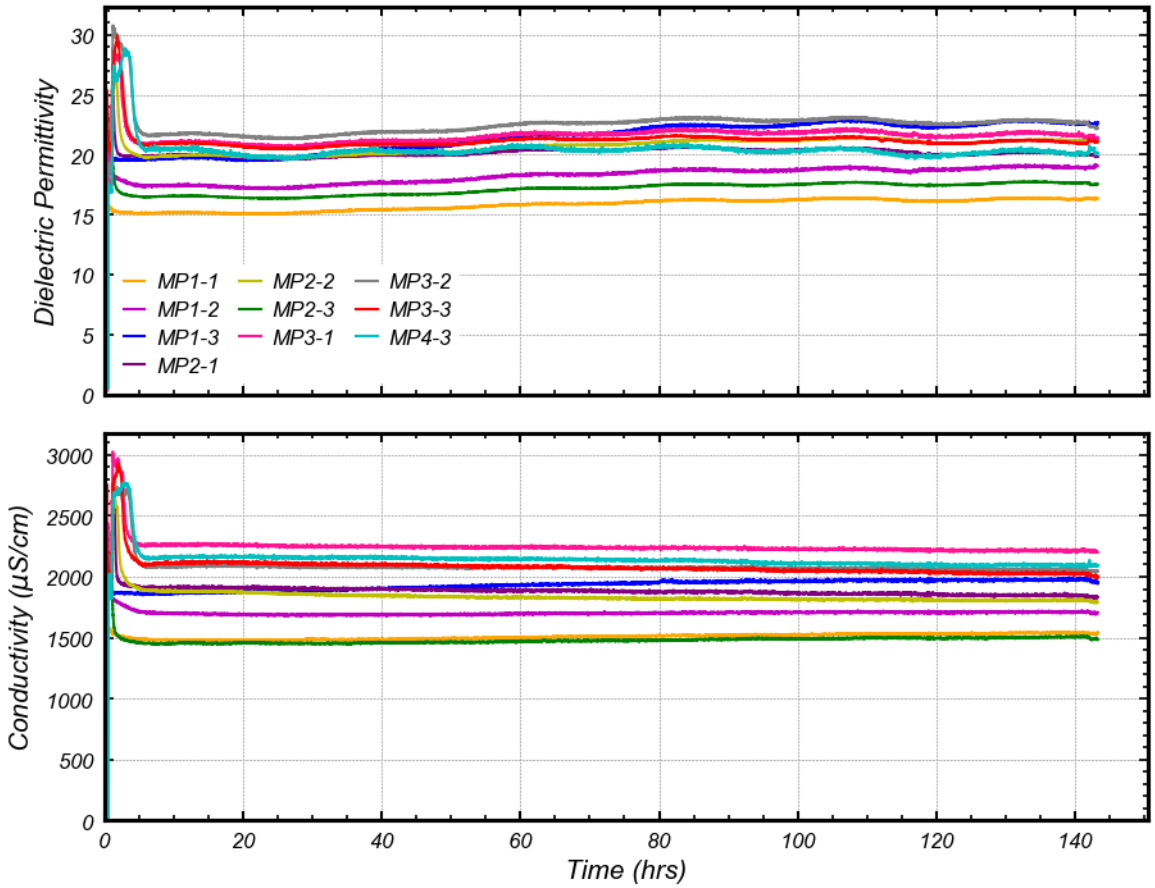

Figure 95. Dielectric permittivity and conductivity during specimen preparation for T1.

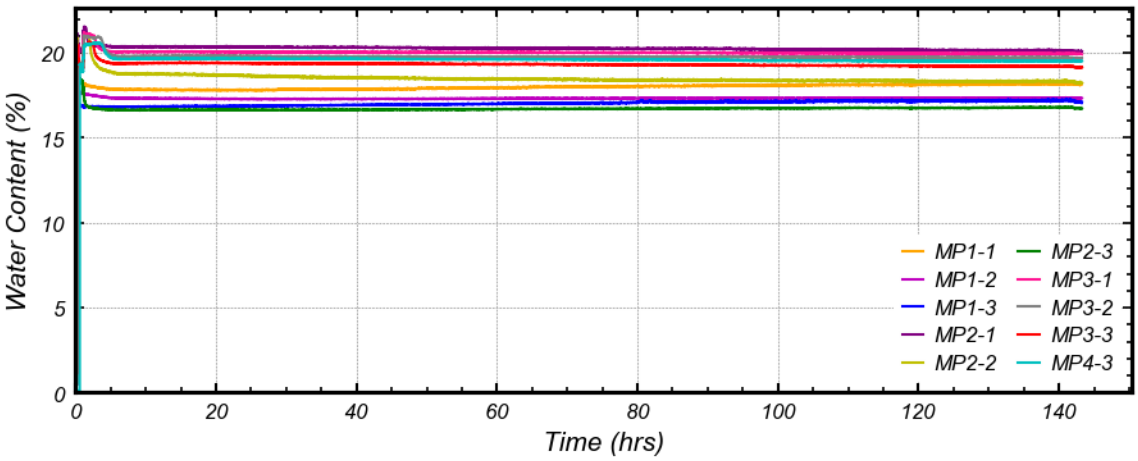

Figure 96. Correlated water content during specimen preparation for T1.

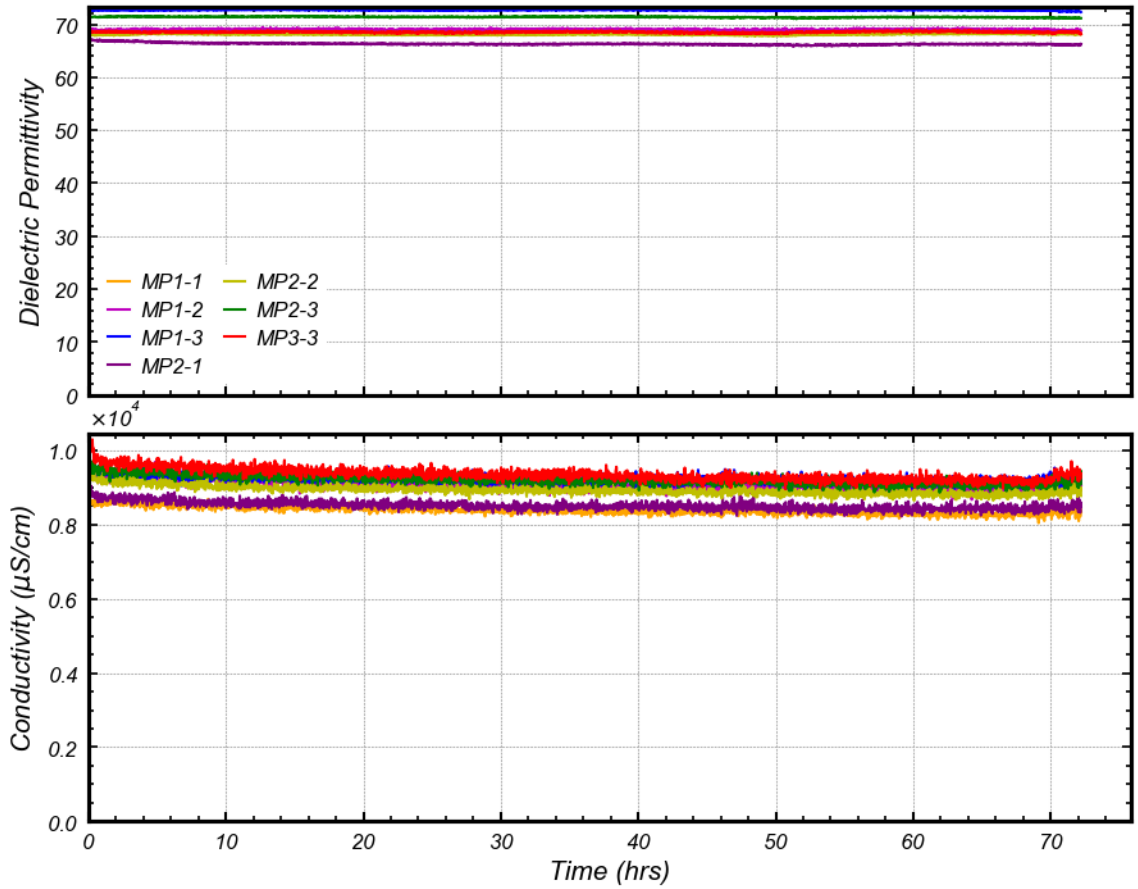

Figure 97. Dielectric permittivity and conductivity during specimen preparation for T2.

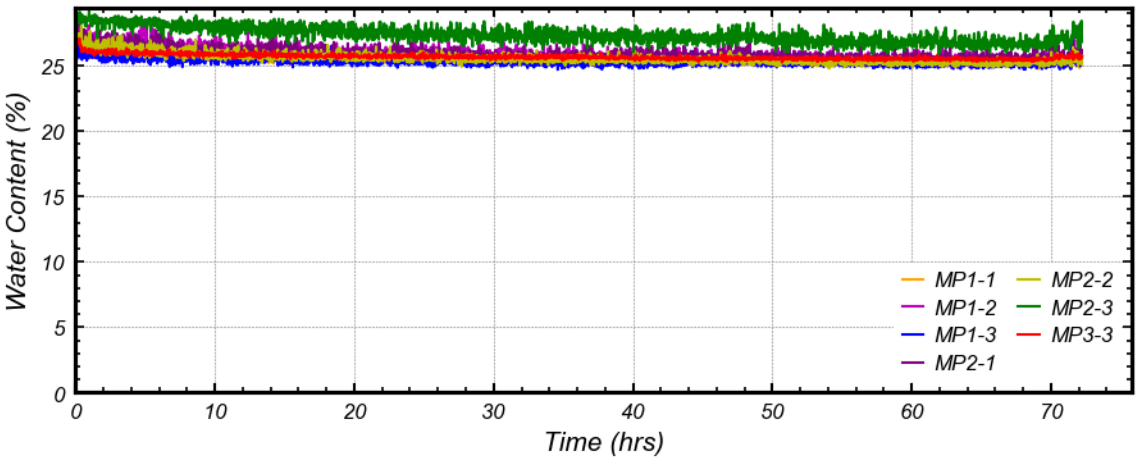

Figure 98. Correlated water content during specimen preparation for T2.

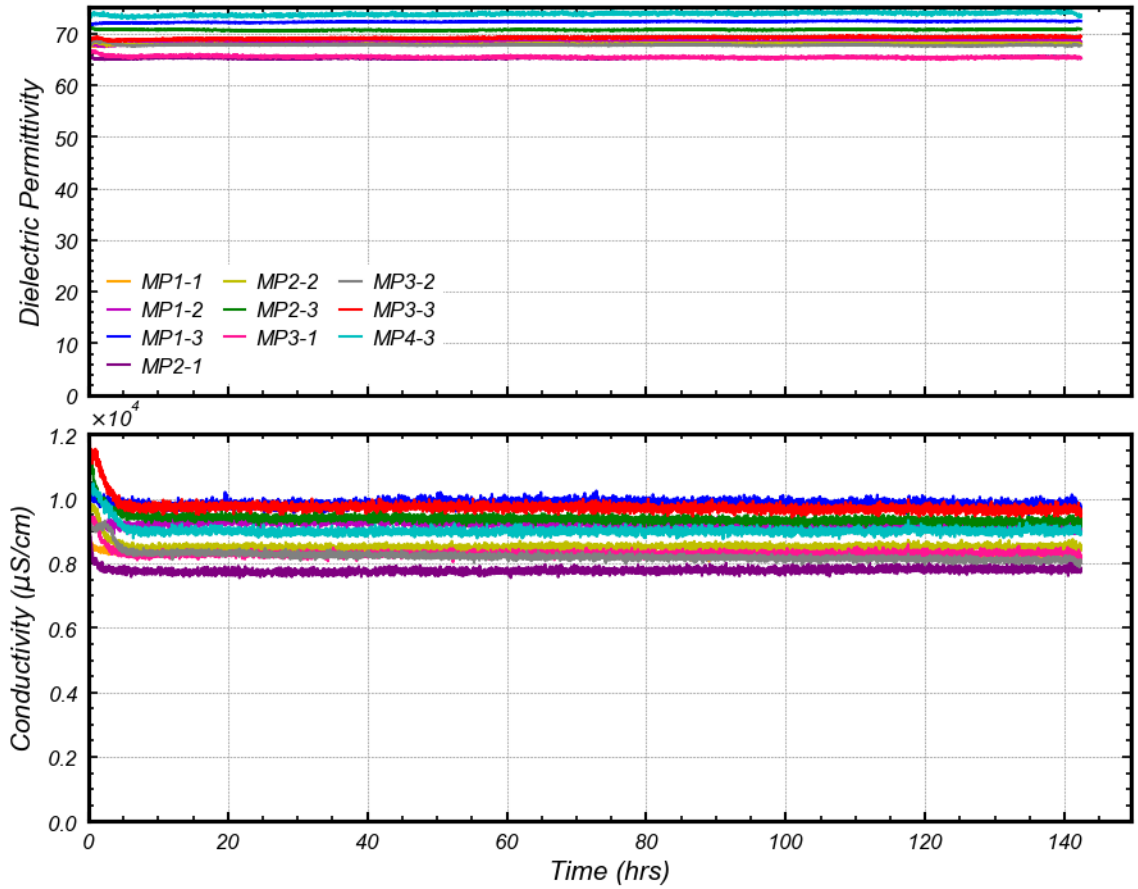

Figure 99. Dielectric permittivity and conductivity during specimen preparation for T3.

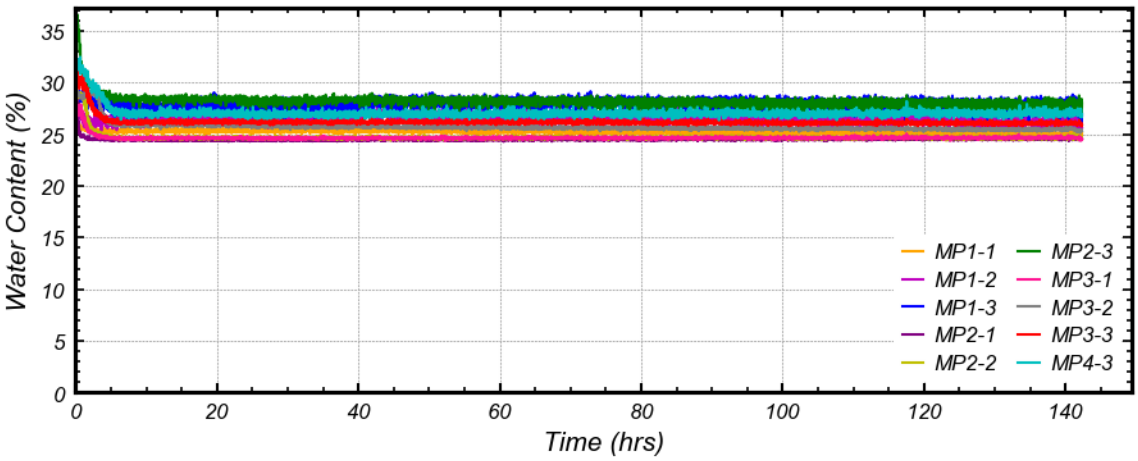

Figure 100. Correlated water content during specimen preparation for T3.

Figure 101 through **Figure 106** present the dielectric permittivity, conductivity, and correlated water content for the three runout tests. The drops in permittivity and conductivity are due to the specific moisture probes becoming exposed after opening of the gates. **Figure 102**, **Figure 104**, and **Figure 106** do not include the predicted water contents of the moisture probes exposed during the runout tests. After opening of the gates, water contents within the ash remained constant. Although difficult to determine without pore pressure data, the lack of changes in water content after opening of the gates suggests minimal flow of water through the failed deposits after failure occurred. This could be due to the small hydraulic gradients present in 1 g conditions of, as well as the relatively short amount of time the runout tests were conducted in (compared to FR06 for example, in which the runout test was performed for a prototype time of about 30 hours).

To build upon the data presented in **Figure 54**, dielectric permittivity for the 1 g tests is plotted against its corresponding conductivity measurements in **Figure 107**. Minus a few outlier points, the data for the 1 g tests between 0 to 5000 µS/cm relatively matches the data obtained in FR06, which behaved linearly below the laboratory data trendline. At about 5000 µS/cm, the 1 g data jumps in dielectric permittivity over a narrow range of conductivity and begins to match the

lab trendline more closely at higher conductivity readings. The 1 g data further suggests that there are unknown factors influencing the dielectric permittivity and conductivity readings in the conductivity range of 0 to 5000 µS/cm, which could also be influencing the predicted water contents based on the developed laboratory calibrations.

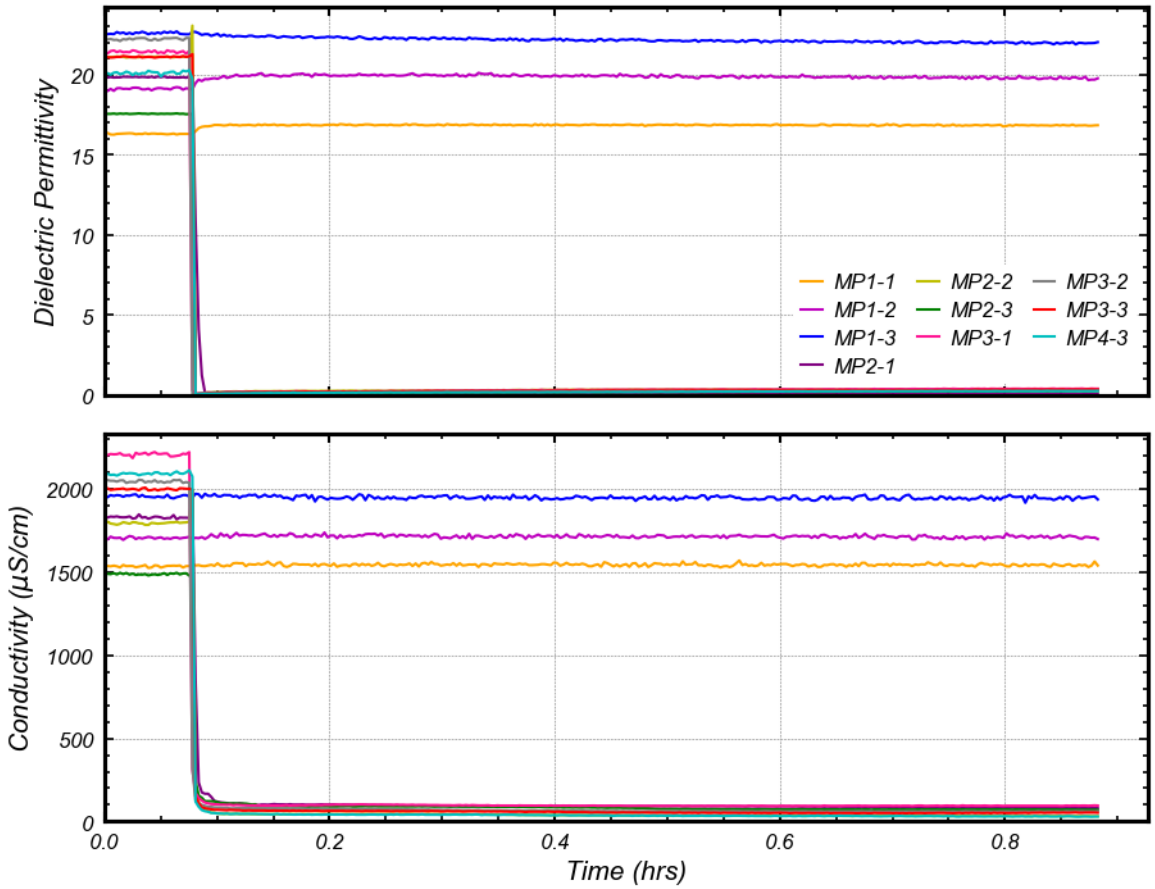

Figure 101. Dielectric permittivity and conductivity during runout test of T1.

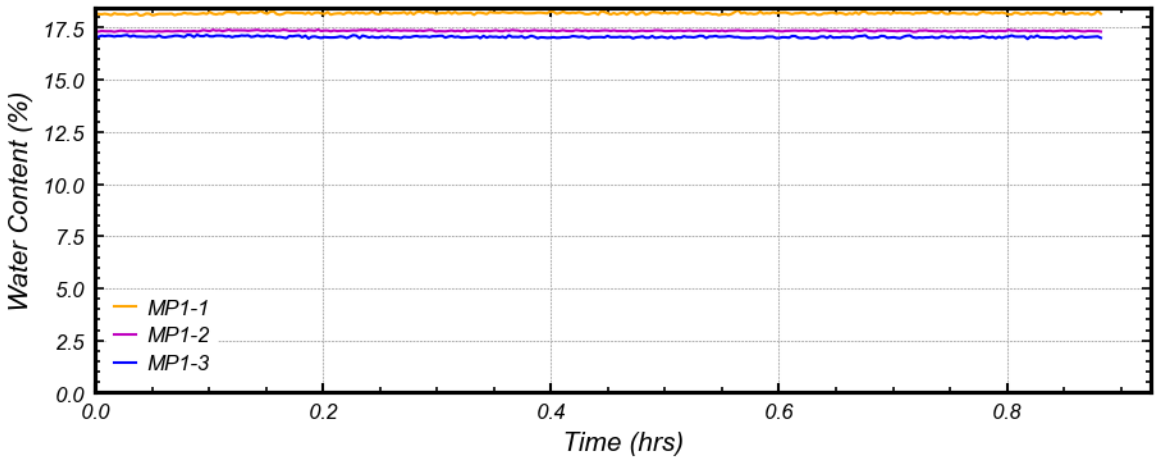

Figure 102. Correlated water content during runout test of T1.

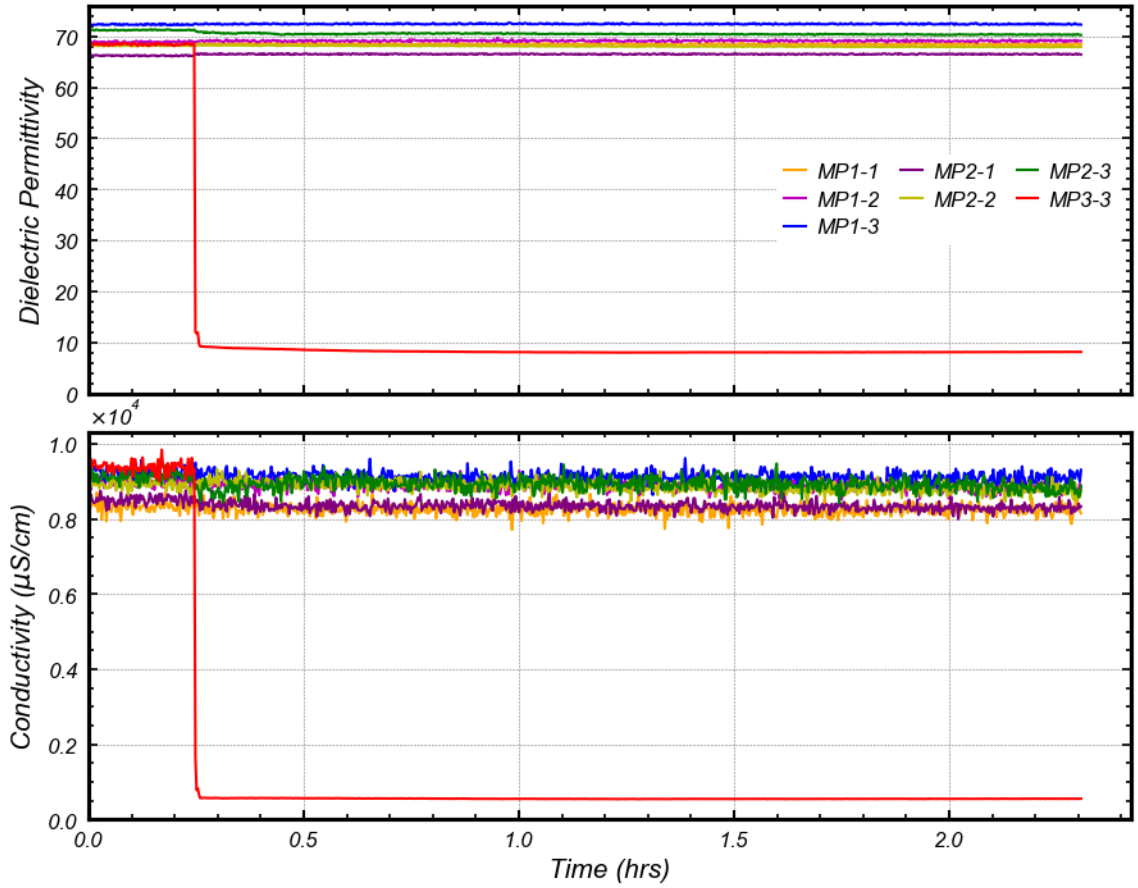

Figure 103. Dielectric permittivity and conductivity during runout test of T2.

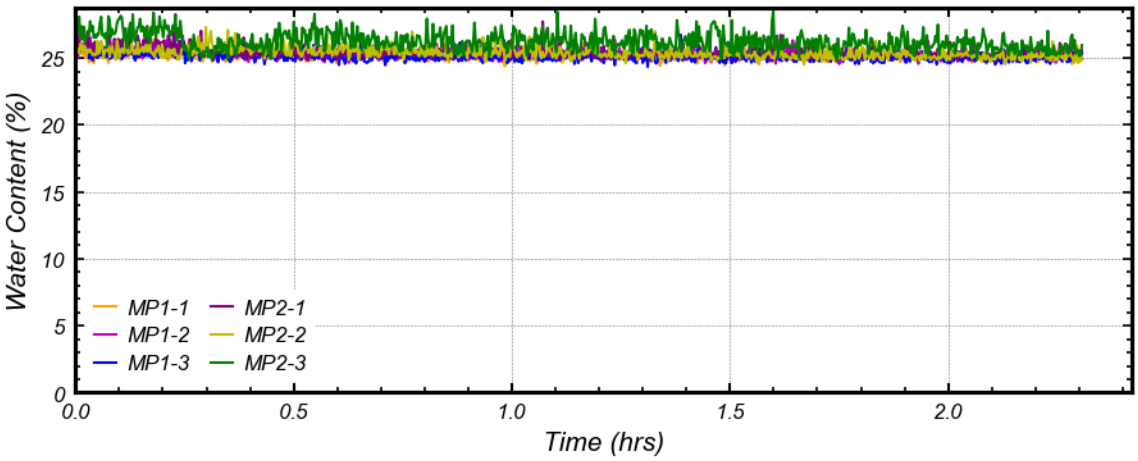

Figure 104. Correlated water content during runout test of T2.

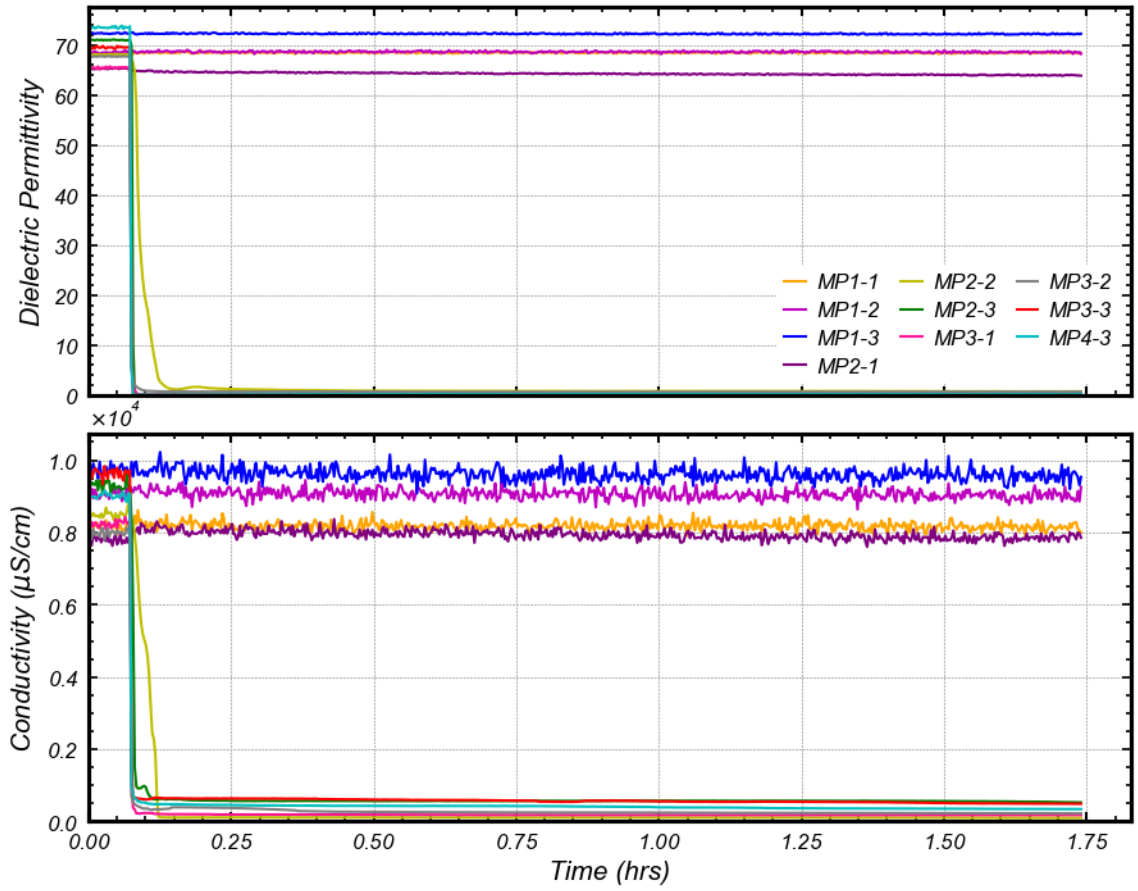

Figure 105. Dielectric permittivity and conductivity during runout test of T3.

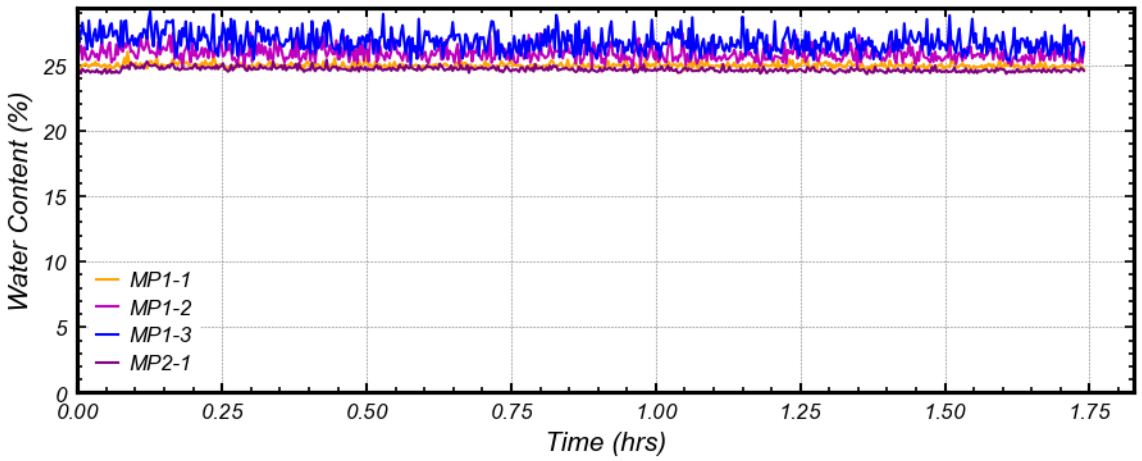

Figure 106. Correlated water content during runout test of T3.

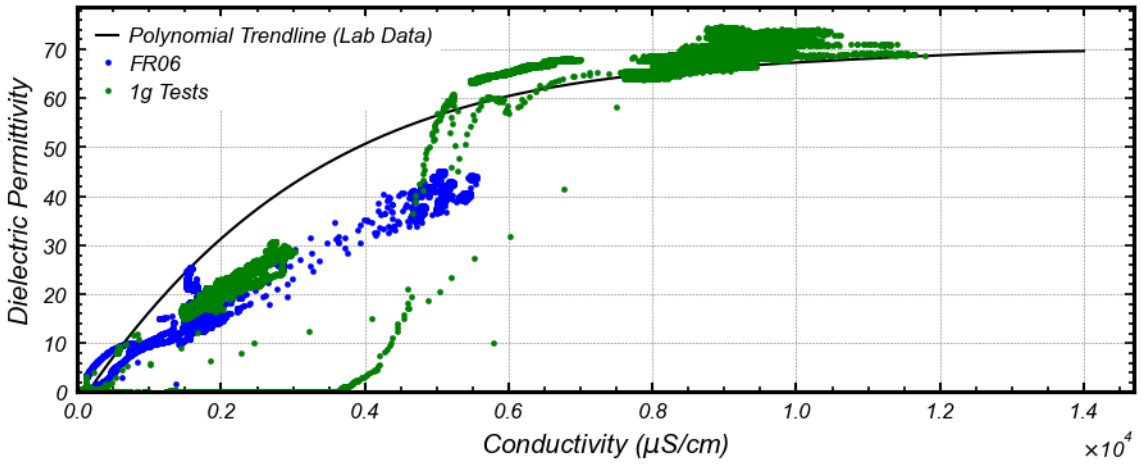

Figure 107. Dielectric permittivity plotted against conductivity for FR06 and 1 g tests.

4.6 Comparison of 1 g Tests to Centrifuge Tests

As has been found in the centrifuge tests, the slurry water content of the ash during deposition plays a significant role in its strength and runout behavior. T2, which had the least runout distance and the highest T-bar resistances, was poured with a slurry water content of 32%, which is similar to what was used for centrifuge tests FR01, FR02, and FR03. FR02 and FR03 both exhibited undrained CPT resistances greater or equal to that of FR05 and FR06 and were poured with slurry water contents between 30 to 40%. The failure modes in the 1 g tests also

changed with changing slurry water contents, similar to the centrifuge tests. Slurry water content appears to have had little effect on measured density of the 1 g tests (see **Figure 85**), but this could be due to errors in measuring the deposit volumes in the 1 g tests. Water content measurements did not increase after opening of the gates in the 1 g tests, whereas some measured water contents did for the centrifuge tests. This is most likely from differences in scaling effects between the centrifuge and 1 g tests (such as time).

Comparing the undrained strength ratios in **Figure 69** and **Figure 92** through **Figure 94**, the average undrained strength ratio from 10 m to 15 m (prototype scale) of FR02, FR03, FR05, and FR06 is 2.80, 4.47, 0.15, and 1.87, respectively. Between 10 cm to 20 cm, the average undrained strength ratio for the fast T-bar pushes for T1, T2, and T3 was 0.22, 1.71, and 0.32, respectively. The tests that exhibited flow failures (FR05, T1, and T3) all had average undrained strength ratios well below 1, while the tests that exhibited slope instability or slumping-like failures (FR02, FR03, FR06, and T2) all had undrained strength ratios exceeding 1.5. From the T-bar resistances, it does not appear a difference in drainage conditions was developed between fast and slow pushes, as it was in the centrifuge tests, which could be due to differences in the coefficient of consolidation of the ash when subjected to 1 g and 60 g conditions. Differences in fast and slow penetration resistances in T1 and T3 may have been due to strain rate effects for undrained shear strength. It should be noted that differences in strain rate during undrained penetration between the CPT and T-bar tests would need to be determined to adequately compare the undrained strength ratios of the centrifuge and 1 g models.

5 CONCLUSIONS

For this thesis, one centrifuge test was performed at the UC Davis CGM to investigate the runout behavior of impounded fly ash. The effects of dewatering on a looser ash were explored, with the strength and stiffness assessed with a miniature CPT probe and bender elements. Moisture probes were used to measure changes in water content during specimen preparation and gate opening, and pore pressure responses were measured with tensiometers. Observed runout behaviors generally agreed with the measured properties of the deposit, which demonstrated shear-induced dilative tendencies for the top 4.6 m (prototype scale), negligible shear-induced dilatancy below to a depth of 11.2 m, and shear -induced contractive tendencies at deeper depths. The results were compared to previous centrifuge tests performed in the project, with similarities drawn to three denser tests and one looser test. Specifically, strength and stiffness and observed dilatancy were found to be similar to the denser tests above 11.5 m, while similarities in strength and dilatancy were found with both the looser and denser tests below this depth. Runout behavior of the test performed was similar to the previous denser tests. Issues were identified in the calibration of the moisture probes, which had been previously observed in the looser test.

Three 1 g tests were also performed to further inform the relationship between initial ash density and runout behavior. Though the density was not able to be accurately determined, a clear relationship between slurry water content, T-bar penetration resistance, and runout behavior was found. Increased slurry water contents led to decreased strengths and larger runout distances, which was found in the centrifuge tests as well. The behavior of the material also clearly depended on confining stress, with failure mechanisms significantly changing between the centrifuge and 1 g tests.

The following sections present specific discussions and conclusions regarding the use of CPTs during geotechnical centrifuge testing of fly ash, 1 g test results, effects of water table height and initial ash density on the 9-m centrifuge tests, and recommendations for future work.

5.1 Cone Penetration Testing in Centrifuge Tests

Through the use of a miniature CPT probe during the centrifuge test FR06, the strength and dilatancy of the deposit were effectively characterized. Measured tip resistances exceeded 3 MPa for both the undrained and drained pushes below a depth of about 2 m prototype scale, and the undrained strength ratio (s_u/σ'_v) exceeds 1 below this depth. Q_{tn} plots above 25 at locations shallower than 13 m and close to below 20 for the remainder of the push. The inferred dilatancy based on the drained to undrained resistance ratio ($q_{c,\ 100\ mm/s}/q_{c,\ 2\ mm/s}$) and clean sand corrected normalized cone tip resistance ($Q_{tn,cs}$) correlate well with the observed shear-induced excess pore pressure response, with both metrics decreasing significantly starting at a prototype depth of 11.5 m. Negative to negligible shear-induced excess pore pressures developed in the 3 shallowest rows of tensiometers (depths of 4.6 m, 7.9 m, and 11.2 m) after opening of the gates, indicating dilative behavior that decreases with depth, and positive excess pore pressures developed at the deepest tensiometer row (depth of 17.8 m) after opening of the gates, indicating contractive behavior. $Q_{tn,cs}$ for FR06 does plot at the lower side of the Robertson (2010) transition zone, but it should be noted that partial saturation above the water table may have led to partially drained conditions during the undrained CPT push. In addition, the assumption of χ being 1 in Equation 10 leads to a slight underprediction of $Q_{tn,cs}$ above the water table, especially near the surface. Overall, a stable response was observed, which aligns with most of the impoundment plotting within the Robertson transition zone.

The CPT results from FR06 also compare well to that of FR02, FR03, and FR05, with differences in behavior aligning with differences in the previously mentioned CPT metrics. The ratio of undrained to drained resistance, Q_{tn}, undrained strength ratio, and $Q_{tn,cs}$ were all significantly higher in the models that exhibited slope instability failures (FR02 and FR03) than in the model that showed a flow failure (FR05), with FR06 being between the two sets of tests.

The shear-induced excess pore pressure responses from the other three tests analyzed support the inferred dilatancy from the CPT results. FR02 and FR03 displayed dilative behavior in the upper portions of the deposits, FR05 was obviously contractive (despite limited availability of pore pressure data), and FR06 displayed dilative and contractive behavior at shallower and greater depths, respectively. $Q_{tn,cs}$ values for FR02 and FR03 plotted within or above the Robertson (2010) transition zone, aligning with the shear-induced pore pressure response. FR05 plotted well below the transition zone, consistent with the observed static liquefaction.

Performing undrained and drained CPT pushes also provided another metric to assess the dilatancy of the ash, the undrained to drained resistance ratio. From a critical state soil mechanics perspective, having a larger undrained than drained shear strength would be expected for dilative (generation of negative shear-induced excess pore pressures), or dense of critical materials, while a higher drained than undrained shear strength would be expected for contractive (generation of positive shear-induced excess pore pressures), or loose of critical materials (see **Figure 108**). Using the normalized penetration velocity framework presented by DeJong and Randolph (2012), penetration velocities for undrained and drained CPT tests determined for the fly ash studied were used. Similar to the calculated Q_{tn} and $Q_{tn,cs}$ values, the undrained to drained resistance ratio correlated well with the observed dilatancy from the shear-induced pore pressure response and runout behavior.

The centrifuge tests performed have demonstrated the value of performing CPTs on impounded fly ash to characterize its strength and dilatancy. Q_{tn} can be calculated based on standard testing in practice, which is typically performed at a penetration velocity of 20 mm/s. This can then be converted to $Q_{tn,cs}$ (a proxy for state parameter) and assessed for flow liquefaction potential, following Robertson (2010). The centrifuge tests have shown that the $Q_{tn,cs}$ transition zone of 50 to 70 can possibly predict the stability of fly ash impoundments in centrifuge testing, with data plotting within or below this criteria displaying negligible to contractive behavior. However, FR06 has $Q_{tn,cs}$ values between 40 to 50 and did not experience a flow failure, but this could be a result of the dewatering performed during the test or the interactions between the ash zones above and below the water table. It is also possible that the transition zone is actually at a lower value for the fly ash studied, as demonstrated by comparing the undrained to drained resistance ratio and $Q_{tn,cs}$ values for FR02. An undrained to drained resistance ratio greater than 1 was calculated for almost the entire depth of FR02, whereas $Q_{tn,cs}$ plots in the transition zone from 4 m prototype scale to the end of the push. Though not typically done in practice, CPT soundings could be performed at fast and slow speeds determined through the DeJong and Randolph (2012) normalized penetration velocity framework to assess undrained and drained strengths of fly ash. Assuming proper CPT equipment is available, this could provide redundancy to the $Q_{tn,cs}$ criteria and also fits into the framework of critical state soil mechanics.

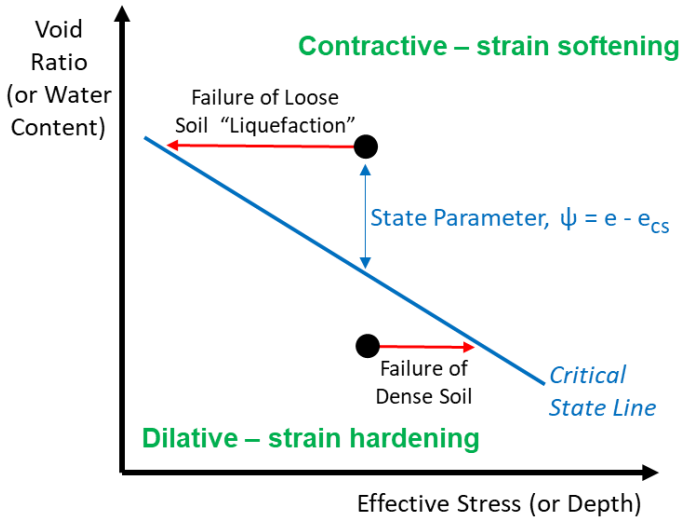

Figure 108. Undrained failure in the perspective of critical state soil mechanics (EPRI 2021).

5.2 1 g Tests

Slurry water content of the ash deposits, and its effect on the settled water content, was found to be a significant factor in the strength of the impoundments during 1 g testing. Densities measured for the three tests were similar, but it is noted that there is error in determining the volume of the impoundments, especially for T2 which had an uneven surface. **Figure 109** plots the corrected T-bar resistance and slurry water content with respect to the measured normalized runout lengths. The runout distance of the ash increased as the slurry water content of the ash increased, with T1 and T3 reaching the extents of the runout basin. This conclusion is also supported by the visual observation that T1 experienced a more liquid-like flow than T3. The slurry water content influenced the T-bar penetration results and the measured undrained shear strength. T1 had the lowest undrained strength ratio (fast pushes) of approximately 0.2, followed by T3 with 0.35. T2 had a significantly larger strength ratio than T1 and T3. The measured undrained strength ratios and corresponding runout lengths were found to roughly correlate with those measured in centrifuge testing, though uncertainty exists in the strength factor ($N_{T\text{-}bar}$) chosen for the 1 g tests

and possible strain-rate effects to determine s_u. The T-bar tests were found to be the only reliable index of strength in the 1 g tests. Work should be performed with slurry water contents between 32% and 40% to refine the transition between the liquid-like flow failure and the slumping failure, which may also provide a refinement of the relationship of slurry water content on T-bar resistance, and the relationship of T-bar resistance to runout length.

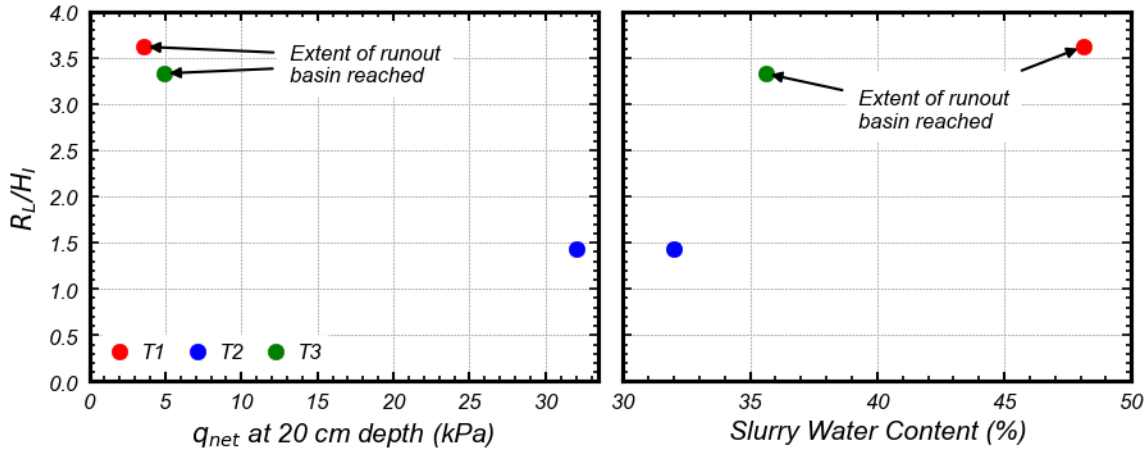

Figure 109. Normalized runout length with respect to q_{net} measured at 20 cm depth and slurry water content.

5.3 Effects of Water Table Height in Centrifuge Tests

Dewatering performed during FR06 significantly increased the vertical effective stress, as shown in **Figure 110**, with the water table drawn down to 59% of the impoundment height. Vertical effective stress doubles in the upper 10 m and the entire impoundment had increases of at least 50%. This increase in effective stress, along with dewatering's effect on ash consolidation and drainage conditions, appears to be the main factor in FR06 having the highest drained CPT tip resistance value, despite having a lower density than the denser tests. During the runout test, only dilative to negligible dilatancy behavior was observed from the shear-induced excess pore

pressures above the water table, as well in the row of tensiometers approximately 3 m below the water table. Shear-induced excess pore pressures at a depth of 17.8 m showed contractive behavior, which only had a 56% increase in effective stress after dewatering. Dewatering also appeared to alter the failure mechanism of FR06, with the initial failure mass consisting of the drier, dewatered zone of ash. The secondary failure occurred by wetter ash breaking through the drier initial failure mass, which likely limited the runout distance in the test (see **Figure 41**). Dewatering of FR06 resulted in less runout with time when compared with FR02 and FR03, as shown by the magnitudes of the green and dark grey arrows in **Figure 111**.

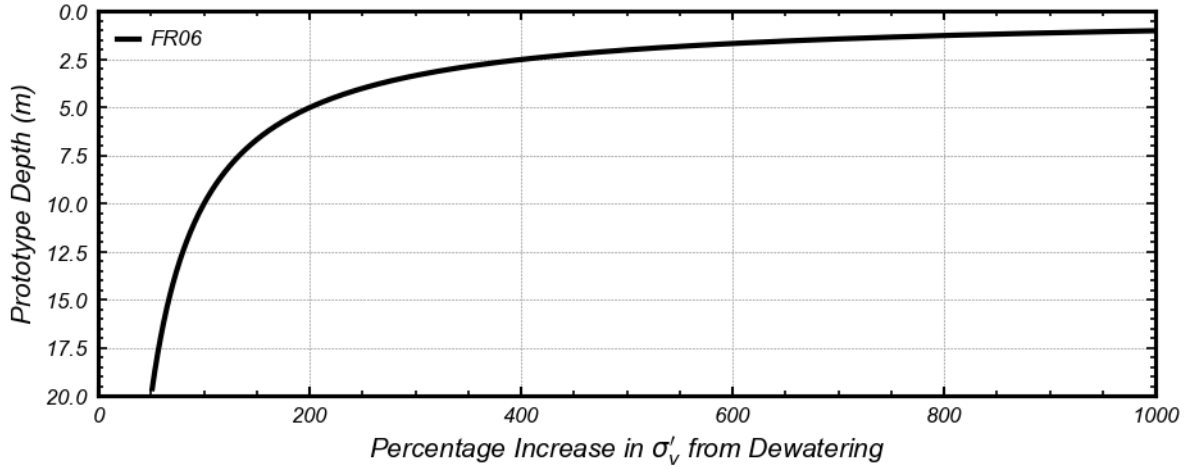

Figure 110. Change in vertical effective stress (σ'_v) from dewatering for FR06 (assuming χ of 1).

Based on the densest centrifuge tests (FR01, FR02, and FR03), the water table height within the ash impoundments has an effect on the runout length. **Figure 111** plots the normalized runout length (R_L/H_I) against the normalized water table height (H_{WT}/H_I), with the densest tests shown in grey. As the water table height of the impoundments increased, the runout length increased. Calculated hydraulic gradients in the impoundments increased with increasing water

table height, increasing the flow of water out of the deposit. The presence of pooled water in FR03 also increased the runout length through surficial erosion of the impoundment. Based on these results, reducing the water table height in already stable ash impoundments will reduce the runout length of the fly ash during centrifuge testing.

Two centrifuge tests were performed on ash with a 'looser' density: FR05 and FR06. Though the calculated density was not entirely similar, the two tests both exhibited pore pressure data well below the water table that showed significant positive shear-induced excess pore pressure spikes after opening of the gates. The water table in FR05 was at the surface of the deposit and was at 59% of the impoundment height in FR06. FR05 experienced a sudden flow failure, while FR06 had a slope instability failure mechanism.

From the results of the five centrifuge tests, dewatering is shown to be effective in reducing the runout length of failed ash impoundments, increasing the effective stress within the impoundment, and can alter the dilatancy of the material under shearing. When plausible in practice, dewatering could be performed at existing fly ash impoundments to improve its stability and reduce the consequences of containment structure failure.

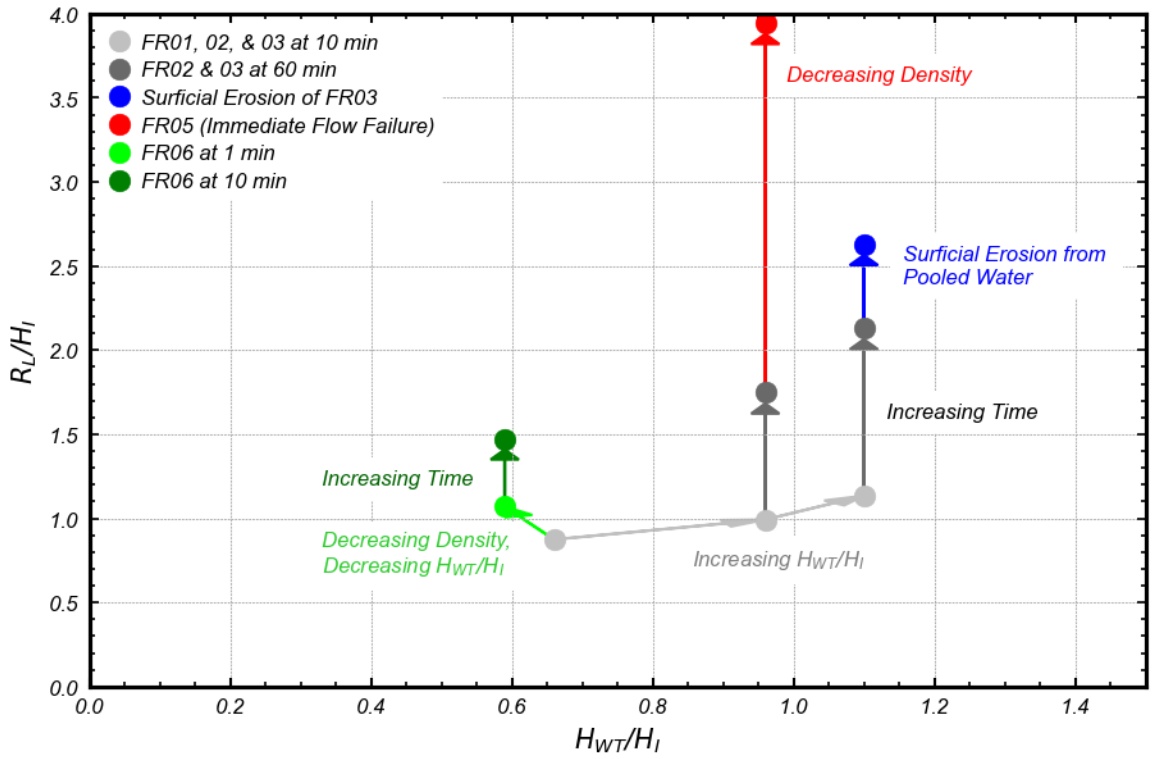

Figure 111. Runout comparison of centrifuge tests, normalized by impoundment height.

5.4 Effects of Ash Density in Centrifuge Tests

Though dewatering was shown to be effective in reducing the runout length of failed ash impoundments, the density of the deposit was shown to have a more dramatic effect on the runout behavior and length. FR01 and FR06 are an example of this; the water table heights had both been lowered during flight to approximately the same level, but FR06 had a larger runout length than FR01. The calculated dry density in FR01 was 16% higher than that of FR06. Density was also the main difference between FR02 and FR05, which had the same normalized water table height. FR02 had a dry density 29% higher than FR05, with FR02 having a slope stability failure and FR05 experiencing a rapid flow failure. Due to the constraints with the length of the runout basin, the true runout distance for FR05 cannot be known. The failure mechanism displayed during this test demonstrates the significant consequences that can result from the failure of looser ash

impoundments. The other four centrifuge tests, all of which had dry densities 16 to 35% higher than FR05, exhibited slope instability failure mechanisms, which has less consequences than the flow failure shown in FR05.

Using the undrained to drained resistance ratios determined from the CPT results, the tests can be designated as generally dense or loose of critical, based on which drainage condition has a greater strength, the shear-induced pore pressure response, and the observed runout behavior. FR01, FR02, and FR03 are generally dense of critical, and FR05 is loose of critical. FR06 had an undrained to drained resistance ratio between 0.75 to 1 to a depth of 11.6 m (prototype scale), which decreased to 0.6 at the bottom of the push at 16 m. Shear-induced volume-change behavior was also determined to be dilative in the upper 4.6 m, negligible in the middle of the deposit, and contractive at the bottom of the deposit. Assuming the deposit was initially uniform, it is possible that dewatering changed the state of the ash in the upper 4.6 m from loose of critical to dense of critical, while the bottom portion of the deposit remained in a loose of critical state. Suppressed excess pore pressure generation from partial drainage effects could have also influenced the results by reducing the magnitude of volume change tendencies, which would affect the measured undrained to drained resistance ratio. It should be noted that the lower portion of FR06 still had a much higher undrained to drained resistance ratio than FR05, likely due to its larger density.

5.5 Recommendations for Future Work

Through the centrifuge and 1 g tests performed at UC Davis, insights have been gained into the behavior of fly ash under a sudden loss of lateral confinement. Dewatering has been shown to be an effective tool to limit the runout of impounded ash, but further work is needed to assess how it affects very loose deposits, such as that in FR05. Additional centrifuge testing is also needed with different normalized water table height ratios.

The effects of density and slurry water content should also be investigated further. The runout behavior in the 1 g tests showed a dependence on the slurry water content, but further work is needed to determine at which slurry water contents the deposited ash will experience changes in runout behavior. A fundamental study on the sedimentation process of fly ash could also be performed, which could refine the laboratory data trendline defined in **Figure 14** for predicting the settled density of fly ash. Further calibration work needs to be performed for the moisture probes, with an emphasis on correlating conductivity to water content more accurately with variations in material boundary conditions (such as plastic versus metallic), scaling effects (such as specimen or container size), and specimen density. Further CPT testing on ash impoundments can provide further insight into the shear-induced dilatancy of fly ash, with additions to the data collected of $Q_{tn,cs}$ and undrained to drained resistance ratios for different failure mechanisms in centrifuge testing. A correlation could also be developed between the undrained to drained resistance ratios to the state parameter, which could help more accurately define a critical state line for the material and account for the effect of the octahedral normal stress pore pressure component described by Burns and Mayne (1998) on the undrained to drained resistance ratios, which would cause a material with an initial state parameter of 0 to still exhibit some positive excess pore pressures during undrained CPT pushes. Finally, further investigation is needed into the effects of density on the runout behavior of fly ash, with further refinement possible for determining the critical state lines of impounded ash.

6 REFERENCES

Bachus, R. C., and Santamarina, J. C. (2014). "Geotechnical Properties and Diagenesis of Ponded Fly Ash." *Geo-Congress 2014 Technical Papers*, American Society of Civil Engineers, Atlanta, Georgia, 326–333.

Bachus, R. C., Terzariol, M., Pasten, C., Chong, S. H., Dai, S., Cha, M. S., Kim, S., Jang, J., Papadopoulos, E., Roshankhah, S., Lei, L., Garcia, A., Park, J., Sivaram, A., Santamarina, F., Ren, X., and Santamarina, J. C. (2019). "Characterization and Engineering Properties of Dry and Ponded Class-F Fly Ash." *Journal of Geotechnical and Geoenvironmental Engineering*, 145(3), 04019003.

Bishop, A. W., and Blight, G. E. (1963). "Some Aspects of Effective Stress in Saturated and Partly Saturated Soils." *Geotechnique*, 13(3), 177–97.

Burns, S. E., and Mayne, P. W. (1998). "Monotonic and dilatory pore-pressure decay during piezocone tests in clay." *Canadian Geotechnical Journal*, 35, 11.

Carey, T., Gavras, A., Kutter, B., Haigh, S. K., Madabhushi, S. P. G., Okamura, M., Kim, D. S., Ueda, K., Hung, W. Y., Zhou, Y. G., Liu, K., Chen, Y. M., Zeghal, M., Abdoun, T., Escoffier, S., and Manzari, M. (2018). "A new shared miniature cone penetrometer for centrifuge testing." *Physical Modelling in Geotechnics*, (A. McNamara, S. Divall, R. Goodey, N. Taylor, S. Stallebrass, and J. Panchal, eds.), 293–298.

Centrifuge Models of Embankment Failures on Saturated Coal Ash. (2015). Electric Power Research Institute, Palo Alto, CA, 145. 3002006290.

D18 Committee. (n.d.). "Test Methods for Determining the Water (Moisture) Content, Ash Content, and Organic Material of Peat and Other Organic Soils." ASTM International.

DeJong, J. T., and Randolph, M. (2012). "Influence of Partial Consolidation during Cone Penetration on Estimated Soil Behavior Type and Pore Pressure Dissipation Measurements." *Journal of Geotechnical and Geoenvironmental Engineering*, 138(7), 777–788.

DeJong, J. T., Yafrate, N. J., and DeGroot, D. J. (2011). "Evaluation of Undrained Shear Strength Using Full-Flow Penetrometers." *Journal of Geotechnical and Geoenvironmental Engineering*, 137(1), 14–26.

Dorodnicov, S. (2018). "The basics of stereo depth vision." https://www.intelrealsense.com/stereo-depth-vision-basics/.

Embankment Loading on Saturated Coal Ash: Centrifuge Demonstration Test. (2013). Electric Power Research Institute, Palo Alto, CA, 178. 3002001146.

Engineering Correlations for Geotechnical Parameters for Ponded Fly Ash: Database Review and Plate Load Test. (2014). Electric Power Research Institute, Palo Alto, CA, 320. 3002001151.

Evaluation of Fly Ash Diagenesis Potential. (2020). Electric Power Research Institute, Palo Alto, CA, 144. 3002016517.

"Frequent Questions about the 2015 Coal Ash Disposal Rule." (2015). United States Environmental Protection Agency. https://www.epa.gov/coalash/frequent-questions-about-2015-coal-ash-disposal-rule#3.

Garnier, J., Gaudin, C., Springman, S. M., Culligan, P. J., Goodings, D., Konig, D., Kutter, B., Phillips, R., Randolph, M. F., and Thorel, L. (2007). "Catalogue of scaling laws and similitude questions in geotechnical centrifuge modelling." *International Journal of Physical Modelling in Geotechnics*, 3, 01–23.

Geotechnical Centrifuge Tests to Assess Stability of Fly Ash Impoundments - Runout and Dewatering Behavior Analysis. Under Review. (2021). Electric Power Research Institute, Palo Alto, CA.

Geotechnical Properties of Fly Ash and Potential for Static Liquefaction: Volume 1 - Summary and Conclusions. (2012). Electric Power Research Institute, Palo Alto, CA, 106. 1023743.

Geotechnical Properties of Fly Ash and Potential for Static Liquefaction: Volume 2 - Data Summary. (2014). Electric Power Research Institute, Palo Alto, CA, 104. 3002001138.

GS3. (2018). METER, Pullman, WA.

Jacobsz, S. W. (2018). "Low cost tensiometers for geotechnical applications." *Physical Modelling in Geotechnics*, (A. McNamara, S. Divall, R. Goodey, N. Taylor, S. Stallebrass, and J. Panchal, eds.), 305–310.

Kalyoncu, R. S. (2001). "Fact Sheet." *U.S. Geological Survey Minerals Yearbook*, Fact Sheet, United States Geological Survey, 1–11.

Kutter, B. L. (1995). "Recent Advances in Centrifuge Modeling of Seismic Shaking." *Third International Conference on Recent Advances in Geotechnical Earthquake Engineering and Soil Dynamics*. St. Louis, MO, 927–941.

Lu, N., and Likos, W. J. (2004). *Unsaturated Soil Mechanics*. Wiley.

Lunne, T., Robertson, P. K., and Powell, J. (1997). *CPT and piezocone testing in geotechnical practice*. Blackie Academic and Professional, London.

MS54XX (RoHS) Miniature SMD Pressure Sensor. (2007). Intersema, 8.

Office of the Inspector General. (2009). *Review of Kingston Fossil Plant Ash Spill Root Cause Study and Observations About Ash Management*. Inspection Report, Tennessee Valley Authority, 110.

Price, A. B., Boulanger, R. W., and DeJong, J. T. (2019). "Centrifuge Modeling of Variable-Rate Cone Penetration in Low-Plasticity Silts." *Journal of Geotechnical and Geoenvironmental Engineering*, 145(11), 04019098.

Randolph, M. F. (2004). "Characterisation of soft sediments for offshore applications." *ISC-2: 2nd Int. Conf. on Site Characterization*, V. da Fonesca and P. Mayne, eds., Millpress, Rotterdam, The Netherlands, 209–232.

Robertson, P. K. (1990). "Soil Classification Using the Cone Penetration Test." *Canadian Geotechnical Journal*, 27(1), 151–58.

Robertson, P. K. (2010). "Evaluation of Flow Liquefaction and Liquefied Strength Using the Cone Penetration Test." *Journal of Geotechnical and Geoenvironmental Engineering*, 136(6), 842–853.

Santamarina, J. C., Torres-Cruz, L. A., and Bachus, R. C. (2019). "Why coal ash and tailings dam disasters occur." *Science*, 364(6440), 526–528.

Stewart, D. P., and Randolph, M. F. (1991). "A new site investigation tool for the centrifuge." *Centrifuge*, 531–538.

APPENDIX

A. Moisture Probe Calibration

As suggested by the manufacturer (METER 2018), a soil specific calibration was performed for the moisture probes to relate measured dielectric permittivity and conductivity to gravimetric water content, using data from EPRI (2021) and this study. Ash samples were created with water contents between 0 to 50% and were deposited in a plastic container (20 cm width, 20 cm length, and 10 cm depth). To make samples with less than 25% water content (the liquid limit of the ash), ash of a known water content was mixed with deionized water in a mixing bowl, to achieve a target water content. Water content tests were performed on the samples after thorough mixing of the ash and water. The ash mixture was then deposited into the plastic container in approximately 2 cm lifts, with tamping performed after each lift to form a compact layer. For samples with a water content above 25%, the ash was mixed directly with water in the plastic container, which formed a thick slurry at about 25% water content. As water was added to the mixture, the thickness of the mixture decreased. About 10 cm thickness of the ash mixture was used for each sample. The metal probes were fully inserted into the sample, with the sensor held in by hand to ensure it was not pulled out erroneously during testing. One to three sensors were tested in the sample at a time, obtaining four to ten readings each.

Based on the data collected and the data from EPRI (2021), calibration functions were created to determine water content from dielectric permittivity or conductivity. A logistics function was fitted to the dielectric permittivity data, and a combination of linear logistic, logistic, and an average between the two was fitted to the conductivity data. The resultant calibration curves are shown in **Figure 26**. A logistics function takes the form of:

$$y = \frac{Max\,Value}{1 + e^{-A(w[\%]-B)}} \quad (30)$$

With a linear logistic function taking the form of:

$$\boldsymbol{y = Max\ Value}\left(\boldsymbol{M} * \boldsymbol{w}[\%] + \boldsymbol{C} + \frac{\boldsymbol{N}}{\boldsymbol{1} + \boldsymbol{e}^{-\boldsymbol{A}(\boldsymbol{w}[\%]-\boldsymbol{B})}}\right) \quad (\mathbf{31})$$

Max Value is the maximum laboratory data point of either dielectric permittivity or conductivity, *A* and *B* are parameters for the logistics curve, *M* and *C* are the slope and intercept for a linear function, respectively, and *N* is a scaling parameter.

For dielectric permittivity, the entire calibration is modeled with only a logistics function. For conductivity, the curve is modeled starting with a logistics function, a separate linear logistics function, and finally the average between the logistics function and the linear logistics function. The transition between the logistic function and linear logistic function is taken as the second intersection of the logistic and linear logistic curves. The transition between the linear logistic function and the average of the logistic and linear logistic function is then taken as the fourth intersection of the logistic and linear logistic curves. **Table 5** and **Table 6** show the fitting parameters determined for each calibration, with the ID No. being the number written on the physical probes in permanent marker (the number that the data logger uses for each sensor). **Figure 112** and **Figure 113** show the individual sensor calibration curves with the measured laboratory data.

Table 5. Fitting parameters for conductivity calibration, based on data from EPRI (2021) and this study.

Moisture Probe (ID No.)	Max Value (µS/cm)	Logistic Only		Linear Logistic					
		A	B	A	B	M	C	L	N
1-1 (7)	11,867	0.301	24.302	1.374	22.969	0.093	-0.781	0.142	0.501
1-2 (4)	12,522	0.280	23.942	1.595	22.862	0.161	-1.114	0.088	0.459
1-3 (0)	13,184	0.254	23.935	1.388	22.700	0.359	-2.355	0.039	0.447
2-1 (8)	11,686	0.306	24.286	1.457	23.011	0.171	-1.355	0.072	0.516
2-2 (5)	12,509	0.286	24.175	1.549	22.908	0.191	-1.426	0.070	0.482
2-3 (1)	12,357	0.273	24.034	1.332	22.783	0.193	-1.428	0.075	0.457
3-1 (9)	12,747	0.261	24.356	1.199	22.790	0.177	-1.442	0.076	0.477
3-2 (6)	11,531	0.283	23.989	0.974	22.988	0.085	-0.577	0.144	0.519
3-3 (2)	13,657	0.294	24.298	0.697	23.236	-0.081	0.650	-0.126	0.596
4-3 (3)	11,965	0.280	23.991	0.750	22.878	0.151	-1.131	0.073	0.561

Table 6. Fitting parameters for dielectric permittivity calibration, based on data from EPRI (2021) and this study.

Moisture Probe (ID No.)	Max Value	A	B
1-1 (7)	66.55	0.444	20.082
1-2 (4)	69.50	0.354	18.970
1-3 (0)	72.40	0.379	19.050
2-1 (8)	66.20	0.396	20.102
2-2 (5)	69.20	0.445	19.236
2-3 (1)	71.10	0.396	19.520
3-1 (9)	67.90	0.481	19.938
3-2 (6)	70.00	0.400	19.249
3-3 (2)	70.10	0.437	20.164
4-3 (3)	74.10	0.487	20.707

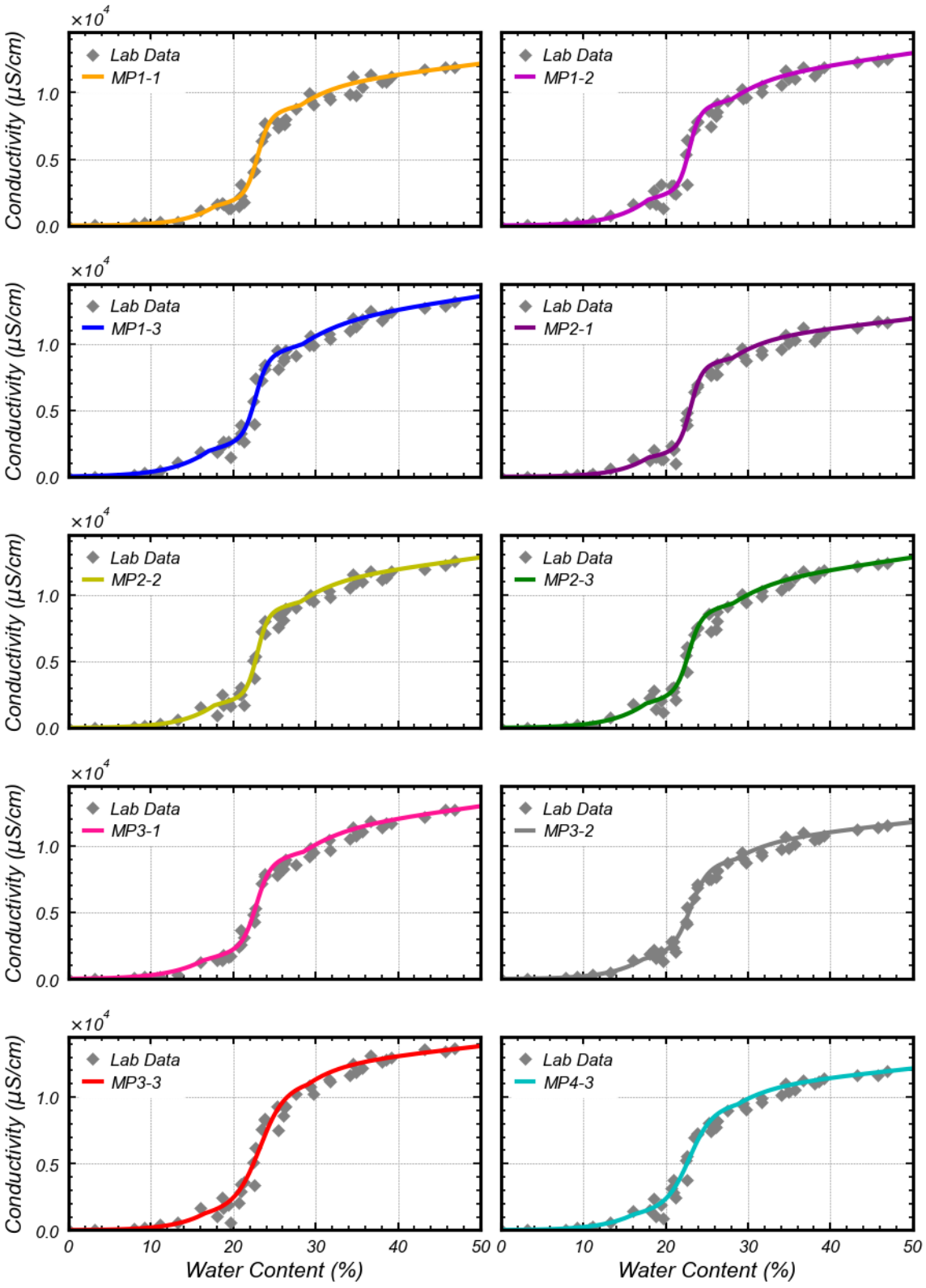

Figure 112. Individual calibration curves for conductivity, based on data from EPRI (2021) and this study.

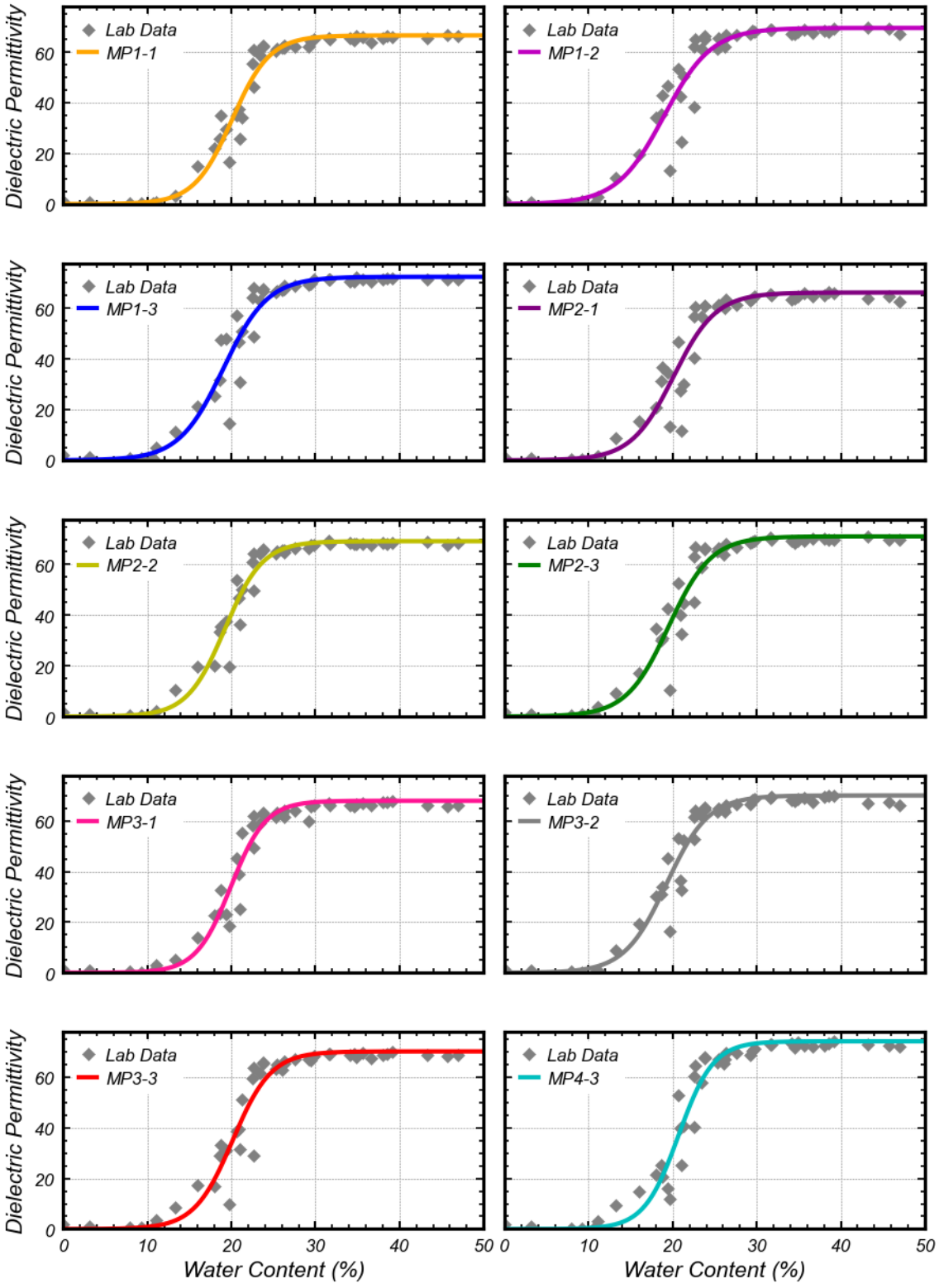

Figure 113. Individual calibration curves for dielectric permittivity, based on data from EPRI (2021) and this study.